National Library of Canada
Bibliothèque nationale du Canada

Canadian Theses Service
Service des thèses canadiennes

Ottawa, Canada
K1A 0N4

NOTICE

The quality of this microform is heavily dependent upon the quality of the original thesis submitted for microfilming. Every effort has been made to ensure the highest quality of reproduction possible.

If pages are missing, contact the university which granted the degree.

Some pages may have indistinct print especially if the original pages were typed with a poor typewriter ribbon or if the university sent us an inferior photocopy.

Reproduction in full or in part of this microform is governed by the Canadian Copyright Act, R.S.C. 1970, c. C-30, and subsequent amendments.

AVIS

La qualité de cette microforme dépend grandement de la qualité de la thèse soumise au microfilmage. Nous avons tout fait pour assurer une qualité supérieure de reproduction.

S'il manque des pages, veuillez communiquer avec l'université qui a conféré le grade.

La qualité d'impression de certaines pages peut laisser à désirer, surtout si les pages originales ont été dactylographiées à l'aide d'un ruban usé ou si l'université nous a fait parvenir une photocopie de qualité inférieure.

La reproduction, même partielle, de cette microforme est soumise à la Loi canadienne sur le droit d'auteur, SRC 1970, c. C-30, et ses amendements subséquents.

NL-339 (r. 88/04) c

Canada

UNIVERSITY OF ALBERTA

DESIGN OF A RECIRCULATING POWER GEAR RIG AND ITS USE IN THE EVALUATION OF TENSILE FILLET STRAIN OF SPUR AND HELICAL GEAR PAIRS

BY

DONALD E. G. PETERSON

(C)

A thesis
submitted to the Faculty of Graduate Studies and Research
in partial fulfilment of the requirements for the degree of

MASTER OF SCIENCE

DEPARTMENT OF MECHANICAL ENGINEERING

Edmonton, Alberta

FALL, 1991

National Library of Canada
Bibliothèque nationale du Canada

Canadian Theses Service
Service des thèses canadiennes

Ottawa, Canada
K1A 0N4

The author has granted an irrevocable non-exclusive licence allowing the National Library of Canada to reproduce, loan, distribute or sell copies of his/her thesis by any means and in any form or format, making this thesis available to interested persons.

L'auteur a accordé une licence irrévocable et non exclusive permettant à la Bibliothèque nationale du Canada de reproduire, prêter, distribuer ou vendre des copies de sa thèse de quelque manière et sous quelque forme que ce soit pour mettre des exemplaires de cette thèse à la disposition des personnes intéressées.

The author retains ownership of the copyright in his/her thesis. Neither the thesis nor substantial extracts from it may be printed or otherwise reproduced without his/her permission.

L'auteur conserve la propriété du droit d'auteur qui protège sa thèse. Ni la thèse ni des extraits substantiels de celle-ci ne doivent être imprimés ou autrement reproduits sans son autorisation.

ISBN 0-315-69922-1

Canada

UNIVERSITY OF ALBERTA

RELEASE FORM

NAME OF AUTHOR: Donald E.G. Peterson

TITLE OF THESIS: Design of a Recirculating Power Gear Rig and its Use in the Evaluation of Tensile Fillet Strain of Spur and Helical Gear Pairs

DEGREE: Master of Science

YEAR THIS DEGREE GRANTED: Fall, 1991

Permission is hereby granted to the University of Alberta Library to reproduce single copies of this thesis and to lend or sell such copies for private, scholarly or scientific research purposes only.

The author reserves all other publication and other rights in association with the copyright in the thesis, and except as hereinbefore provided neither the thesis nor any substantial portion thereof may be printed or otherwise reproduced in any material form whatever without the author's prior written permission.

Donald B. D. Peterson

Donald E.G. Peterson
#220, 14819-51 Avenue
Edmonton, Alberta
T6H 5G4

Date: August 30, 1991

UNIVERSITY OF ALBERTA

FACULTY OF GRADUATE STUDIES AND RESEARCH

The undersigned certify that they have read, and recommend to the Faculty of Graduate Studies and Research for acceptance, a thesis entitled **Design of a Recirculating Power Gear Rig and its Use in the Evaluation of Tensile Fillet Strain of Spur and Helical Gear Pairs** submitted by **Donald E. G. Peterson** in partial fulfillment of the requirements for the degree of **Master of Science**.

J. R. Colbourne

M. G. Faulkner

J. S. Kennedy

D. J. Kennedy

Date: 23 Sept 1991

Abstract

Recirculating power gear testing rigs are used in many areas of gear research. The design and commissioning of a recirculating power gear testing apparatus with a maximum recirculating power of 150 kW and a maximum center distance of 500 mm is described. Using this apparatus an investigation of static tensile fillet strain variation through the meshing cycle was conducted. Strains at 27 measurement sites on eight spur and helical gears were monitored. The experimental results obtained were compared with the American Gear Manufacturers standard AGMA 2001-B88 and the method of Colbourne, which is based on AGMA 2001-B88.

Results indicate that when used for design Colbourne's method will conservatively predict the value of the maximum tensile fillet strain for spur gears. For helical gears, Colbourne's method predicts the maximum tensile fillet strain more conservatively as the difference between the minimum and maximum total contact lengths is decreased. Finally, Colbourne's method predicts the contact point location and load intensity corresponding to the maximum tensile fillet strain more accurately than AGMA 2001-B88.

This thesis is dedicated to my wife, Carol Naslund,
and to my parents, Howard and Arline Peterson.
I love you all so much.

Acknowledgements

The author wishes to express his appreciation to Dr. J.R. Colbourne for his supervision during this research.

The author is also indebted to the machinists and technicians of the Department of Mechanical Engineering, University of Alberta for their excellent contribution to this project.

This research has been funded in part by the Natural Science and Engineering Research Council.

The author would especially like to thank his parents for their years of moral support, and his wife, Carol, for her caring and timely suggestions.

Contents

Abstract iv

Acknowledgements vi

Chapter 1

Introduction 1

1.1 Spur and Helical Gear Tooth Stresses 1

1.2 Scope of Work 2

Chapter 2

Bending Stresses in Spur and Helical Gear Teeth 3

2.1 Introduction 3

2.2 Load Magnitude and Position 3

2.3 Load Intensity 7

2.4 Equivalent Spur Gear 16

2.5 Helical and Spur Gear Tensile Fillet Stresses 17

2.6 Load Position, Intensity, and Maximum Fillet Stresses for Different Classes of Gears 20

2.6.1 Spur Gears 20

2.6.2 Helical Gears with $m_F \leq (2 - m_p)$ 22

2.6.3 Helical Gears with $(2 - m_p) < m_F \leq 1$ 24

2.6.4 Helical Gears with $m_F > 1$ 26

2.7 AGMA 2001-B88 28

Chapter 3

Gear Testing Apparatus Design 31

3.1 Overview 31

3.1.1 Types of Gear Testing Apparatus 31
3.1.2 Examples of Gear Testing and Research Conducted with Recirculating Power Gear Testing Apparatus 34
3.1.3 Design Requirements 35
3.2 System Losses: Determination of Maximum Recirculating Power 37
3.2.1 Introduction 37
3.2.2 Gear Power Losses 37
3.2.3 Bearing Power Losses 42
3.3 Test Gear Size Determination from a Failure Study 42
3.3.1 Gear Failure Modes 42
3.3.2 Gear Failure Study 46
3.4 Shaft and Bearing Design 49
3.4.1 Shaft Design 49
3.4.2 Bearing Selection 54
3.4.3 Bearing Lubrication 58
3.5 Gear Lubrication System Design and Gear Lubricant Specifications 58
3.5.1 Lubrication System Design 58
3.5.2 Lubricant Specification 60
3.6 Final Design 62

Chapter 4

Instrumentation **65**

4.1 Transducers 65
4.2 Microcomputer Based Data Acquisition System 69

Chapter 5

Experimental Investigation **73**

5.1 Introduction 73

5.2 Test Gear Design 73
5.2.1 Gear Tooth Profile 73
5.2.2 Gear Body Design and Manufacture 74
5.3 Test Procedure 75
5.3.1 Strain Gage Locations 75
5.3.2 Test Procedure 75
5.4 Test Results 81
5.4.1 Theoretical Variation of Strain Through the Meshing Cycle of Spur Gears S1-S4 81
5.4.2 Measured Strain Variation for 5 Module Spur Gears S1 and S2 83
5.4.3 Measured Strain Variation for 8 Module Spur Gears S3 and S4 87
5.4.4 Theoretical Variation of Strain Through the Meshing Cycle of Helical Gears H1-H4 92
5.4.5 Measured Strain Variations for the 6 Module Helical Gears H1 and H2 102
5.4.6 Measured Strain Variations for the 8 Module Helical Gears H3 and H4 114
5.4.7 Examination of the Differences Between Experimental and Theoretical Tensile Fillet Strains 121

Chapter 6
Conclusions **128**

References **130**

List of Tables

2.1 Load Position and Intensity Values Corresponding to Maximum Tensile Fillet Stresses for Various Classes of Gears 30

3.1 Gear Specifications for Meshing and Windage Loss Calculations 40

3.2 Bearing Specifications for Power Loss Calculations 43

3.3 Sample Data for Gear Failure Study 47

3.4 Comparison of 10 Element Finite Element Model to the Exact Solution for a Cantilevered Shaft 52

3.5 Specifications of the Recirculating Power Gear Testing Apparatus 63

5.1 Test Gear Description 76

5.2 Strain Gage Locations 77

List of Figures

2.1 Arbitrary Transverse Section of Two Helical Gears 4

2.2 Description of Contact Point Location Along the Path of Contact 6

2.3 Progression of Gear Teeth Through the Meshing Cycle 8

2.4 Transverse Section Showing Two Pairs of Teeth in Contact 10

2.5 Meshing Diagram for Two Helical Gears 12

2.6 Contact Region Corresponding to Figure 2.5 and Geometry Used to Determine the Length of the Lines of Contact 13

2.7 Geometry of and Loading on a Driven Equivalent Spur Gear Tooth 18

2.8 Contact Region when $m_F = 0$ 21

2.9 Contact Region when $m_F \leq (2 - m_p)$ 23

2.10 Contact Region when $(2 - m_p) < m_F < 1$ 25

2.11 Contact Region when $m_F > 1$ 27

3.1 Open Loop Gear Testing Apparatus Schematic 32

3.2 Recirculating Power Loop Gear Testing Apparatus Schematic 32

3.3 Drive Motor Efficiency as a Function of Rated Load 36

3.4 Drive Motor Efficiency as a Function of Rated Speed 36

3.5 Coefficient of Friction from Dudley [19] 38

3.6 Sliding Friction Power Losses Corresponding to the Gear Pairs Described in Table 3.1 38

3.7 Windage Power Losses (kW) Corresponding to the Gear Pairs Described in Table 3.1 41

3.8 Windage Power Losses as a Function of Drive Motor Power 41

3.9 Bearing Power Losses for the Ball Bearing Geometries Described in Table 3.2 44

3.10 Bearing Power Losses for the Angular Contact Ball Bearings Described in Table 3.2 44

3.11 Bearing Power Losses Corresponding to the Spherical Roller Bearing Geometries Described in Table 3.2 45

3.12 Maximum Allowable Torques without Incurring Gear Failure: Gear Group 1, 500 r.p.m. 48

3.13 Maximum Allowable Torques without Incurring Gear Failure: Gear Group 1, 1500 r.p.m. 48

3.14 Maximum Allowable Torques without Incurring Gear Failure: Gear Group 2, 500 r.p.m. 50

3.15 Maximum Allowable Torques without Incurring Gear Failure: Gear Group 2, 1500 r.p.m. 50

3.16 Maximum Allowable Torques without Incurring Gear Failure: Gear Group 3, 500 r.p.m. 51

3.17 Maximum Allowable Torques without Incurring Gear Failure: Gear Group 3, 1500 r.p.m. 51

3.18 Finite Element Code Test Model 52

3.19 Driving and Driven Shaft Finite Element Models 53

3.20 Deflections of the Driving Shaft Finite Element Model 55

3.21 Slopes of Driving Shaft Finite Element Model 55

3.22 Deflections of Driven Shaft Finite Element Model: Bearings 7 and 8 Omitted 56

3.23 Deflections of Driven Shaft Finite Element Model: Bearings 7 and 8 Included 56

3.24 Slopes of the Driven Shaft Finite Element Model: Bearings 7 and 8 Omitted 57

3.25 Slopes of the Driven Shaft Finite Element Model: Bearings 7 and 8 Included 57

4.1 Schematic of Transducer Locations 66

4.2 Block Diagram and Specifications for the MetraByte Dash 8 Data Acquisition Board 70

4.3 Schematic of Signal and Data Line Connections Between the Gear Testing Apparatus and the Microcomputer Based Data Acquisition System 71

5.1 Static Positioner Schematic 78

5.2 Static Positioner Calibration Curve 80

5.3 Theoretical Normalized Tensile Fillet Strain, Load Intensity, and Load Radius Variation, 5 Module Spur Gears 82

5.4 Theoretical Normalized Tensile Fillet Strain, Load Intensity and Load Radius Variation, 8 Module Spur Gears 82

5.5 Measured Variation of Strain Along the Line of Contact and Contact Pattern for Gage 10, Torque = 413 Nm 84

5.6 Measured Variation of Strain Along the Line of Contact and Contact Patterns for Gages 11 and 12, Torque = 413 Nm 84

5.7 Measured Variation of Strain Along the Line of Contact and Contact Pattern for Gage 10, Torque = 827 Nm 85

5.8 Measured Variation of Strain Along the Line of Contact and Contact Patterns for Gages 11 and 12, Torque = 827 Nm 85

5.9 Measured Variation of Strain Along the Line of Contact and Contact Pattern for Gage 10, Torque = 1241 Nm 86

5.10 Measured Variation of Strain Along the Line of Contact and Contact Patterns for Gages 11 and 12, Torque = 1241 Nm 86

5.11 Measured Variation of Strain Along the Line of Contact on 5 Module Spur Gears: Composite Data, Torque = 413 Nm 88

5.12 Measured Variation of Strain Along the Line of Contact on 5 Module Spur Gears: Composite Data, Torque = 827 Nm 88

5.13 Measured Variation of Strain Along the Line of Contact on 5 Module Spur Gears: Composite Data, Torque = 1241 Nm 89

5.14 Measured Variation of Strain Along the Line of Contact and Contact Patterns for Gages 1 and 2, Torque = 413 Nm 90

5.15 Measured Variation of Strain Along the Line of Contact and Contact Patterns for Gages 3 and 4, Torque = 413 Nm 90

5.16 Measured Variation of Strain Along the Line of Contact and Contact Patterns for Gages 5 and 7, Torque = 413 Nm 91

5.17 Measured Variation of Strain Along the Line of Contact and Contact Patterns for Gages 8 and 9, Torque = 413 Nm 91

5.18 Measured Variation of Strain Along the Line of Contact and Contact Patterns for Gages 1 and 2, Torque = 827 Nm 93

5.19 Measured Variation of Strain Along the Line of Contact and Contact Patterns for Gages 3 and 4, Torque = 827 Nm 93

5.20 Measured Variation of Strain Along the Line of Contact and Contact Patterns for Gages 5 and 7, Torque = 827 Nm 94

5.21 Measured Variation of Strain Along the Line of Contact and Contact Patterns for Gages 8 and 9, Torque = 827 Nm 94

5.22 Measured Variation of Strain Along the Line of Contact and Contact Patterns for Gages 1 and 2, Torque = 1241 Nm 95

5.23 Measured Variation of Strain Along the Line of Contact and Contact Patterns for Gages 3 and 4, Torque = 1241 Nm 95

5.24 Measured Variation of Strain Along the Line of Contact and Contact Patterns for Gages 5 and 7, Torque = 1241 Nm 96

5.25 Measured Variation of Strain Along the Line of Contact and Contact Patterns for Gages 8 and 9, Torque = 1241 Nm 96

5.26 Measured Variation of Strain Along the Line of Contact on 8 Module Spur Gears: Composite Data, Torque = 413 Nm 97

5.27 Measured Variation of Strain Along the Line of Contact on 8 Module Spur Gears: Composite Data, Torque = 827 Nm 97

5.28 Measured Variation of Strain Along the Line of Contact on 8 Module Spur Gears: Composite Data, Torque = 1241 Nm 98

5.29 Theoretical Normalized Tensile Fillet Strain, Load Intensity, and Load Radius Variation, 6 Module Helical Gears, z/F = 1.0 99

5.30 Theoretical Normalized Tensile Fillet Strain, Load Intensity, and Load Radius Variation, 6 Module Helical Gears, z/F = 0.5 99

5.31 Theoretical Normalized Tensile Fillet Strain Load Intensity, and Load Radius Variation, 6 Module Helical Gears, z/F = 0.0 101

5.32 Theoretical Normalized Tensile Fillet Strain, Load Intensity and Load Radius Variation, 8 Module Helical Gears, z/F = 1.0 101

5.33 Theoretical Normalized Tensile Fillet Strain, Load Intensity, and Load Radius Variation, 8 Module Helical Gears, z/F = 0.5 103

5.34 Theoretical Normalized Tensile Fillet Strain, Load Intensity, and Load Radius Variation, 8 Module Helical Gears, z/F = 0.0 103

5.35 Measured Variation of Strain Along the Line of Contact and Contact Pattern for Gage 22, Torque = 413 Nm, z/F = 0.5 104

5.36 Measured Variation of Strain Along the Line of Contact and Contact Pattern for Gage 23, Torque = 413 Nm, z/F = 0.2 104

5.37 Measured Variation of Strain Along the Line of Contact and Contact Pattern for Gage 24, Torque = 413 Nm, z/F = 0.35 105

5.38 Measured Variation of Strain Along the Line of Contact and Contact Pattern for Gage 25, Torque = 413 Nm, z/F = 0.5 105

5.39 Measured Variation of Strain Along the Line of Contact and Contact Patterns for Gages 26 and 27, Torque = 413 Nm, z/F = 0.5 106

5.40 Measured Variation of Strain Along the Line of Contact and Contact Patterns for Gages 28 and 29, Torque = 413 Nm, z/F = 0.5 106

5.41 Measured Variation of Strain Along the Line of Contact and Contact Pattern for Gage 22, Torque = 827 Nm, z/F = 0.5 108

5.42 Measured Variation of Strain Along the Line of Contact and Contact Pattern for Gage 23, Torque = 827 Nm, z/F = 0.2 108

5.43 Measured Variation of Strain Along the Line of Contact and Contact Pattern for Gage 24, Torque = 827 Nm, z/F = 0.35 109

5.44 Measured Variation of Strain Along the Line of Contact and Contact Pattern for Gage 25, Torque = 827 Nm, z/F = 0.5 109

5.45 Measured Variation of Strain Along the Line of Contact and Contact Patterns for Gages 26 and 27, Torque = 827 Nm, z/F = 0.5 110

5.46 Measured Variation of Strain Along the Line of Contact and Contact Patterns for Gages 28 and 29, Torque = 827 Nm, z/F = 0.5 110

5.47 Measured Variation of Strain Along the Line of Contact and Contact Pattern for Gage 22, Torque = 1241 Nm, z/F = 0.5 111

5.48 Measured Variation of Strain Along the Line of Contact and Contact Pattern for Gage 23, Torque = 1241 Nm, z/F = 0.2 111

5.49 Measured Variation of Strain Along the Line of Contact and Contact Pattern for Gage 24, Torque = 1241 Nm, z/F = 0.35 112

5.50 Measured Variation of Strain Along the Line of Contact and Contact Pattern for Gage 25, Torque = 1241 Nm, z/F = 0.5 112

5.51 Measured Variation of Strain Along the Line of Contact and Contact Patterns for Gages 26 and 27, Torque = 1241 Nm, z/F = 0.5 113

5.52 Measured Variation of Strain Along the Line of Contact and Contact Pattern for Gages 28 and 29, Torque = 1241 Nm, z/F = 0.5 113

5.53 Measured Variation of Strain Along the Line of Contact on 6 Mod. Helical Gears: Composite Data, Torque = 413 Nm, z/F = 0.5 115

5.54 Measured Variation of Strain Along the Line of Contact on 6 Mod. Helical Gears: Composite Data, Torque = 827 Nm, z/F = 0.5 115

5.55 Measured Variation of Strain Along the Line of Contact on 6 Mod. Helical Gears: Composite Data, Torque = 1241 Nm, z/F = 0.5 116

5.56 Measured Variation of Strain Along the Line of Contact and Contact Patterns for Gages 13 and 14, Torque = 413 Nm, z/F = 0.5 117

5.57 Measured Variation of Strain Along the Line of Contact and Contact Patterns for Gages 16 and 17, Torque = 413 Nm, z/F = 0.5 117

5.58 Measured Variation of Strain Along the Line of Contact and Contact Patterns for Gages 18 and 19, Torque = 413 Nm, z/F = 0.5 118

5.59 Measured Variation of Strain Along the Line of Contact and Contact Patterns for Gages 20 and 21, Torque = 413 Nm, z/F = 0.5 118

5.60 Measured Variation of Strain Along the Line of Contact and Contact Patterns for Gages 13 and 14, Torque = 827 Nm, z/F = 0.5 119

5.61 Measured Variation of Strain Along the Line of Contact and Contact Patterns for Gages 16 and 17, Torque = 827 Nm, z/F = 0.5 119

5.62 Measured Variation of Strain Along the Line of Contact and Contact Patterns for Gages 18 and 19, Torque = 827 Nm, z/F = 0.5 120

5.63 Measured Variation of Strain Along the Line of Contact and Contact Patterns for Gages 20 and 21, Torque = 827 Nm, z/F = 0.5 120

5.64 Measured Variation of Strain Along the Line of Contact and Contact Patterns for Gages 13 and 14, Torque = 1241 Nm, z/F = 0.5 122

5.65 Measured Variation of Strain Along the Line of Contact and Contact Patterns for Gages 16 and 17, Torque = 1241 Nm, z/F = 0.5 122

5.66 Measured Variation of Strain Along the Line of Contact and Contact Patterns for Gages 18 and 19, Torque = 1241 Nm, z/F = 0.5 123

5.67 Measured Variation of Strain Along the Line of Contact and Contact Patterns for Gages 20 and 21, Torque = 1241 Nm, z/F = 0.5 123

5.68 Measured Variation of Strain Along the Line of Contact on 8 Mod. Helical Gears: Composite Data, Torque = 413 Nm, z/F = 0.5 124

5.69 Measured Variation of Strain Along the Line of Contact on 8 Mod. Helical Gears: Composite Data, Torque = 827 Nm, z/F = 0.5 124

5.70 Measured Variation of Strain Along the Line of Contact on 8 Mod. Helical Gears: Composite Data, Torque = 1241 Nm, z/F = 0.5 125

List of Plates

3.1 Recirculating Power Gear Testing Apparatus 64

4.1 Transducer Location on the Gear Testing Apparatus 67

4.2 Gear Testing Apparatus Measurement Equipment 72

Chapter 1: Introduction

1.1 Spur and Helical Gear Tooth Stresses

Potential failure of gear teeth from static overload or bending fatigue failure is an area of concern to both gear designers and users because initiation of these failures is often difficult to detect and progression to final failure can be rapid. Catastrophic failure of the gear or gear box usually results with the distinct possibility of damage to drive systems or loads. Depending on the size and location of the gear box, large costs can be incurred during its replacement or repair. Finally, large financial losses can occur as a result of unscheduled equipment downtime and possible production loss associated with such failures.

As increasing demands have been placed on the precision and load carrying capacity of gears, it has become more important to understand the mechanism by which power is transmitted through gears. For the case of spur gears, whose teeth are parallel to the gear axis, the region of contact between two gear teeth is a line segment which is parallel to the gear axis. As the gears rotate through the meshing cycle the position of this contact line on a driven gear tooth will vary between the tooth tip and a point much lower on the tooth's surface. Additionally, it is observed that at some points in the meshing cycle one pair of gear teeth are in contact while at other times two pairs of teeth are in contact. Consequently, the load on a gear tooth, which is usually expressed in terms of the tensile stress or strain in the gear tooth fillet, must be a function of the position of the contact point between the gears and the number of gear pairs in contact. The former quantity will be referred to as the load radius in this thesis. The latter quantity will be expressed in terms of the load intensity, which is equal to the total load transferred between the gear teeth divided by the total length of the contact lines of all the pairs of teeth in contact.

In helical gears, the gear teeth are not parallel to the gear axis but instead form helices about the gear axis. The angle between the helix tangent and the gear axis is known as the helix angle. The cross section of a helical gear cut at right angles to the gear's axis is known as a transverse section. The transverse section of a helical gear will be the same as a transverse section of a spur gear. The contact region between two helical gears teeth is a line segment which is inclined with respect to the gear axis. As

a helical gear tooth is driven through the mesh, the contact line will move down the face of the tooth and will change in length. While this is happening, contact lines may be appearing, disappearing, or maintaining constant length on the surfaces of other teeth in the mesh. The total length of these lines of contact in the meshing region may remain constant or vary widely for a pair of helical gears. As a result, the tensile fillet stresses developed in helical gear teeth at a particular transverse plane will be a function of load intensity and load radius. From the foregoing discussion it should be apparent that the determination of fillet stresses for helical gears is much more complex than for spur gears.

1.2 Scope of Work

This thesis reports the results of an experimental investigation of the variation of tensile fillet strains through the meshing cycle of spur and helical gear pairs. In Chapter 2, expressions are developed which can be used to determine analytically the tensile stresses and strains in the fillets of spur and helical gear teeth as the gears pass through the meshing region. These expressions are based on the American Gear Manufacturer's Association (AGMA) standard, AGMA 2001-B88 [1] as adapted by Colbourne [2]. Chapter 3 describes the mechanical design of a recirculating power gear testing apparatus constructed as part of this work. This device was designed to perform gear research in a number of areas. Chapter 4 discusses details of the instrumentation installed on the gear testing apparatus, and the 80286 based microcomputer system used to collect data from it. Chapter 5 describes the experimental investigation which was conducted. The design of the test gears is described as well as the test procedure followed. The experimentally determined values of maximum fillet strains obtained from this investigation are compared to Colbourne's method. The value of the load radius and load intensity at the location of maximum fillet strain is compared to the corresponding values predicted by Colbourne's method and AGMA 2001-B88. Differences between the theoretical and measured results are then discussed by comparing the results obtained in this study with the results of other investigators. Finally, in Chapter 6 conclusions based on this experimental study are presented.

Chapter 2: Bending Stresses in Spur and Helical Gear Teeth

2.1 Introduction

Expressions are developed to determine analytically the tensile stresses in the fillets of spur and helical gear teeth as gears pass through the meshing region. In Chapter 5, the magnitude of tensile fillet strains determined using this method will be compared to results obtained from an experimental investigation. The location of the maximum fillet strains produced by this method will also be compared to the locations given by the American Gear Manufacturer's Association (AGMA) standard, AGMA 2001-B88 [1]. A working knowledge of gearing theory is assumed and only those factors directly relevant to the fillet tensile stress determination are discussed in detail. The reader requiring further details of the geometry of spur and helical gears is referred to Colbourne [2].

The relations to be developed relate the load position, load intensity and approximate fillet tensile stresses for helical gears cut by hobs and loaded elastically. Equivalent relations for spur gears are shown to be a particular case of the helical gear relations and are presented when needed. All expressions are related to geometry and loading quantities which can be measured practically so as to permit comparison with experimental data. The notation and terminology used are that of Colbourne [2], which closely matches the notation and terminology found in AGMA 2001-B88 [1].

2.2 Load Magnitude and Position

The fillet tensile stresses developed in helical gear teeth are a function of the geometry of the gear, the magnitude of the load applied to the tooth, the position of the load in the teeth, and the total length of the gear teeth which are carrying the load. The geometry of the gear is known to the gear designers and can be determined accurately from the appropriate specifications; the design of the gears tested in this investigation is discussed in Chapter 5. While neither the magnitude of the load applied to the tooth nor the position of the load on the teeth are easy to measure in practice, they can be determined from the input torque to the gear and the rotational position.

Figure 2.1 shows an arbitrary transverse section through a set of helical gears. The driven gear is labelled "Gear 1" and the driving gear is labelled "Gear 2," and the

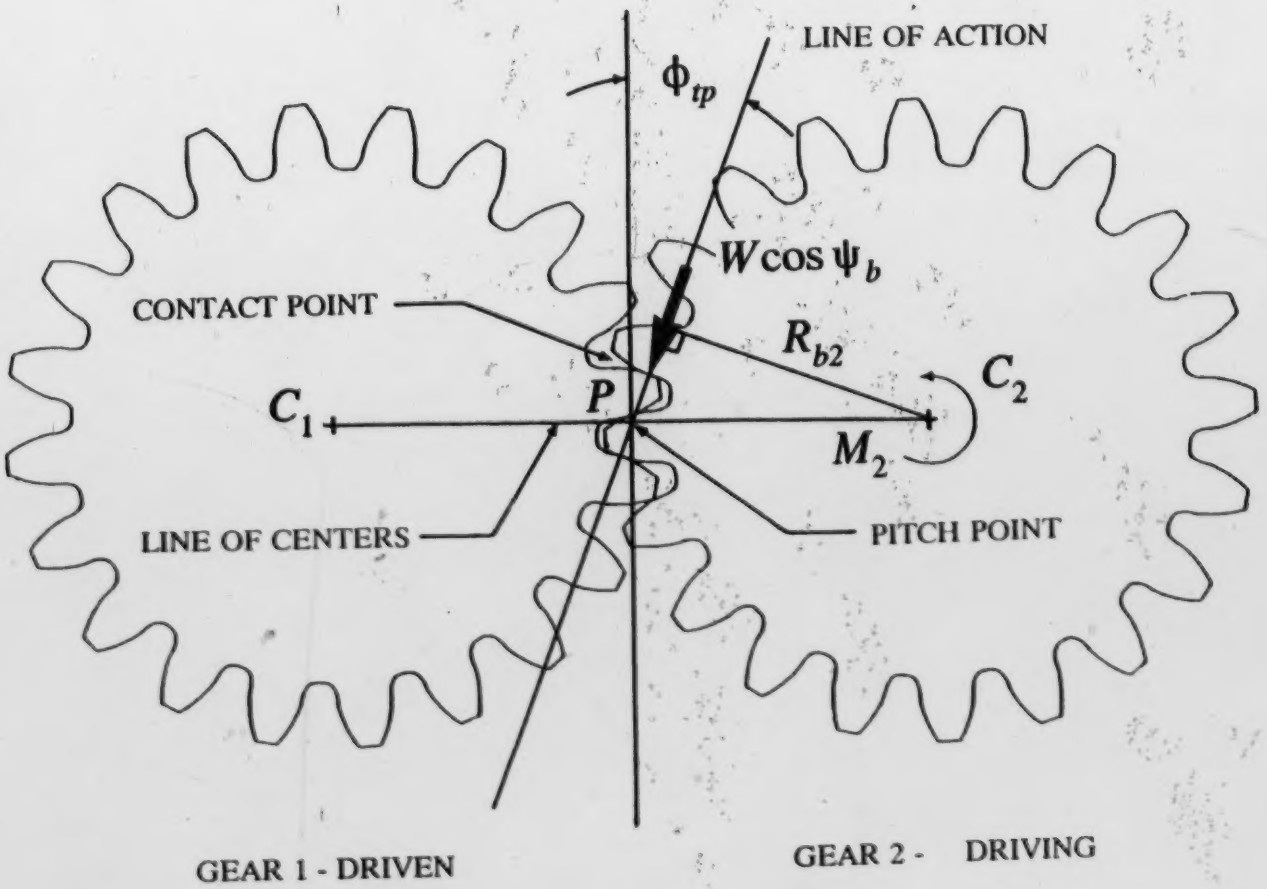

Figure 2.1 - Arbitrary Transverse Section of Two Helical Gears

gears are arranged so that the driving gear turns counter-clockwise and the driven gear, clockwise. This notation will be used throughout this thesis and is consistent with the operation of the gear testing apparatus described in Chapter 3. The input torque to the driving gear is denoted M_2.

The centers of the driven and driving gears are denoted C_1 and C_2, while the line connecting them is called the line of centers. The figure shows that one pair of teeth are in contact. The common normal to the tooth profiles at the contact point is referred to as the line of action. Since the gears are involute gears, all contact points between the gears, throughout the meshing sequence, will lie on the line of action.

The line of action passes through the line of centers at the pitch point P, and is inclined with respect to the normal to the line of centers passing through P at an angle of ϕ_{op}, the operating pressure angle. The total tooth force will be denoted W, and has a component in the transverse plane of $W\cos\psi_b$, where ψ_b is the base helix angle. This component of the total tooth force lies on the line of action. The total tooth force, therefore, can be determined from the torque applied to the driving gear:

$$W = \frac{M_2}{\cos\psi_b \, R_{b2}} . \tag{2.1}$$

In order to develop a means for expressing the position of the contact point along the line of action, it is necessary to examine the meshing region of the gear more closely. Figure 2.2 shows the two teeth from Figure 2.1 which are in contact; these teeth have been designated "Tooth 2A" for the driving gear and "Tooth 1A" for the driven gear. The contact point between the teeth is shown along with the pitch point and the line of centers. A line segment is shown which is coincident with the line of action. While the line of action represents a direction along which the contact force between the teeth must lie, the line segment in this figure, known as the path of contact, is the actual locus of all possible contact positions between the teeth. The limits of the path of contact for the gears are denoted "A" and "B." As the driven gear turns, the first contact point between Tooth 2A and Tooth 1A will occur at A. Tooth 2A, subsequently, will drive Tooth 1A through the meshing region with the last contact between the teeth (in this transverse

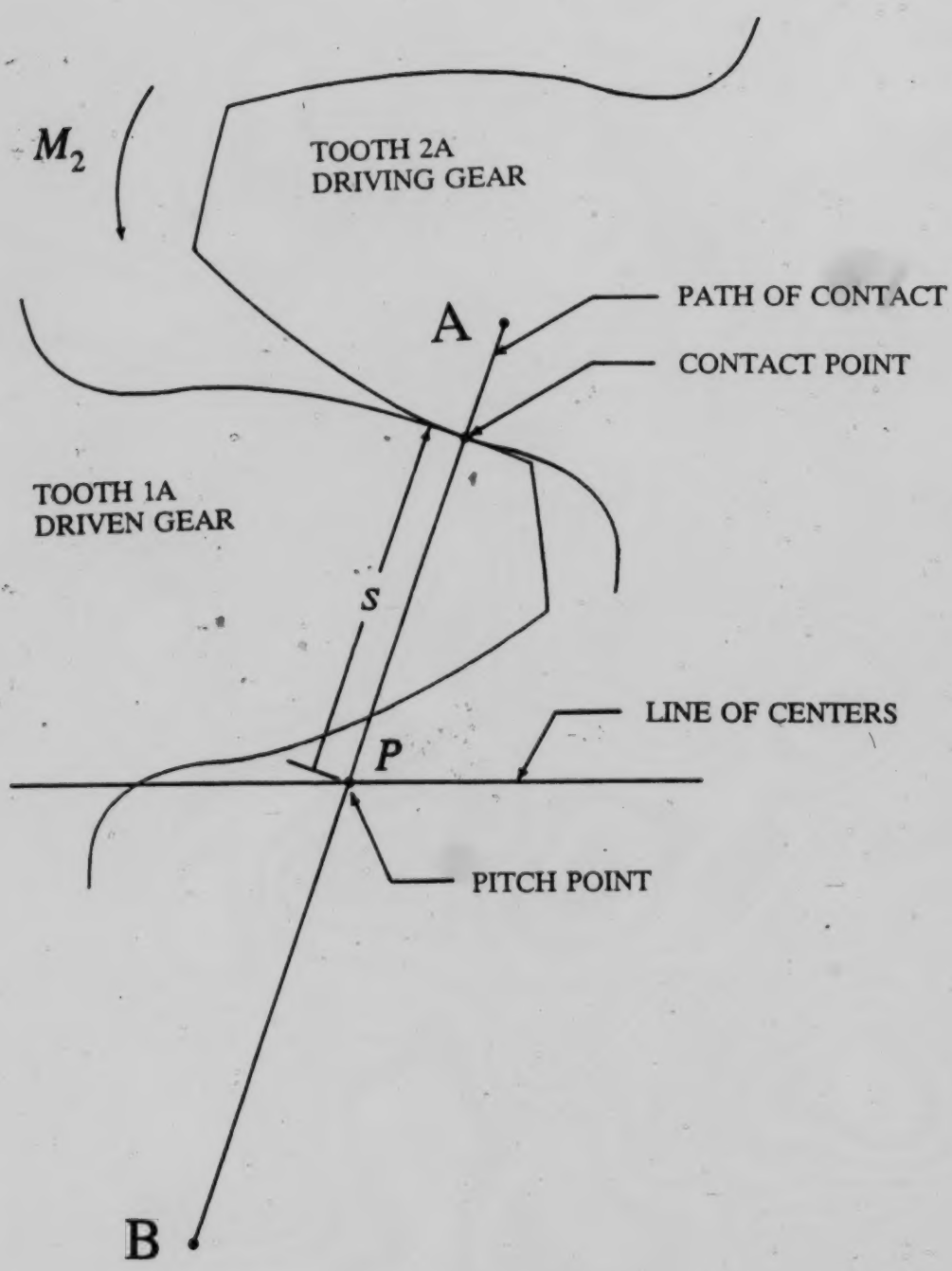

Figure 2.2 - Description of Contact Point Location Along the Path of Contact

plane) being at B.

The coordinate s, defines the location of the contact point along the path of contact. The coordinate origin lies at the pitch point and is defined such that contact points above the pitch points have positive s values while contact points below the pitch point have negative s values. Extreme values of s are illustrated in Figure 2.3 which shows the progression of a pair of gear teeth through the meshing region. Figure 2.3A shows the instant when driving Tooth 2A has just came into contact with driven Tooth 1A. For this case, s has its maximum value s_{max} and the Tooth 2A is said to be entering the contact region. Figure 2.3B shows the gears meshed at the pitch point $s = 0$. Finally, as Tooth 2A is on the verge of becoming disengaged from Tooth 1A, the bottom end of the path of contact is reached at the point where $s = s_{min}$. At this time, Tooth 2A is said to be leaving the contact region.

The counter-clockwise angular rotation of the driving gear from one position to another will be denoted as $\Delta\beta_2$. As the gear undergoes this rotation, the contact point will move down the path of contact. The change of contact position along the path of contact will be denoted as Δs. The rotation of the gear and the displacement of the contact point along the path of contact can be related as follows:

$$\Delta s = R_{b2}\Delta\beta_2. \tag{2.2}$$

where R_{b2} is the base radius of the driving gear.

2.3 Load Intensity

In Section 2.2, a method was presented for determining the total tooth force, W, from the input torque to a gear pair. While convenient for explaining various gearing concepts, the total tooth force is fictitious since, in reality, the tooth force is distributed across those gear teeth in contact. A more correct representation of how the forces present in a pair of meshing gears are distributed is accomplished with the use of load intensity. The load intensity is a measure of the portion of the total tooth force carried by each unit length of the tooth contact line. The total length of tooth surface in contact

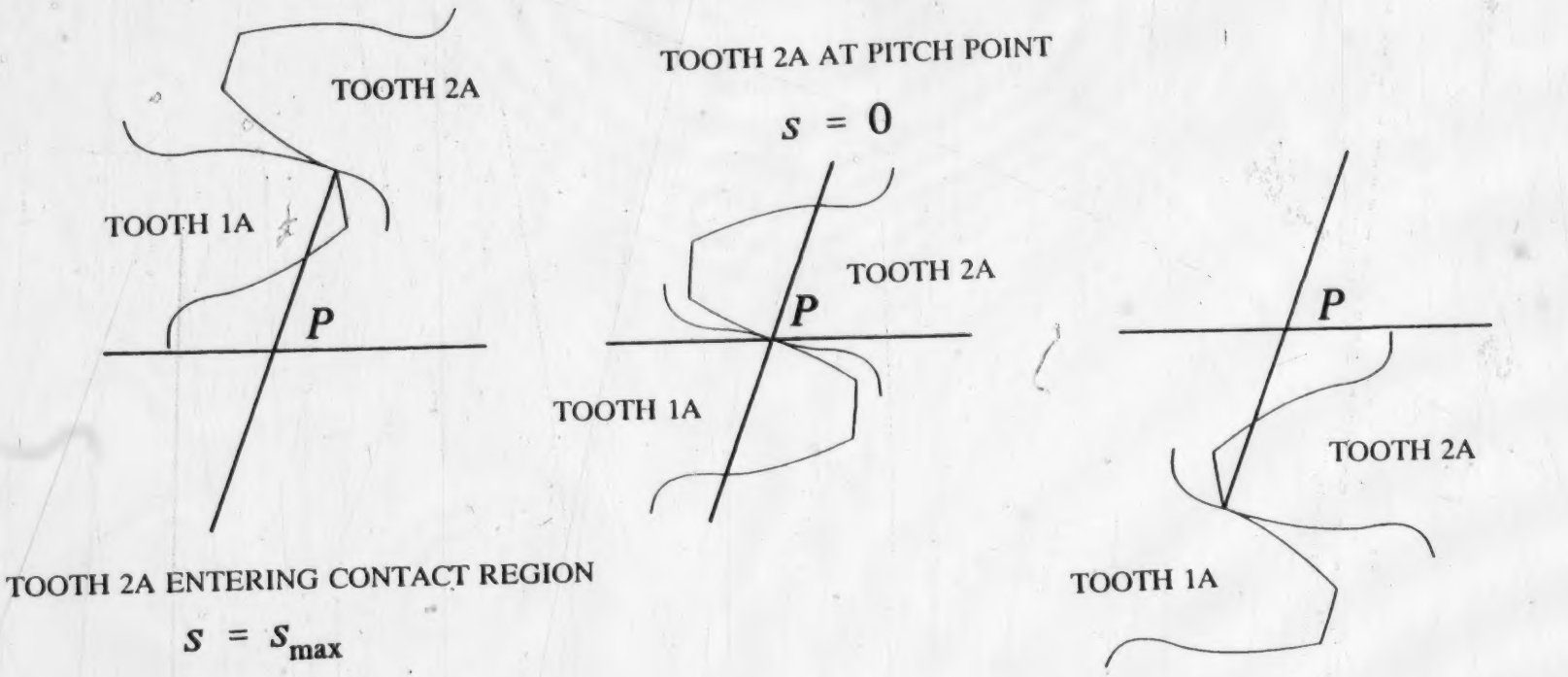

Figure 2.3 - Progression of Gear Teeth Through the Meshing Cycle

is referred to as the total contact length and is denoted as L_{TOT}. The load intensity, denoted w, is expressed as follows:

$$w = \frac{W}{L_{TOT}}. \tag{2.3}$$

In order to determine analytically the load intensity, the following assumptions are made:

1. The value of the load intensity will be assumed to be constant at all locations where the teeth are in contact.
2. In practice, the total contact length for the gear often is different from the calculated length as a result of gear manufacturing and installation errors, and of intentional crowning of the teeth. These errors also result in non-uniform load intensity values along the contact lines. In this derivation, any non-uniformity in load intensity caused by gear manufacturing and/or installation errors is ignored.

Since the value of W is known from Equation 2.1, the determination of the load intensity only involves the determination of the total contact length. Figure 2.4 shows an arbitrary transverse section through a pair of helical gear teeth in contact. Teeth 2A of the driven gear and 2B of the driving gear contact Teeth 1A and 1B, respectively, of the driven gear. The path of contact is shown and its length is given as follows:

$$s_{TOT} = s_{max} - s_{min} \tag{2.4}$$

The distance along the path of contact between the contact points of the adjacent teeth is equal to the transverse base pitch p_{tb}. The ratio of the length of the path of contact to the transverse base pitch is known as the profile contact ratio or transverse contact ratio:

$$m_p = \frac{s_{TOT}}{p_{tb}}. \tag{2.5}$$

The distance between helical gear teeth in the axial direction is known as the axial pitch p_z, and the face width of the gear is F. The ratio of the face width to the axial pitch is known as the face contact ratio,

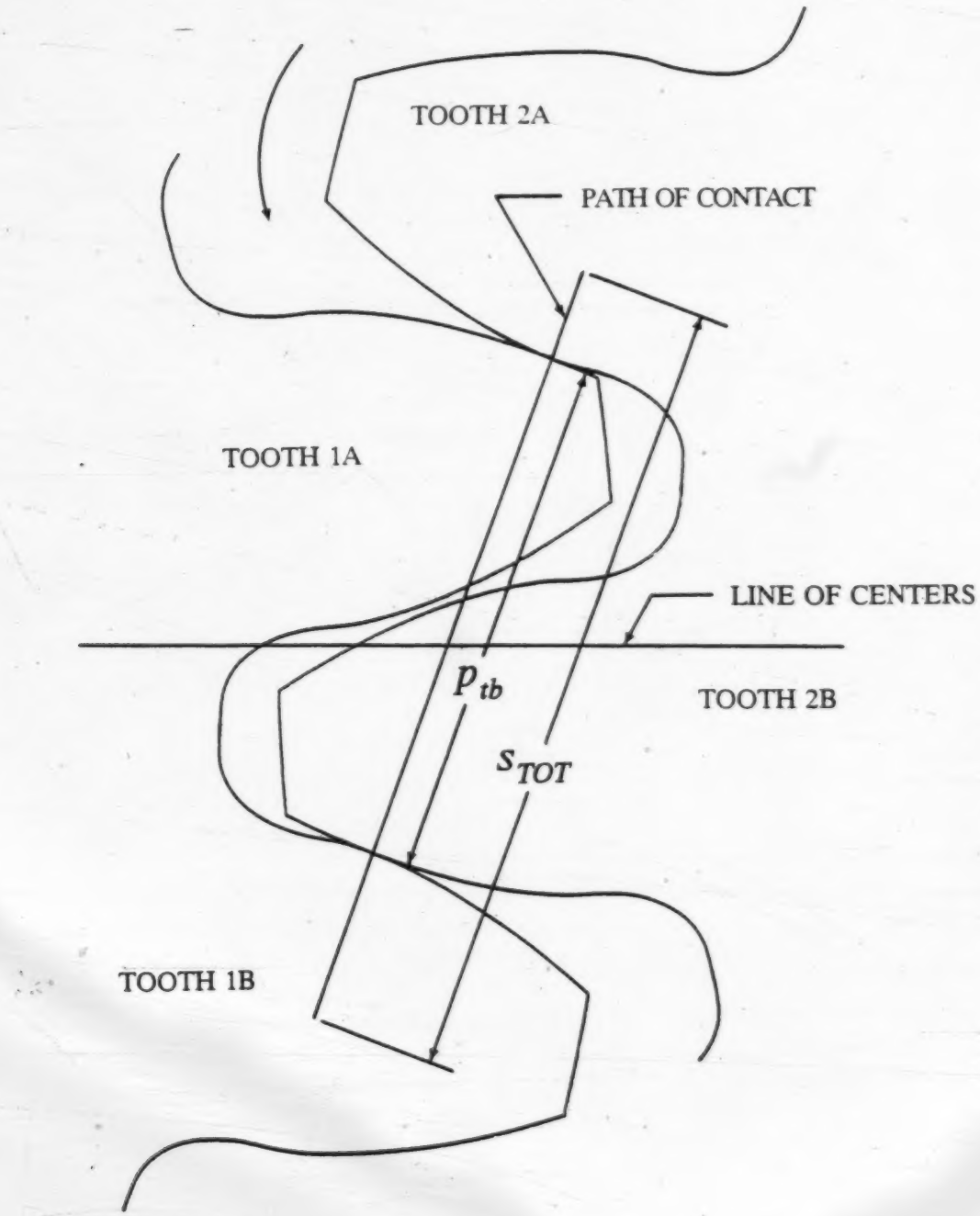

Figure 2.4 - Transverse Section Showing Two Pairs of Teeth in Contact

$$m_F = \frac{F}{p_z}. \tag{2.6}$$

The sum of the transverse contact ratio and face contact ratio is known as the total contact ratio:

$$m_c = m_p + m_F \tag{2.7}$$

The value of the load intensity and fillet tensile stresses are functions of the relative values of m_p, m_F and m_c.

The meshing diagram for a pair of helical gears is shown in Figure 2.5. The centers of the two gears C_1 and C_2 are shown as well as the line of centers, pitch point P, and line of action. The path of contact lies along the line of action between T_1 (The tip of the gear tooth is the first point of contact on the driven gear.) and T_2 (The tip of the tooth is the last point of contact on the driving gear.). Q' and Q are known as the highest and lowest points of single tooth contact and lie on the path of contact one transverse base pitch above T_2 and below T_1, respectively. The significance of these points will be discussed forthwith.

Consideration of the location of the contact point lines, thus far has focused on its position along the contact lines as expressed by either Δs or $\Delta\beta_2$ in an arbitrary transverse plane. However, as was mentioned in Chapter 1, the position of the load on each transverse section of a helical gear tooth is different, so that the determination of the total contact length requires that the position of the contact point in every transverse plane be determined. The collection of paths of contact in every transverse plane forms a rectangular region known as the plane of contact.

The plane of contact can be visualized by viewing a meshing diagram along a direction perpendicular to the path of contact as shown in Figure 2.5. The dimensions of the plane of contact will be $m_p p_{tb}$ (i.e. s_{TOTAL}) by F as shown in Figure 2.6A. The plane of contact will be bounded in the axial direction by the z-coordinates, $z = 0$ and $z = F$, and in the orthogonal coordinate by $T_1(s_{max})$ and $T_2(s_{min})$. The tip radii points, as well

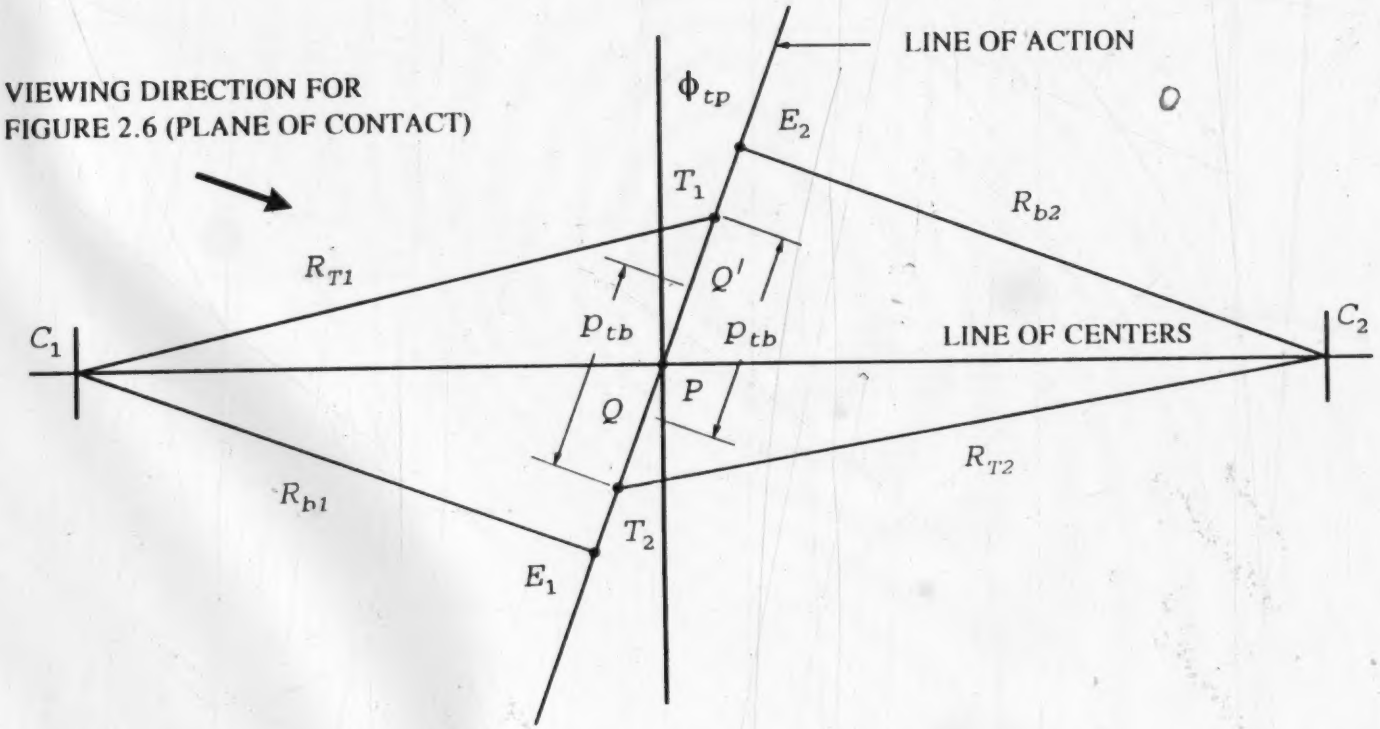

Figure 2.5 - Meshing Diagram for Two Helical Gears

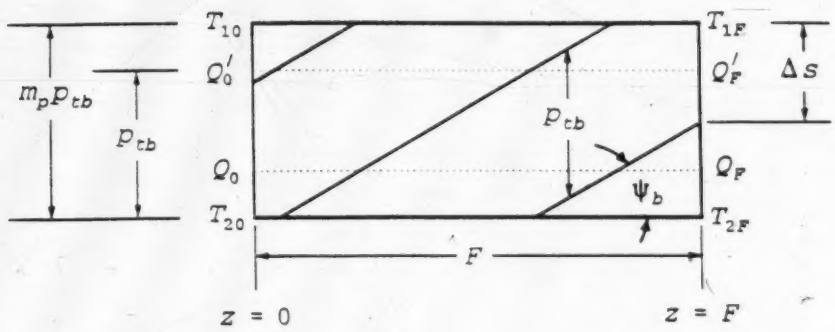

A

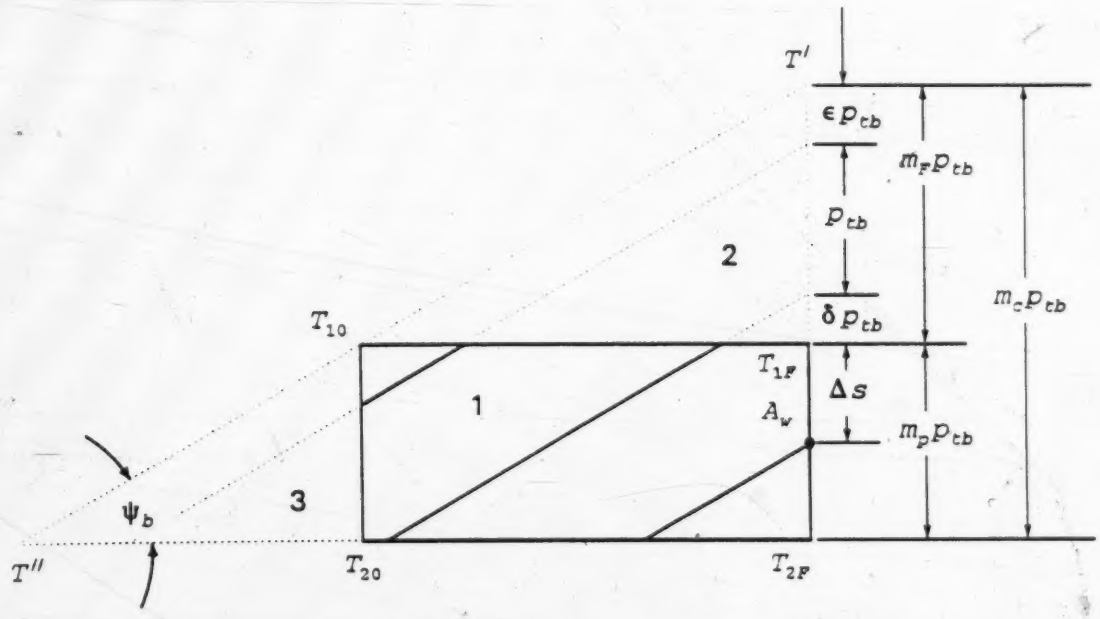

B

Figure 2.6 - Contact Region Corresponding to Figure 2.5 and Geometry Used to Determine the Length of the Lines of Contact

as the highest and lowest points of single tooth contact Q' and Q are shown with a subscript 0 in the $z = 0$ transverse plane, and F in the $z = F$ transverse plane. The collection of contact points in all transverse planes will form contact lines in the plane of contact. These lines will be inclined at an angle of ψ_b with respect to the axial direction and will be spaced at intervals of p_{tb} in the orthogonal direction. Three contact lines are shown in Figure 2.6A; one of which intersects the $z = F$ transverse plane a distance of Δs below T_{1F}. The total contact length would be the sum of the lengths of the contact lines shown.

In order to determine the total contact length in the plane of contact, T_{10}, T_{1F}, T_{2F}, T_{20}, a triangle comprising points T', T_{2F}, T'' and denoted by Triangle 1 is constructed around the plane of contact, as shown in Figure 2.6B. This triangle is constructed by extending the contact lines, so that they intersect a line extending from $T_{20} - T_{2F}$ and the $z = F$ transverse plane. An additional line is added parallel to the contact lines which passes through T_{10} and intersects the extension of $T_{20} - T_{2F}$ at T'' and intersects the $z = F$ transverse plane at T'. The extension of the contact line closest to T_{10}, in the plane of contact, intersects the $z = F$ transverse plane a distance of ϵp_{tb} below T' where ϵ has a value between zero and one. The determination of the contact length involves determining the lengths of the actual and extended lines of contact in Triangle 1 and subtracting the lengths of the extended lines of contact in triangles T', T_{1F}, T_{10} (Triangle 2) and T_{10}, T_{20}, T'' (Triangle 3). The distance from T' to T_{1F} is $m_F p_{tb}$, so the distance from T' to T_{2F} is given by Equation (2.7) as $m_c p_{tb}$. The number of contact lines in Triangle 1 is one greater than the integer portion of $(m_c - \epsilon)$. The number of contact lines will be defined n_c and is expressed as follows:

$$n_c = INT(m_c - \epsilon) + 1 \tag{2.8}$$

where *INT* is the BASIC function *INT(x)* which returns the largest integer less than or equal to x. The length of the longest contact line in the triangle is $(m_c - \epsilon)p_{tb}/\sin\psi_b$. The total length of the lines in Triangle 1 is given by:

$$L_1 = \frac{p_{tb}}{\sin\psi_b}(n_c)(m_c - \epsilon - 0.5(n_c - 1)). \tag{2.9}$$

The lengths of the extended contact lines in Triangles 2 and 3 are, therefore,

$$L_2 = \frac{p_{tb}}{\sin\psi_b}(n_F)(m_F - \epsilon - 0.5(n_F - 1)) \tag{2.10}$$

$$L_3 = \frac{p_{tb}}{\sin\psi_b}(n_p)(m_p - \epsilon - 0.5(n_p - 1)). \tag{2.11}$$

The total contact length is given by:

$$L_{TOT} = L_1 + L_2 + L_3 \tag{2.12}$$

Colbourne [2] has examined the values of L_{TOT} for various positions of the contact lines in the plane of contact. The total contact length is a minimum when the contact occurs at points Q'_{1F} and T_{2F} on the driven gear. Correspondingly, the maximum contact length will occur when the contact occurs at points T_{1F} and Q_F on the driven gear. The relationship between the contact length, load position, and tensile fillet stress will be examined in Section 2.5 for different classes of gears.

Using Equation 2.12, the total contact length may be determined as a function of ϵ. However, it would be more convenient to express L_{TOT} in terms of the position of the first contact point that enters the contact plane as defined by s. In Figure 2.6B, it is apparent that ϵ can be defined in terms of the distance below T_{10} at which a contact line intersects the $z = 0$ transverse plane. The value of total contact length is the same if we define ϵ in terms of the distance that a point at the intersection of a contact line and the $z = F$ transverse plane lies above Q'_F. The distance from the pitch point to Q'_F is constant and equal to $(1 - 0.5m_p)p_{tb}$ for gear pairs tested in this study, so ϵ and s

may be related as follows:

$$s = (1 - 0.5m_p + \epsilon)p_{tb} \tag{2.13}$$

The load radius R_w from the center of the driven gear to the contact point A_w is determined from the gear geometry:

$$R_w^2 = R_{bl}^2 + [\sqrt{R_{Tl}^2 - R_{bl}^2} - \Delta s]^2 \tag{2.14}$$

The $z - F$ transverse plane is used as a reference for defining the contact point position throughout this thesis. By knowing the input torque to the gears and their relative angular rotation from the point of driven tooth engagement, the relations developed in this section can be used to determine the load position and intensity throughout the meshing cycle.

2.4 Equivalent Spur Gear

The expressions developed in the preceding sections allow the total contact length to be determined from the position of the contact point in the $z - F$ section. The loading along the contact lines is assumed constant and, therefore, the determination of the load intensity on the helical gear teeth has been reduced to a two-dimensional problem. The difficulty in determining the fillet stresses would be reduced if a suitable two-dimensional representation of the helical gear could be devised. Use of the normal section of the helical gear to determine fillet stresses would be difficult because the shape of the helical gear tooth in the normal section is neither symmetrical nor easy to calculate.

In order to represent accurately the geometry of a helical gear in two-dimensions for the purposes of stress calculation, AGMA 2001-B88 [1] uses the concept of an equivalent spur gear. The equivalent spur gear is a spur gear whose tooth profile matches as closely as possible the normal tooth profile of the helical gear upon which it is based. The circular pitch, pressure angle, dedendum and addendum of the equivalent spur gear are equal to the corresponding quantities of the helical gear. It is constructed on a circle whose radius is equal to the radius of curvature of the normal helix in the pitch cylinder of the helical gear. The pitch radius and number of teeth in the equivalent spur gears are

determined as follows:

$$R_e = \frac{R_{sl}}{\cos^2\psi_s} \tag{2.15}$$

$$N_e = \frac{N}{\cos^3\psi_s} \tag{2.16}$$

where the subscript, e, will be used to denote equivalent spur gear, and ψ_s is the helix angle at the standard radius. The tooth profiles and fillet shapes of the equivalent spur gear are assumed to have been cut by the same hob which cut the helical gears. In Chapter 5, the specifications of the hob which was used to cut the gears tested in this thesis will be presented. Using the values of the quantities defined in Equations 2.15 and 2.16, the profile of the equivalent spur gear tooth and fillet may be defined fully. While the profiles are not identical to the normal tooth and fillet profiles of the helical gears, the differences are too small to affect the magnitudes of the tensile fillet stresses.

2.5 Helical and Spur Gear Tensile Fillet Stresses

Using the expressions for load intensity as a function of load position, as developed in Section 2.3, and the geometry of the equivalent spur gear, as described in the previous section, it is possible to determine the tensile fillet stresses of the helical gear. In Figure 2.7, the geometry and loading on an equivalent spur gear is shown. A coordinate system, (x, y) originates from the center of the gear with the x-axis passing through the centerline of the tooth and the y-axis orthogonal to it in the transverse plane. The load intensity w is shown acting at point $B(x_w, y_w)$ which is located at radius R_{we} from the gear's center. The profile angle ϕ_w, at point B, the polar angular coordinate θ_w, of B, and their difference γ_w, are all shown. The intersection of the extension of the load intensity vector and the x-axis is labelled $(x_D, 0)$. The tensile fillet stresses in the gear tooth will be calculated at $A(x, y)$. The position of A lies between the root radius of the tooth and the fillet radius - the lowest point on the involute profile of the gear tooth. The determination of (x, y) coordinates for points on the tooth profile and on the fillet is a function of hob tooth geometry and is not discussed here. The tensile

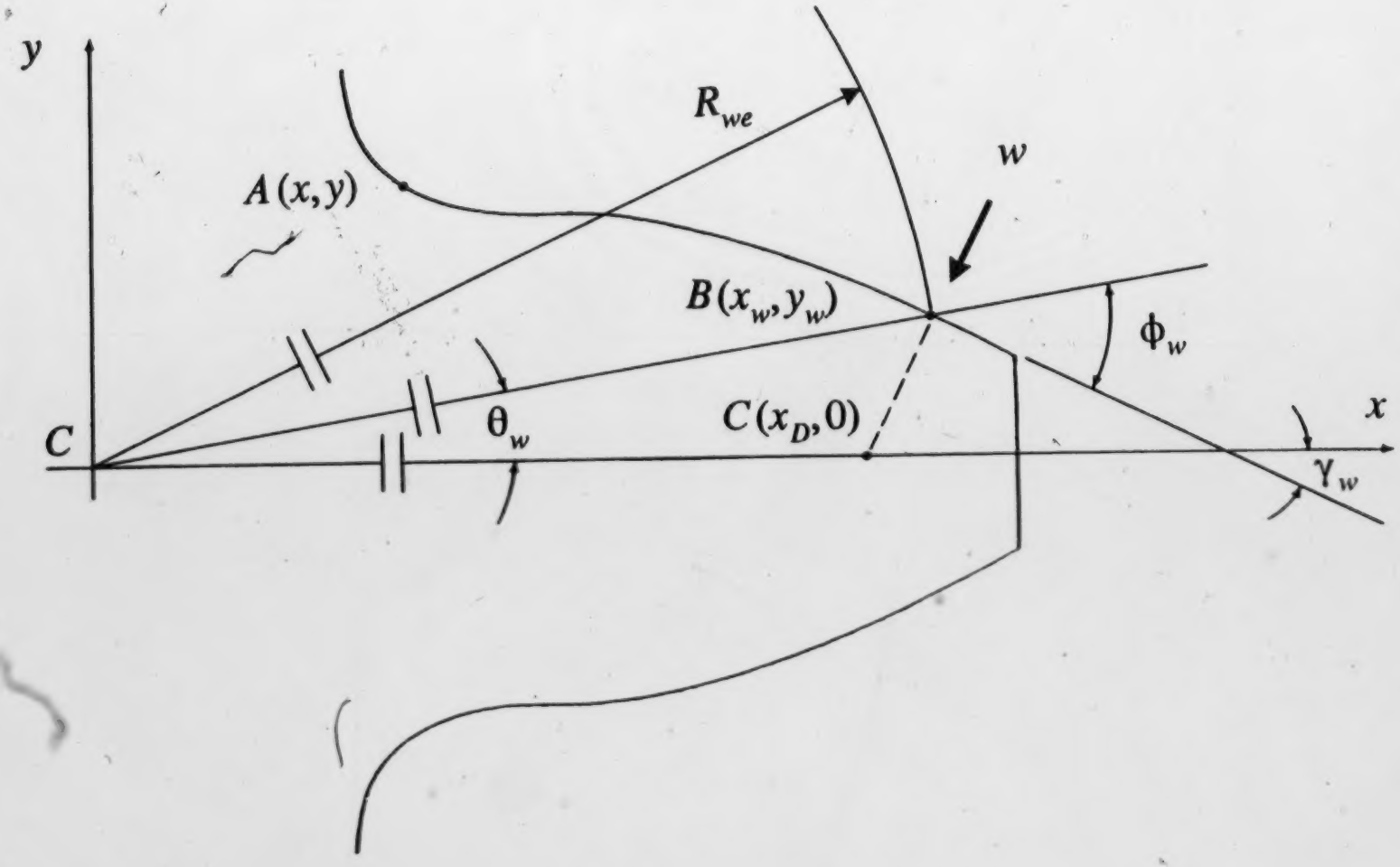

Figure 2.7 - Geometry of and Loading on a Driven Equivalent Spur Gear Tooth

bending stress σ_t at A can be approximated first by assuming that the gear tooth is a rectangular cantilever beam of length $(x_D - x)$, depth z_1, and width (1). It is given by the following equation,

$$\sigma_t = \frac{w}{m_n} \cos\gamma_w \left[\frac{1.5m_n(x_D - x)}{y^2} - \frac{0.5m_n \tan\gamma_w}{y}\right] \tag{2.17}$$

Two modifying factors are required to allow Equation 2.17 to express properly the tensile fillet stress. First, a stress concentration factor exists in the fillet which would not be present in a rectangular cantilever beam. This stress concentration factor takes the form:

$$K_f = k_1 + \left(\frac{2y}{r_f}\right)^{k_2} \left(\frac{2y}{x_D - x}\right)^{k_3} \tag{2.18}$$

where r_f is the fillet radius of curvature which is a function of gear and hob geometry and k_1, k_2, and k_3 are constants which are based on the results of photoelastic tests performed by Dolan and Broghamer [3].

The contact lines which cross the faces of helical gear teeth are straight and not at a constant radius. When the same load intensity is transferred to the teeth of the equivalent spur gear, the contact lines on the teeth become curved. Wellauer and Seireg [4] studied the bending moment in a cantilever plate caused by an oblique load across its surface. Their work produced a dimensionless quantity C_h, which is the ratio of the bending moment which would occur if the load was applied along the top edge of the plate divided by the bending moment arising from the oblique load. C_h is known as the helical factor and is a function of the helix angle and the transverse pressure angle. Colbourne [5] has determined that the values for the helical factor produced by the formula given in AGMA 2001-B88 are incorrect, and has offered an alternate method for its calculation. This method will be used for the determination of theoretical tensile fillet strains in Chapter 5.

The stress intensity and helical factors may be directly incorporated into Equation 2.17.

$$\sigma_t = \frac{w}{m_n} \cos\gamma_w \left[K_f\left(\frac{1.5m_n(x_D - x)}{C_h y^2} - \frac{0.5m_n \tan\gamma_w}{y}\right)\right] \tag{2.19}$$

Equation 2.19 gives the tensile stresses at point A in the fillet of the helical gear as a function of load intensity. Since the load across the teeth in the spur gear is at a constant radius $C_h = 1$, the tensile fillet stresses for a spur gear are given as follows:

$$\sigma_t = \frac{w}{m}\cos\gamma_w\left[K_f\left(\frac{1.5m(x_D - x)}{y^2} - \frac{0.5m\tan\gamma_w}{y}\right)\right] \qquad (2.20)$$

The tensile fillet stress given in Equation 2.20 may be converted to a tensile fillet strain by using stress strain relations. Tensile fillet strains produced in this manner will be compared to experimentally measured strains in Chapter 5.

2.6 Load Position, Intensity, and Maximum Fillet Stresses for Different Classes of Gears

2.6.1 Spur Gears

Figure 2.8 shows the plane of contact for a typical pair of spur gears. The contact between the spur gears occurs along a straight line at a constant radius, so the contact lines shown in Figure 2.8A are parallel to the top and bottom of the plane of contact. The spacing between the contact lines is equal to the base pitch and the contact lines are shown with Contact Line 1 at position s along the path of contact. The notation used in Figures 2.8 is the same as the notation used in Figures 2.5 and 2.6. The total length of the contact lines is $2F$ and, as stated in Section 2.3, the total length of the contact lines is a maximum and the load intensity a minimum when Contact Line 2 passes through Q'_F. As the driven gear rotates, the distance s to Contact Line 2 will decrease and the contact lines will move down the plane of contact. The total contact length and load intensity will remain constant and, therefore, the tensile fillet stress will decrease as the load radius decreases. When Contact Line 2 reaches Q'_F, Contact Line 1 will reach T_{2F} and leave the plane of contact. At this point, Driven Tooth 2 (associated with Contact Line 2) will be carrying the entire load. For this reason, Q'_F is referred to as the highest point of single tooth contact. For the geometry shown, the load intensity at Q'_F will be twice the value and the fillet tensile stress of Tooth 2 will be essentially twice

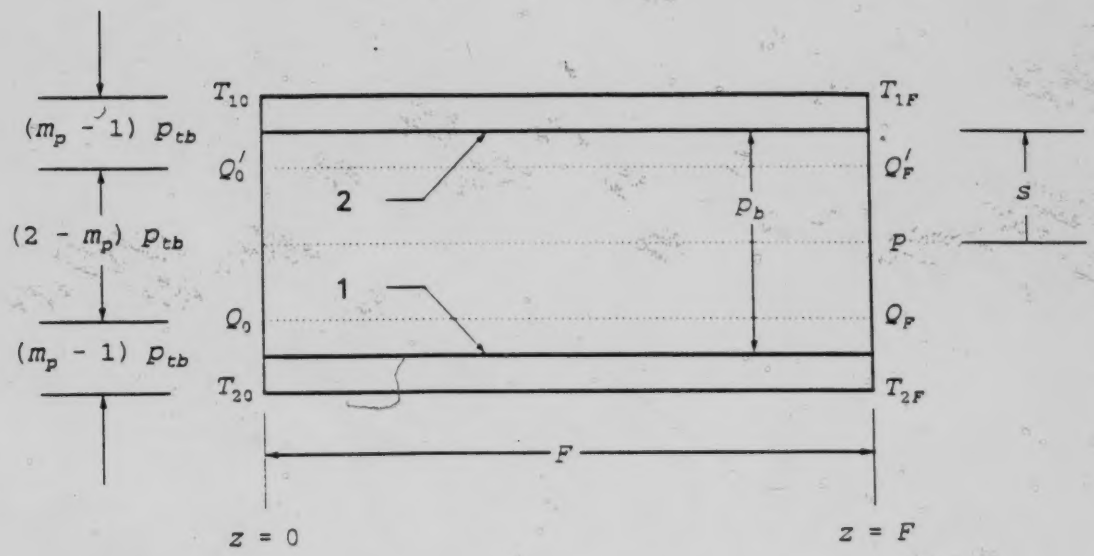

A

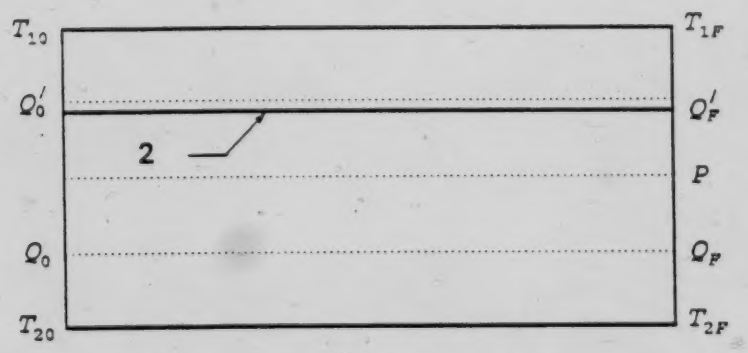

B

Figure 2.8 - Contact Region when $m_p = 0$

the value of the corresponding quantities before Q_F'. The large change in load intensity observed when passing through the highest point of single tooth contact is a phenomenon common to all spur gears. The increase in fillet tensile stresses associated with the large change of load intensity exceeds the increase in fillet tensile stress which occurs as the load radius increases due to contact point movement from the highest point of single tooth contact to the gear tip. As a result, the maximum fillet tensile stress occurs when the load is applied to the highest point of single tooth contact. At this point, the total contact length is given by:

$$L_{TOT} = F \tag{2.21}$$

and the load radius is given by

$$R_w^2 = R_b^2 + [(\sqrt{R_T^2 - R_b^2}) - (m_p - 1)p_b]. \tag{2.22}$$

As the gear rotates, the remaining Contact Line 2 will continue to move down the plane of contact as indicated by Figure 2.8B. The load intensity will remain constant and the tensile fillet stress will decrease until Contact Line 2 aligns with Q_F. This point, known as the lowest point of single tooth contact, is the lowest point through which a contact line may pass without the introduction of a new contact line at T_{1F}. Contact Line 2 will continue to move down the plane of contact until it exits at T_{2F}.

2.6.2 Helical Gears with $m_F \leq (2 - m_p)$

This first class of helical gears to be considered are those gears which have only one pair of teeth in contact during some parts of the meshing cycle. The contact plane for such a gear pair is shown in Figure 2.9A. The projected length along the $z = F$ transverse plane of a contact line for this gear is shown as $m_F p_{tb}$. In order that only one pair of gear teeth be in contact at some time during the meshing cycle, the projected length must be less than the distance between the highest and lowest points of single tooth contact. This distance can be determined from Figure 2.6A as $(2 - m_p)p_{tb}$. Consequently, gears satisfy this condition as long as $m_F \leq (2 - m_p)$. One class of gears

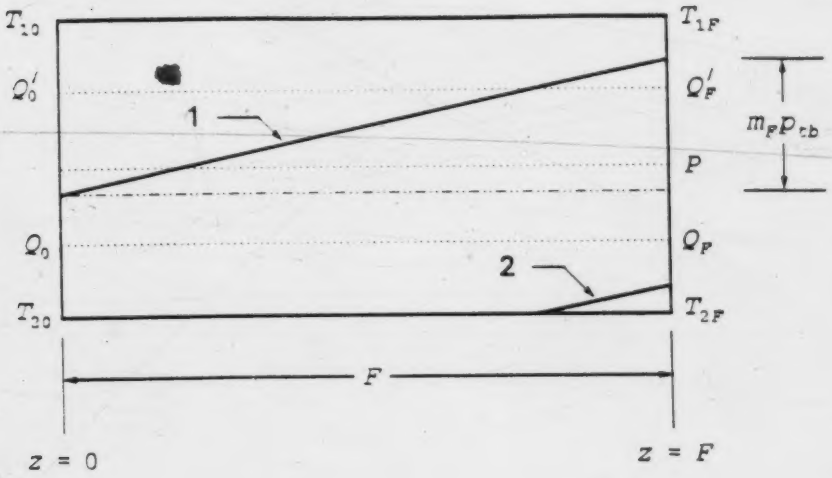

A

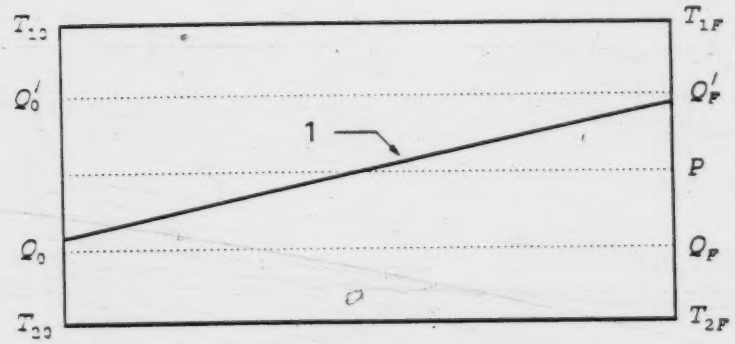

B

Figure 2.9 - Contact Region when $m_p \leq (2 - m_p)$

which satisfy this condition is spur gears, consequently, many of the ideas presented in the previous section are valid here. The highest and lowest points of single tooth contact remain valid; although they only apply to contact in a particular transverse plane. Figure 2.9A shows two contact lines at a time shortly after Contact Line 1 has passed T_{1F}. When Contact Line 1 passed through T_{1F} the contact length was a maximum and the load intensity a minimum. During the interval when Contact Line 1 moves downward from T_{1F} through the position shown in Figure 2.9A to Q_F', the contact length decreases. At Q_F', Contact Line 2 leaves the plane of contact. At this point, the total contact length is a minimum and the tensile fillet stress is a maximum. The total contact length is given by,

$$L_{TOT} = \frac{F}{\cos\psi_b}$$

and the load radius by

$$R_w^2 = R_b^2 + [\sqrt{(R_T^2 - R_b^2)} - (m_p - 1)p_{tb}]^2. \tag{2.23}$$

Contact Line 1 will remain the only contact line in the plane of contact until the left side of this contact line intersects Q_0. As the left side of Contact Line 1 moves below Q_0, a contact line will appear at T_{10} and the total contact length will begin to increase. It will be a maximum when the left side of the contact line passes through T_{20}.

2.6.3 Helical Gears with $(2 - m_p) < m_F \leq 1$

The next class of helical gears to be considered are those whose contact length, when projected on the $z = F$ transverse plane, is between $(2 - m_p)p_{tb}$ and p_{tb}. These conditions are met by helical gears with face contact ratios between $(2 - m_p)$ and 1. Figure 2.10A shows two contact lines on the plane of contact of such a gear. Contact Line 2 is approaching Q_0 on the $z = 0$ transverse plane and Contact Line 3 intersects the $z = F$ transverse plane between Q_F and T_{2F}. When Contact Line 2 passes through

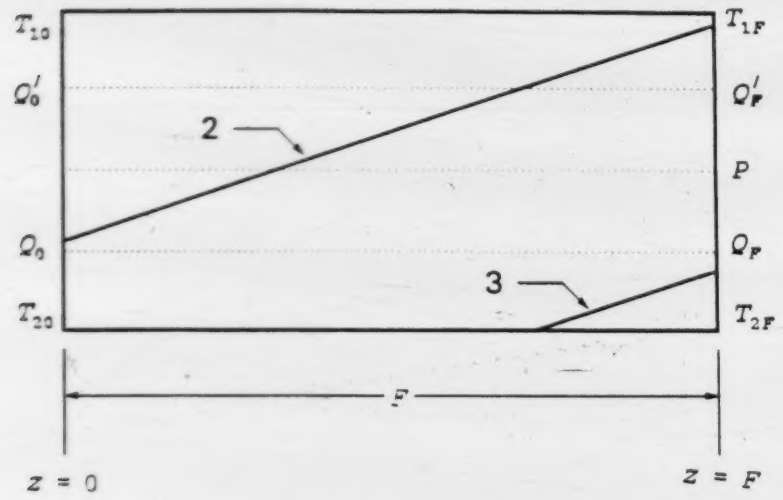

A

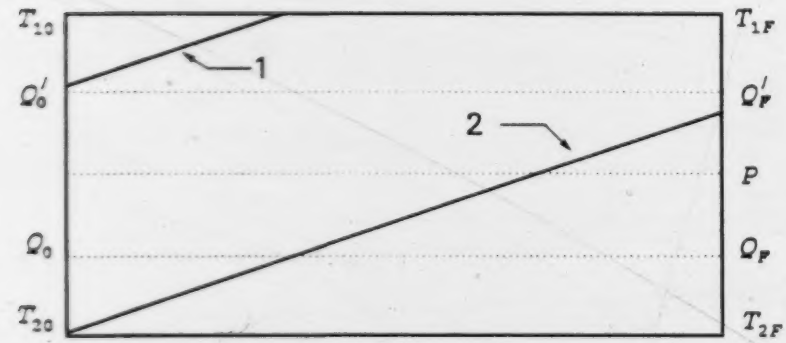

B

Figure 2.10 - Contact Region when $(2 - m_p) < m_F < 1$

Q_0, the total contact length will be a minimum and the load intensity a maximum. The contact line passing through Q_0 will intersect the z - F transverse plane at a distance of $(1 - m_F)p_{tb}$ below T_{1F} and the tensile fillet stress will be a maximum. The total contact length will be:

$$L_{TOT} = \frac{F}{m_F \cos\psi_b}(2m_F + m_p - 2) \tag{2.24}$$

and the load radius will be:

$$R_w^2 = R_b^2 + [\sqrt{(R_T^2 - R_b^2)} - (1 - m_F)p_{tb}]^2. \tag{2.25}$$

The wide variation of total contact length and load intensity through the meshing cycle for spur gears and helical gears with $m_F < 1$ is the dominant and controlling factor for the value of the tensile fillet stresses. This is why the maximum tensile fillet stresses occur when the total contact length is a minimum. The smooth variation of total contact length for helical gears with face contact ratios less than 1 with respect to spur gears accounts for the smoother and quieter operation of these gears in practice.

2.6.4 Helical Gears with $m_F > 1$

This classification of gears encompasses most normal helical gear designs. The meshing diagram for such a gear pair is shown in Figure 2.11. Figure 2.11A shows four contact lines: one entering the mesh (Contact Line 2), two complete contact lines (Contact Lines 3 and 4) and one contact line leaving the mesh (Contact Line 5). The term, "complete contact lines," refers to the fact that the contact line runs from the tip of the driving gear to the tip of the driven gear. This condition will occur when $m_F > m_p$. As the gears rotate, the contact lines will move down the plane of contact until Contact Line 4 touches T_{1F}. When a contact line passes through T_{1F}, the total contact length will be a maximum and the load intensity will be a minimum. At this position, the load radius is a maximum and is the governing factor in the tensile fillet stress. Consequently, the maximum fillet stress will be a maximum for the case of corner tooth loading. As the gear turns further, Contact Line 5 leaves the gear mesh and

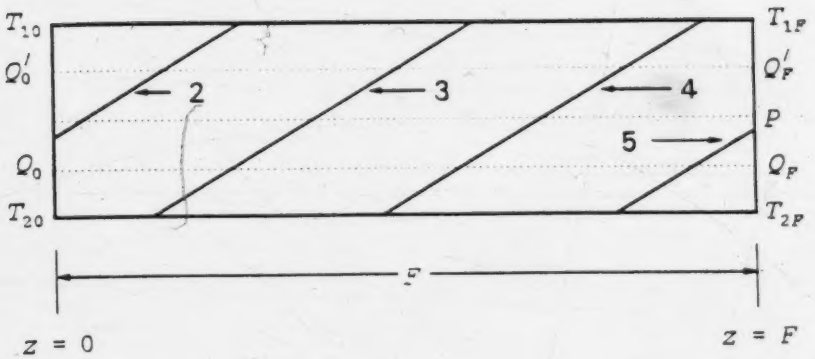

A

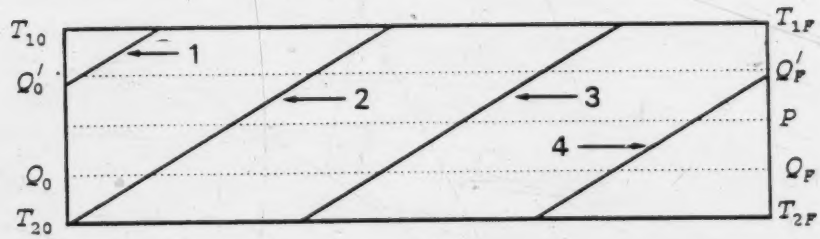

B

Figure 2.11 - Contact Region when $m_P > 1$

Contact Line 1 enters the mesh as shown in Figure 2.11B. Because two complete contact lines are in the plane of contact at any time, the percentage change of total contact length caused by the entry of contact lines into the mesh or the exit of contact lines from the mesh is reduced. For this class of gears, the smaller variations in total contact length will result in the magnitude of the maximum tensile stress being controlled by load position, not load intensity.

2.7 AGMA 2001-B88

American Gear Manufacturers Association's standard AGMA 2001-B88 [1] gives rules for the determination of contact and tensile fillet stresses in spur and helical gear teeth. The standard uses the concept of the equivalent spur gear described in Section 2.4 to model the load on a three-dimensional helical gear as a load intensity applied to the transverse section of a spur gear. The formulation of AGMA 2001-B88 [1] is not presented in this thesis, except to indicate that the standard calculates an ideal fillet stress and then modifies it to account for practical factors such as gear misalignment, service overloads, design life and anticipated reliability. These factors are discussed as required in Chapter 5.

The method used to calculate tensile fillet stresses, presented earlier in this chapter, and the method used in AGMA 2001-B88 [1] differ in terms of their assessment of the load location and load intensity causing maximum fillet stresses for different classes of gears. For spur gears, both methods agree that for accurately cut gears, the maximum tensile fillet stress occurs when the load is applied at the highest point of single tooth contact and the load intensity is a maximum. For helical gears with face contact ratios less than 2 - m_p, the method presented here agrees with the AGMA standard that the maximum tensile stresses occur when the load intensity is a maximum and the contact line passes through the highest point of single tooth contact. For helical gears with face contact ratios between 2 - m_p and 1, both methods agree that the maximum tensile fillet stress occurs when the load intensity is a maximum. However, this method states that the maximum fillet stress occurs when a contact line intersects the z - F transverse plane between the tip radius and the highest point of single tooth contact, while the AGMA

standard states that the maximum stress occurs at the highest point of single tooth contact. For gears with face contact ratios greater than 1, both methods agree that the maximum fillet stress occur when the contact line passes through the tooth corner. However, the AGMA standard states that this condition occurs when the load intensity is a maximum; this method states it occurs when the load intensity is a minimum. A comparison between the two methods of the load intensity and position corresponding to maximum tensile fillet stresses for various classes of helical gears is summarized in Table 2.1.

Table 2.1 - Load Position and Intensity Values Corresponding to Maximum Tensile Fillet Stresses for Various Classes of Gears

Gear Class	Load Position	Load Intensity
Spur, $m_F = 0$		
Colbourne [2.2]	H.P.S.T.C.	Maximum
AGMA 2001-B88 [2.1]	H.P.S.T.C.	Maximum
Helical, $m_F < (2-m_p)$		
Colbourne [2.2]	H.P.S.T.C.	Maximum
AGMA 2001-B88 [2.1]	H.P.S.T.C.	Maximum
Helical, $(2 - m_p) < m_F < 1$		
Colbourne [2.2]	Between Tip Radius and H.P.S.T.C.	Maximum
AGMA 2001-B88 [2.1]	H.P.S.T.C.	Maximum
Helical, $m_F > 1$		
Colbourne [2.2]	Tip Radius	Minimum
AGMA 2001-B88 [2.1]	Tip Radius	Maximum

Notes:

H.P.S.T.C. - Highest Point of Single Tooth Contact

Chapter 3: Gear Testing Apparatus Design

3.1 Overview

3.1.1 Types of Gear Testing Apparatus

The work described in this thesis has involved the design, construction and commissioning of a multi-use gear testing apparatus for the Department of Mechanical Engineering at the University of Alberta. The apparatus was designed to perform gear research in six different areas:

1. Static Gear Stress Distribution Studies,
2. Dynamic Gear Stress Distribution Studies,
3. Gear Noise and Vibration Measurement for the Purposes of Condition Monitoring,
4. Effect of Known Manufacturing and Installation Errors on Gear Performance and Life.
5. Lubrication Studies, and
6. Endurance Testing.

In order to conduct these tests, two classes of gear testing apparatus were considered.

The first class of gear testing apparatus considered was the open-loop design shown in Figure 3.1. This design features a drive motor which supplies power to the test gears either directly or through a reducer. The power transmitted through the gears P_T, is the product of the drive motor torque and the speed $P_T = T_M \omega_M$. The power is dissipated by system losses and a load such as a generator. The test gears are usually supported on four bearings and enclosed in a housing.

The primary advantages of this design are that it is mechanically simple and the test gears can be replaced and aligned with comparative ease. The primary disadvantage of the design is that the drive motor and load must be sized to provide the total desired gear testing power. As a result, in order to realistically test even small industrial gears, large drive motors and loads would be required. In a university setting, this could represent problems in terms of increased capital cost, installation cost, maintenance and potential noise and vibration problems during testing. Additionally, if a constant speed motor is being used to drive the apparatus, only one transmitted power level is possible without an expensive multi-speed reducer.

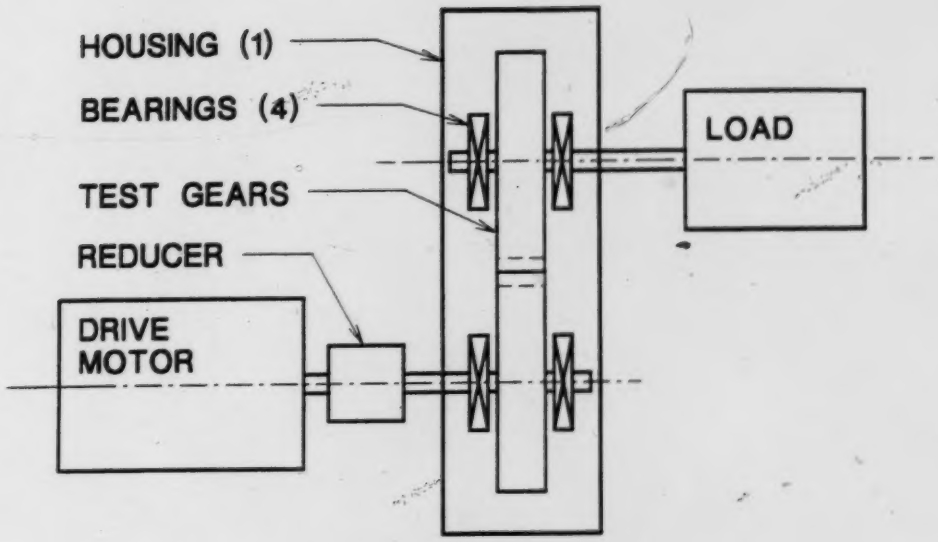

Figure 3.1 - Open Loop Gear Testing Apparatus Schematic

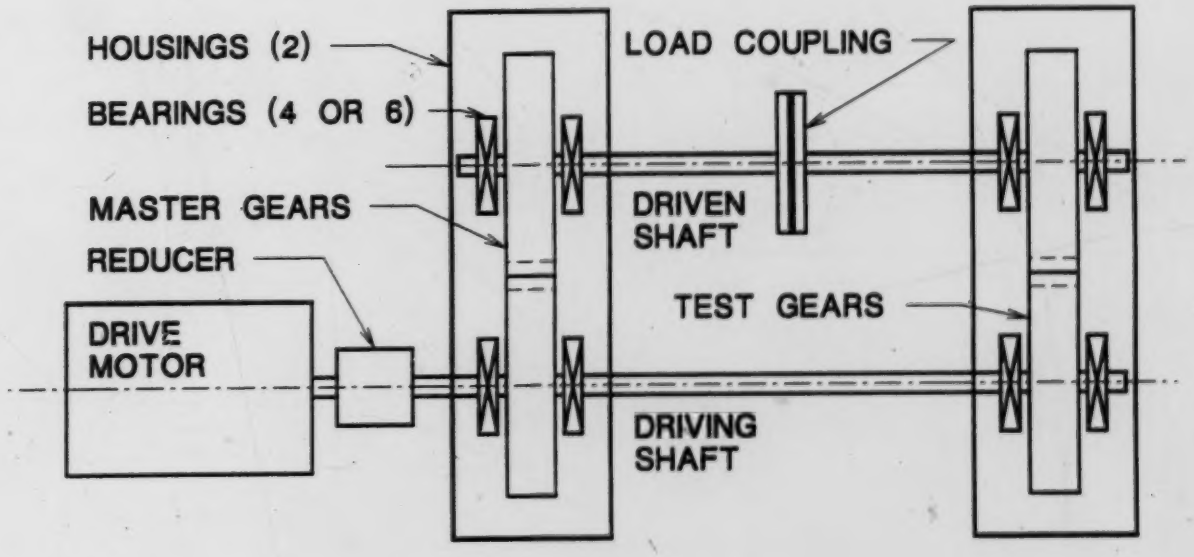

Figure 3.2 - Recirculating Power Loop Gear Testing Apparatus Schematic

The second class of gear testing apparatus considered was the recirculating power design. This design is alternatively known as the closed power-loop, four square or back-to-back design. The major components of this design are shown in Figure 3.2. Power is supplied again by the drive motor which is coupled to an optional reducer. The apparatus consists of two shafts, designated the driving and driven shafts, on which two pairs of gears are mounted. The two gear pairs are designated the master and test gears. The test gears are those gears for which an investigation is being conducted. The master gears are designed to be of high quality and strength, so as to not adversely affect the operation of the test gears. A device known as a load coupling is installed on the driven shaft between the master and test gears. The purpose of the load coupling is to introduce a torque T, to the master and test gears independent of the drive motor. This torque may be locked into the gears by mechanical means prior to testing or it may be varied as the apparatus turns by means of a hydraulic device. It is apparent that the drive motor of a recirculating power gear tester does not supply the torque to the test gears, only rotation. The transmitted power can be thought to be circulating between the master and test gears and is known as the recirculating power P_R. The recirculating power can be denoted as follows:

$$P_R = T\,\omega_m. \tag{3.1}$$

The amount of power required to turn a recirculating power gear testing apparatus at constant speed is equal to the power required to overcome system losses: bearing friction, gear meshing losses, losses associated with lubrication method and windage. The maximum recirculating power which can be achieved by a recirculating power gear testing apparatus is given as follows:

$$P_{R_{MAX}} = \frac{P_M}{\eta_L}. \tag{3.2}$$

where $P_{R_{MAX}}$ -- maximum recirculating power available, kW.

P_M -- drive motor power, kW.

η_L -- friction losses of the gear testing apparatus, expressed as a fraction of the recirculating power.

From the foregoing discussion, it is apparent that the primary advantage of the recirculating power design is that a drive motor of much lower capacity can be used to achieve the same transmitted power as in an open-loop design. Additionally, the need for a separate load on the drive motor is eliminated. Finally, as most load coupling designs are capable of producing infinitely variable torques, a wide range of transmitted powers may be developed at the gears without the need for a variable speed drive motor. The primary disadvantage of the recirculating power design is that it is more mechanically complex than the open-loop design, resulting in more effort being required to position the gears prior to testing. The recirculating power design was chosen for the gear testing apparatus constructed at the University of Alberta.

3.1.2 Examples of Gear Testing and Research Conducted with Recirculating Power Gear Testing Apparatus

The advantages of the recirculating power design outlined in Section 3.1.1 have led to its incorporation into many academic and commercial gear testing rigs. The investigations conducted with this type of apparatus encompass a wide scope of gear research and testing activities. Towle [6] describes the use of the FZG testing rig as a standard in the evaluation of wear properties of industrial lubricants. The FZG testing rig is a mechanically loaded recirculating power gear testing apparatus first proposed by Niemann at the Forschungstelle fur Zahnrader und Getriebebau in Munich, Germany. Townsend et al. [7] used a hydraulically loaded recirculating power gear testing apparatus to evaluate the effect of lubricant base stock and additive combinations on spur gear pitting life. Townsend and Akin [8] performed experimental measurements of instantaneous and average gear tooth surface temperatures as a function of gear load, gear speed and oil jet pressure. An investigation of the oil jet velocity required to provide adequate lubrication on the ingoing side of a gear mesh was examined by Akin et al. [9]. Haizuka et al. [10] studied the frictional loss and temperature rise of spur gears as a function of lubricant oil composition. Naruse [11] investigated the effect of lubricant oil composition on the limiting load for scoring. Fujita et al. [12] used a recirculating power gear testing apparatus to perform fatigue tests on induction hardened Mo-Cr gears and Townsend [13] conducted surface fatigue tests to compare the performance of hot forged

powder metal AISI 4620 and 4640 gears to AISI 4340 and 9310 steel gears. Atherton et al. [14 and 15] used a remotely controlled acoustic intensity probe to evaluate the effect of gear tooth profile, load and speed on measured noise. Finally, Labath and McCarthy [16] conducted full torque, full speed testing of a marine gear box in a modified recirculating power test rig.

3.1.3 Design Requirements

Once the range of tests to be performed and basic design of the gear testing apparatus had been established, the main design requirements were formulated. The requirements governing the design of the gear testing apparatus were as follows:

(1) A 15 kW 3-phase Robbins and Myers squirrel cage induction motor was to be used as the drive motor for the apparatus. The maximum speed of the motor is 1725 r.p.m. and it is coupled to a Canadrive 15 kW primary voltage control type controller. This controller provides infinitely adjustable speed from zero to full speed with a maximum speed fluctuation of 1%. The efficiency of the motor is a function of rated speed and rated load, as shown in Figures 3.3 and 3.4, respectively.

(2) The testing apparatus was to accommodate spur and helical gear pairs with face widths as much as 100 mm and center distances infinitely variable between 200 mm and 500 mm.

(3) The maximum shaft length was approximately 2 m. This distance would facilitate the undertaking of studies dealing with torsional vibration in gearing systems [17].

(4) The gear testing apparatus was to be designed to minimize fabrication and installation costs by ensuring it could be fabricated within the Department of Mechanical Engineering. This requirement necessitated a modular and a comparatively low mass design.

The establishment of the drive motor power and efficiency in (1) above meant that the recirculating power available to test gear sets could be specified once the system power losses could be estimated. The amount of recirculating power available would guide the design of the test gears, shafts, bearings and apparatus frame as governed by requirements (2) - (4).

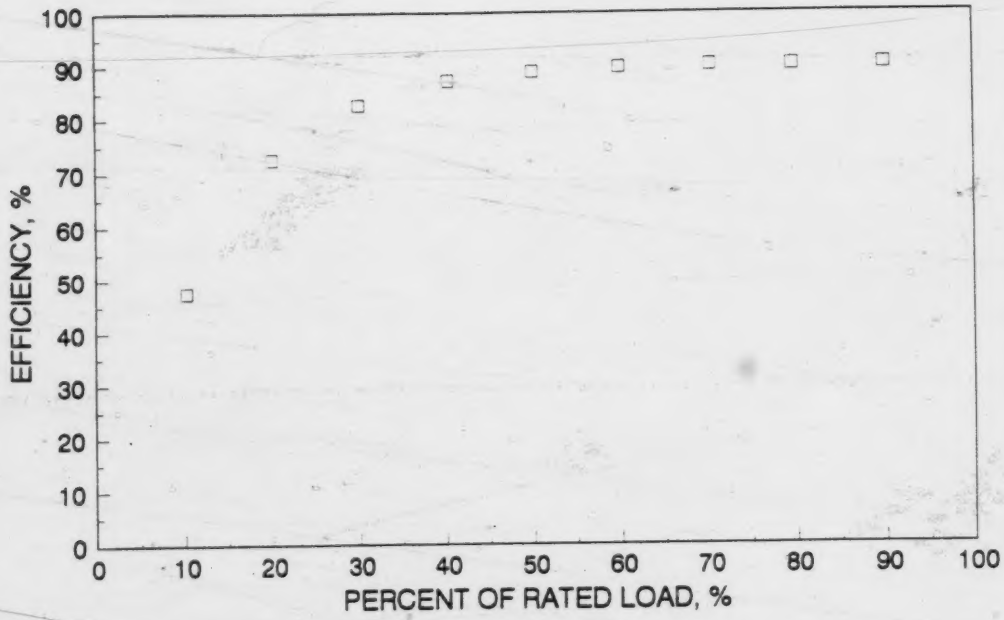

Figure 3.3 - Drive Motor Efficiency as a Function of Rated Load

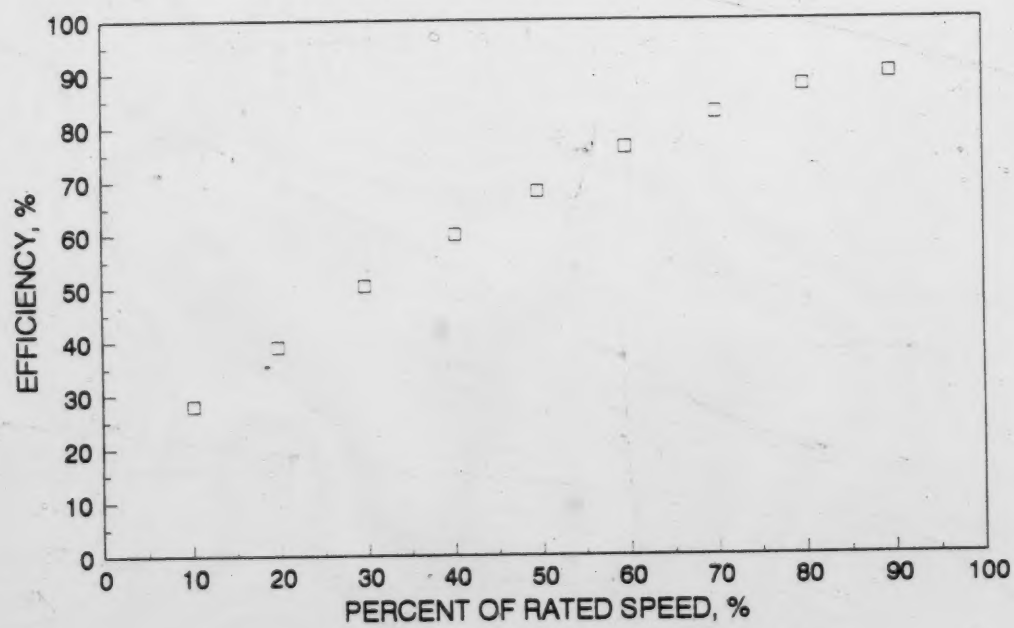

Figure 3.4 - Drive Motor Efficiency as a Function of Rated Speed

3.2 System Losses: Determination of Maximum Recirculating Power

3.2.1 Introduction

The four major power losses to a gearing system are sliding friction, rolling friction, windage and bearings losses [18]. Sliding friction losses result from the gear teeth sliding across one another during the meshing cycle. Rolling friction losses occur when an elastohydrodynamic film is formed between the gears. Windage losses result from drag on the gear body as it turns. In this section, methods will be introduced which were used to calculate the sliding and windage losses of various gear pairs. Rolling friction losses are generally small and were not considered in this thesis. Bearing losses will be discussed in Section 3.2.3.

3.2.2 Gear Power Losses

Dudley [19] provides the following expression for the determination of sliding friction losses for spur and helical gearing:

$$\eta_S = \frac{50f}{\cos\phi_{tp}}\left[\frac{H_S^2 + H_T^2}{H_S + H_T}\right]\cos^2\psi_p. \tag{3.3}$$

where η_S is the sliding friction power loss, %,

f is a coefficient of friction, and

H_S, H_T are the specific sliding velocities at the start of approach action and the end of recess action, respectively.

The coefficient of friction is dependent upon the pitch line velocity of the gear set, as shown in Figure 3.5 [19]. The specific sliding velocities at the start of approach action and end of recess action are dependent upon gear geometry and may be expressed as follows:

$$H_S = (m_G + 1)\left[\sqrt{\left(\frac{R_{T,GEAR}}{R_{P,GEAR}}\right)^2 - \cos^2\phi_{tp}} - \sin\phi_{tp}\right]. \tag{3.4}$$

$$H_T = \left(\frac{m_G + 1}{m_G}\right)\left[\sqrt{\left(\frac{R_{T,PINION}}{R_{P,PINION}}\right)^2 - \cos^2\phi_{tp}} - \sin\phi_{tp}\right]. \tag{3.5}$$

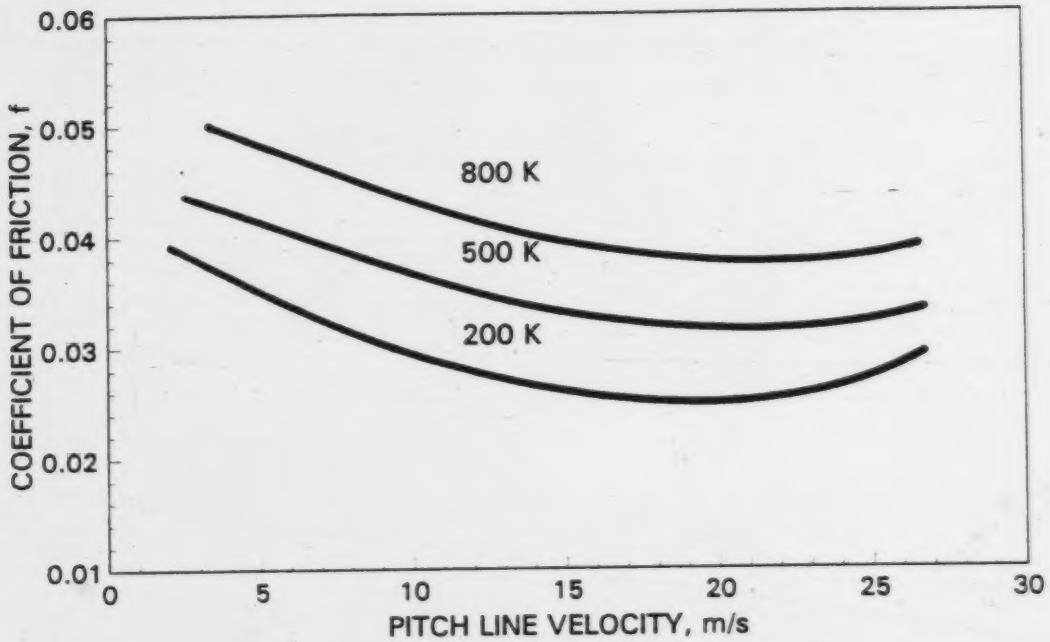

Figure 3.5 - Coefficient of Friction from Dudley [19]

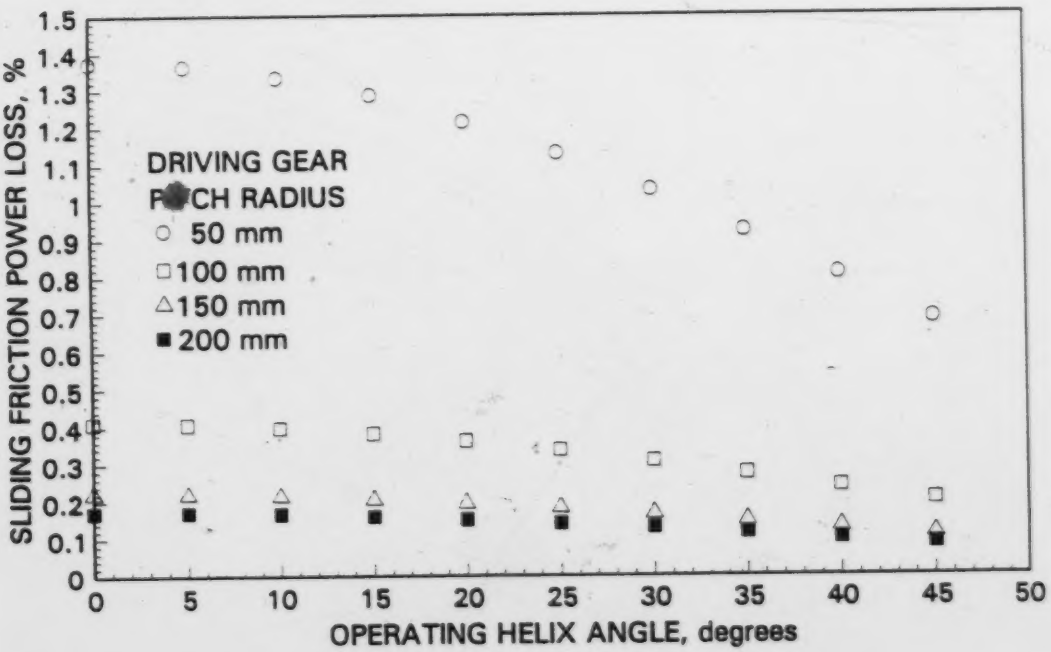

Figure 3.6 - Sliding Friction Power Losses Corresponding to the Gear Pairs Described in Table 3.1

Haizuka et al. [10] has shown that the sliding power loss of spur gears is much more involved than Equation (3.3) would indicate. They have shown that the power loss is dependent upon the gear profile, the base lubricant, lubricant additives, circumferential velocity and load. Nevertheless, Equation 3.5 is adequate for the estimation of the gear power losses for the purpose of determining the recirculating power.

The sliding losses of various gear geometries and operating conditions were evaluated. An example data set, representing four different pitch diameters, 10 helix angles and 16 operating speeds is shown in Table 3.1. The sliding power losses associated with this data set, as determined by using Equation 3.3, are shown in Figure 3.6.

The windage power loss of a gear is dependent upon the dimensions of the gear, its rotational speed and the viscosity of the gear lubricant. Anderson and Lowenthal [20] expressed the windage losses of a mating pinion and gear as follows:

$$P_{W,PINION} = C_3\left(1 + 2.3\frac{F}{R_{p,PINION}}\right)\omega_{PINION}^{2.8} R_{p,PINION}^{4.6}(0.028\mu + C_4)^{0.2} \qquad (3.6)$$

$$P_{W,GEAR} = C_3\left(1 + 2.3\frac{F}{R_{p,GEAR}}\right)\left(\frac{\omega_{PINION}}{m_G}\right)^{2.8} R_{p,GEAR}^{4.6}(0.028\mu + C_4)^{0.2} \qquad (3.7)$$

where $C_3 = 2.82\text{E-}07$ and $C_4 = 0.019$.

Equations 3.6 and 3.7 were used to evaluate the windage power losses of gear pairs formed from the data set presented in Table 3.1. The resulting windage power losses are shown in Figures 3.7 and 3.8. In Figure 3.7, the power losses are shown in terms of power, while in Figure 3.8, they are shown in terms of percentage of drive motor power using the efficiency curve of Figure 3.4. From these figures, it is apparent that the windage power losses become the major cause of gearing related power loss as pitch line velocity increases. This trend has been confirmed by recent investigations [21].

Table 3.1 - Gear Specifications for Meshing and Windage Loss Calculations

Normal Module, m_n	5 mm
Normal Pressure Angle, ϕ_{tp}	20 °
Driving Gear Pitch Radius, R_{p2}	50, 100, 150, 200 mm
Driven Gear Pitch Radius, R_{p1}	200 mm
Face Width, F	50 mm
Operating Helix Angle, ψ_p	0, 5, ... 45 °
Absolute Viscosity, μ	0.060 Ns/m^2
Driving Shaft Rotational Speed, ω_s	200, 300, ... 1700 rpm

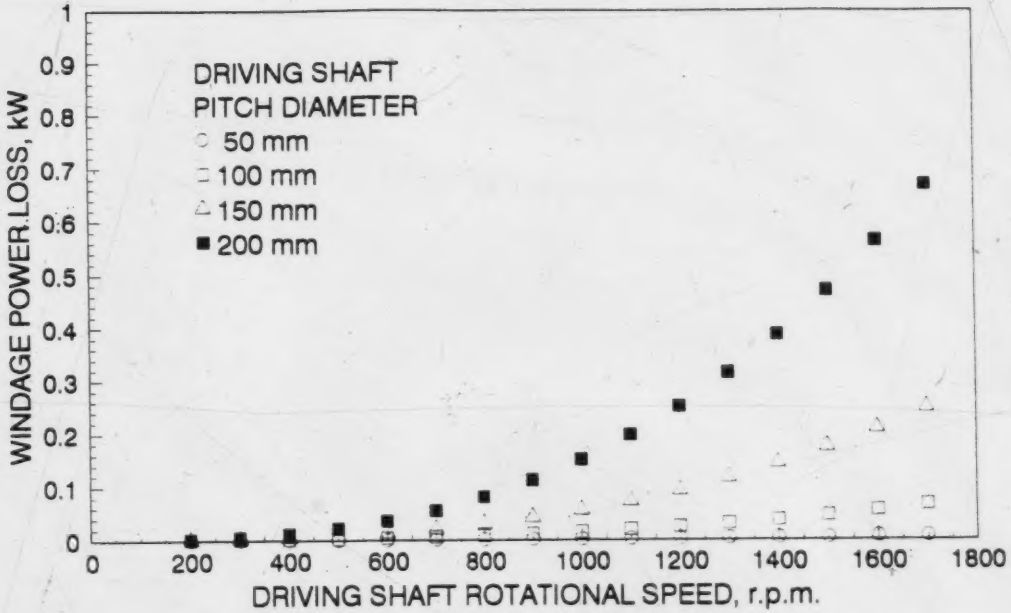

Figure 3.7 - Windage Power Losses (kW) Corresponding to the Gear Pairs Described in Table 3.1

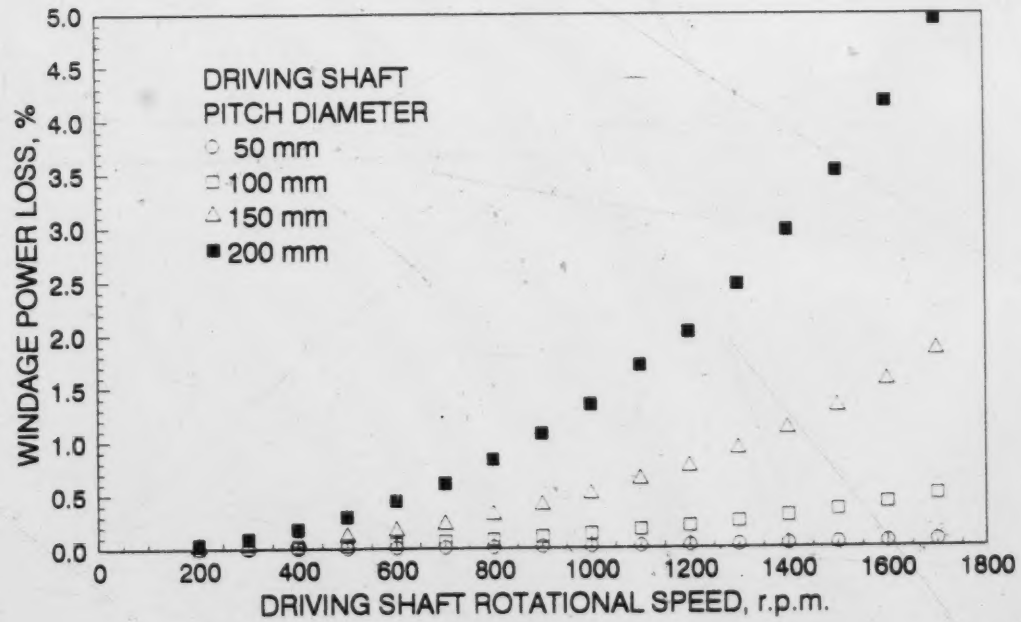

Figure 3.8 - Windage Power Losses as a Function of Drive Motor Power

3.2.3 Bearing Power Losses

The power loss associated with a roller bearing can be thought of as being composed of two parts: a power loss dependent upon the loading on the bearing and a power loss associated with viscous friction. The magnitude of the loading power loss is dependent upon the bearing geometry and the magnitude and direction of loading. The viscous friction power loss is dependent upon the kinematic viscosity of the bearing lubricant, the shaft rotational speed and the mean bearing diameter. Harris [22] expresses the bearing loss as follows:

$$P_B = k_1[f_1 F_\beta d_m + k_2 f_0(\nu_0 \omega)^{2/3} d_m^3] \tag{3.8}$$

where the first and second terms represent the loading loss and the dynamic loss, respectively, while the viscous friction loss and k_1 and k_2 are constants. Using Equation 3.8, bearing power losses were determined for various bearing types, geometries, lubricant viscosities and shaft speeds. Table 3.2 contains sample geometric and operational data for a number of ball bearings, angular contact roller bearings and spherical roller bearings. The bearing power losses associated with these bearings are presented in Figures 3.9-3.11.

3.3 Test Gear Size Determination from a Failure Study

3.3.1 Gear Failure Modes

A gear failure study was conducted in order to determine the range of sizes of gears which could be tested at various speeds. The gear failure study consisted of determining the maximum torque which could be carried by a gear pair turning at constant speed without incurring various types of failures. The maximum torque was then compared to the maximum available torque as determined using the methods discussed in Section 3.2. Although standards exist which identify many modes of gear failures [23], the exact loading condition which will result in failure by most of these modes is unknown. Three modes of failure which are understood well and quantifiable are pitting, bending fatigue and scuffing.

Pitting is a surface-fatigue failure which occurs when repeated subsurface stresses are beyond the endurance limit of the gear material. These repeated stresses will cause

Table 3.2 - Bearing Specifications for Power Loss Calculations

Mean Bearing Diameter, d_m	60 mm, 70 mm
Rolling Element Diameter, D	10 mm
Groove Radius of Curvature, r	5 mm
Number of Rows of Rolling Elements	1
Contact Angle, α	0, 10, 30, 40 °
Largest Radial Load, F_R	5000 N
Largest Axial Load, F_a	2000 N
Shaft Rotational Speed, ω_s	0, 100 ... 1500 rpm
Kinematic Viscosity, ν	25, 125 cSt

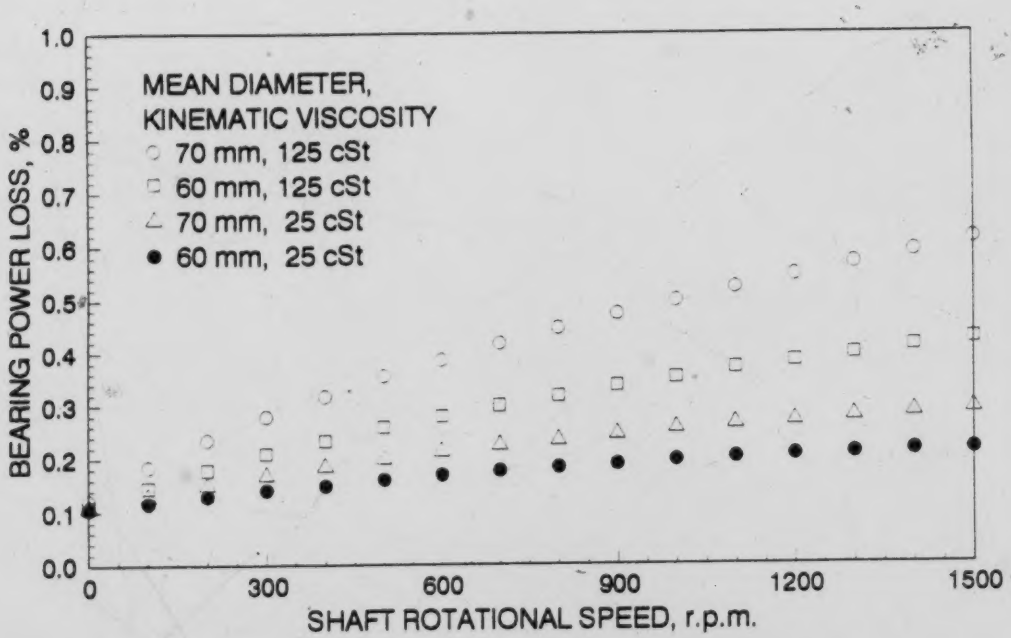

Figure 3.9 - Bearing Power Losses for the Ball Bearing Geometries Described in Table 3.2

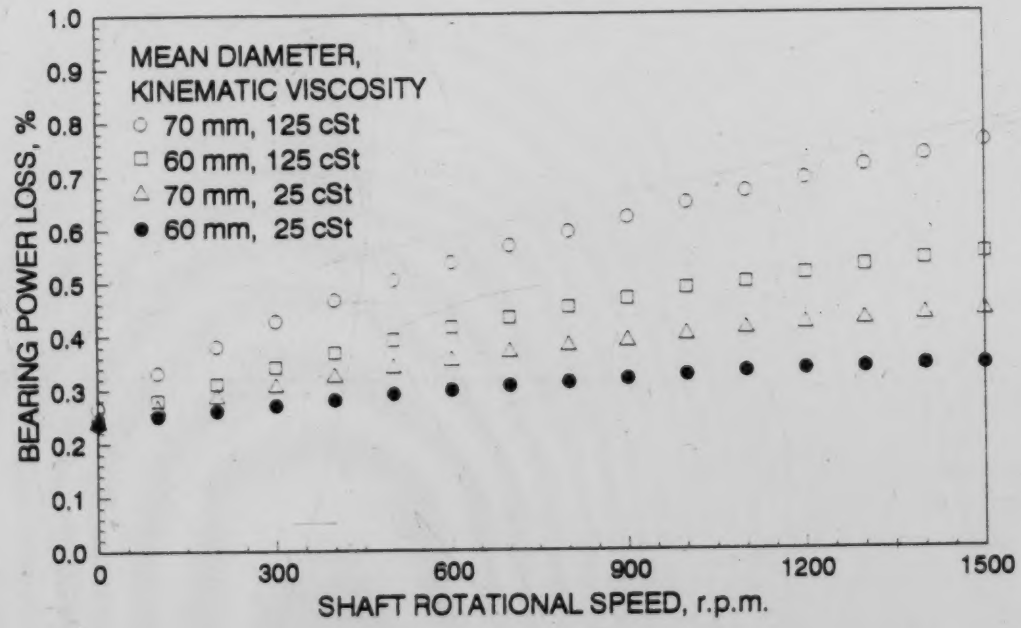

Figure 3.10 - Bearing Power Losses for the Angular Contact Ball Bearings Desribed in Table 3.2

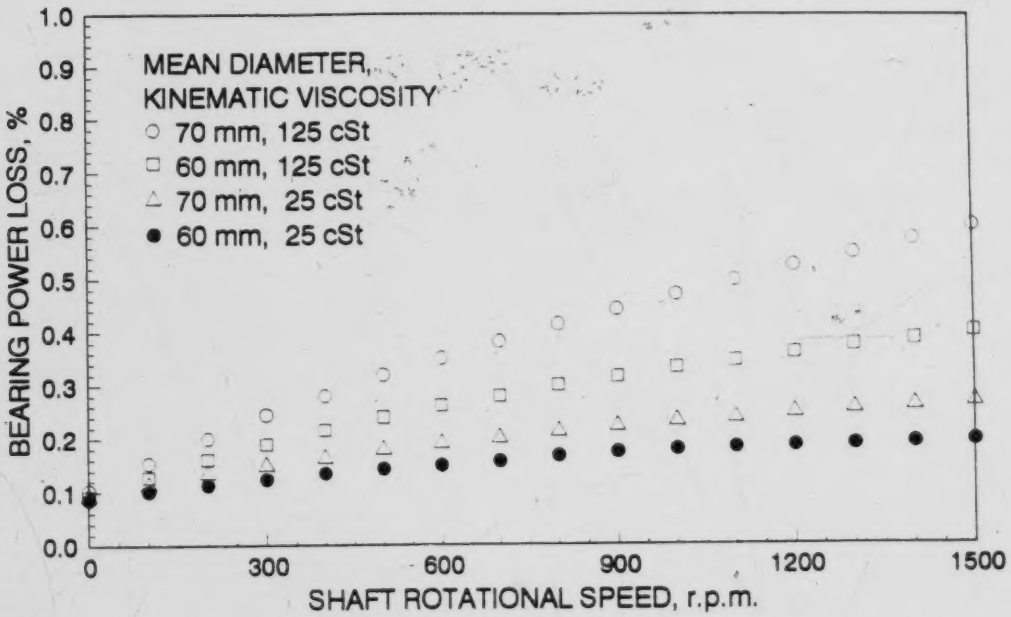

Figure 3.11 - Bearing Power Losses Corresponding to the Spherical Roller Bearing Geometries Described in Table 3.2

removal of material at the surface of the gear and the formation of cavities. Pitting is caused by excessive contact stress, which may be the result of minor profile errors, local surface irregularities, or less than full face contact. Destructive pitting will result in the destruction of the tooth profile, rough and noisy operation, and possible tooth breakage failure.

Bending fatigue failure occurs when cyclic stressing of the gear tooth takes place past the endurance limit of the gear material. A crack will result in the root region of the gear tooth and the whole tooth, or part of it, will break away. The break surface will be typical of a fatigue failure: most of the surface will be relatively smooth, with the region of brittle failure being rough and jagged. The major cause of bending fatigue failures is the loading of the gear teeth in such a manner that the root stresses of the gear exceed the endurance limit of the gear material. These fillet stresses may be augmented by the presence of stress concentrations such as notches in the root fillet, hob tears, inclusions, heat treatment cracks, grinding burns and residual stresses.

Scuffing is wear failure which is caused by a failure of the lubricant film due to localized overheating of the gear mesh, permitting metal-to-metal contact. This contact will weld and tear contacting asperities. Light and moderate scuffing are characterized by radial tear marks which appear on the gear teeth in patches on the addendum, dedendum, or both. Material is removed from above and below the operating pitch line in destructive scuffing, leaving the pitch line clearly visible. The gear tooth surface also exhibits considerable radial scratching and tearing and often material is displaced radially over the gear tip.

3.3.2 Gear Failure Study

The maximum torques which could be applied to various gear pairs without a failure occurring as a result of pitting, bending fatigue or scuffing were determined using methods described in Dudley [19]. These methods are in widespread use and their formulation will not be presented. Using these methods, the maximum allowable torque without incurring failure was determined for three groups of gear geometries. Dimensional data for these groups are shown in Table 3.3. The maximum torque which can be applied to the gears in Group 1 is shown in Figures 3.12 and 3.13. Figures 3.12

Table 3.3 - Sample Data for Gear Failure Study

Parameter	Group 1	Group 2	Group 3
Pressure Angle, ϕ°_{np}	20.0	20.0	20.0
Helix Angle, ψ°_{p}	0.0	20.0	0.0
Normal Module, m_n , mm	10.00	10.00	5.00
Cutter Addendum, a_r , mm	13.50	13.50	6.75
Cutter Tip Radius, r_{rt} , mm	3.50	3.50	1.75
Pitch Radius, R_{p2} , mm	100 - 250	100 - 250	100 - 250
Gear Ratio, m_g	1.00	1.00	1.00
Face Width, F , mm	25.00	25.00	25.00
Shaft Speed, ω_2 , r.p.m.	500, 1500	500, 1500	500, 1500
Design Life, cycles	10.0E+07	10.0E+07	10.0E+07
Gear 1 Brinell Hardness	300	300	300
Gear 2 Brinell Hardness	300	300	300
Reliability Rating	High	High	High
Mounting Rating	Full Face	Full Face	Full Face
Power Source Rating	Uniform	Uniform	Uniform
Load Rating	Uniform	Uniform	Uniform
Allow Stress Contact No.	9.00E+08	9.00E+08	9.00E+08
Allowable Stress No.	2.75E+08	2.75E+08	2.75E+08
Scor. Criterion Number	8000	8000	8000

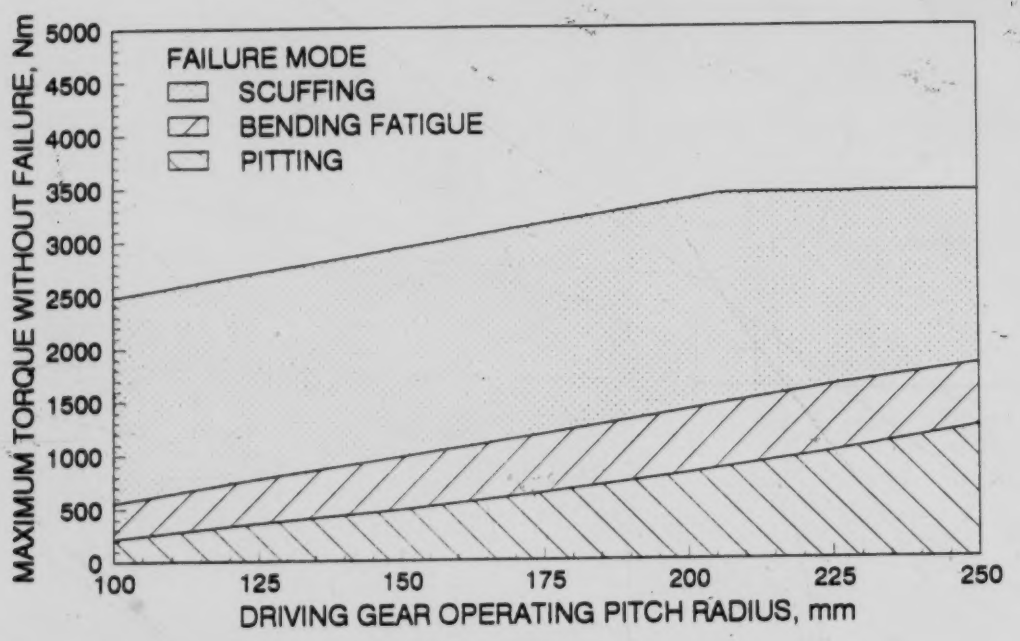

Figure 3.12 - Maximum Allowable Torques without Incurring Gear Failure: Gear Group 1, 500 r.p.m.

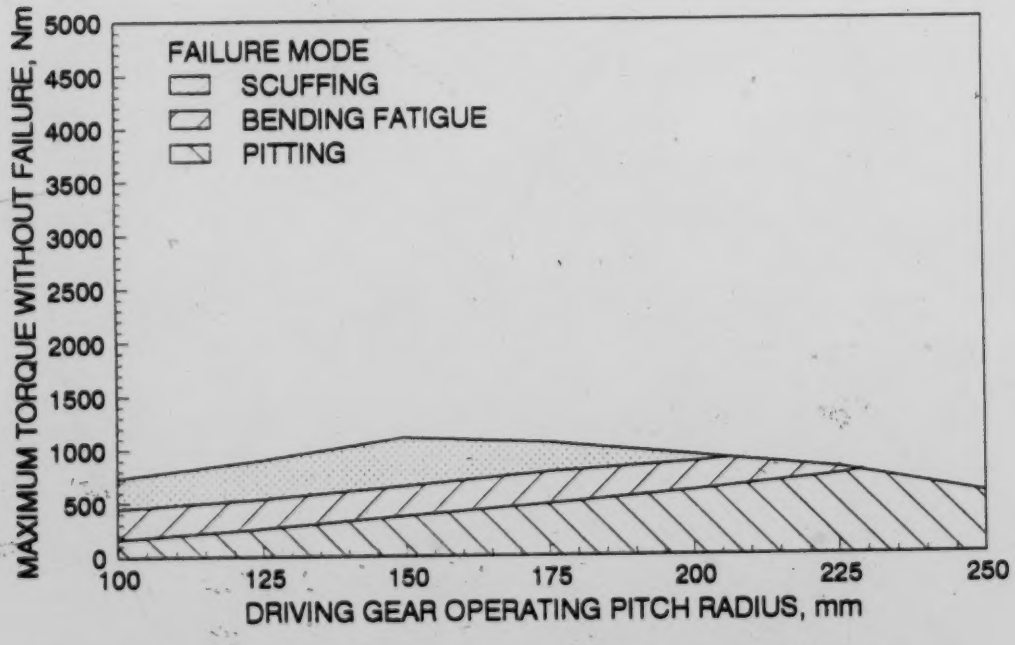

Figure 3.13 - Maximum Allowable Torques without Incurring Gear Failure: Gear Group 1, 1500 r.p.m.

and 3.13 present results for constant driving shaft rotation speeds of 500 r.p.m. and 1500 r.p.m., respectively. Similar results are shown for the other two groups of gears in Figures 3.14-3.17. In each of these figures, three shaded regions are shown. Each region and its extension down to the zero torque axis represents the operating envelope in which failure by the indicated mode will not occur. From these and other calculations, it was determined that the maximum anticipated testing torque which would be required at the beginning of a test would be 2000 Nm.

3.4 Shaft and Bearing Design

3.4.1 Shaft Design

The goal of the shaft design was to determine an appropriate size for the driving and driven shafts, as well as the number and location of bearings which would minimize gear deflection and misalignment while remaining consistent with the design requirements of Section 3.1.3. In order to speed the design of the shafts and support frame, finite element analysis was used. A finite element code was written which permitted the static analysis of linear structures composed of Euler or Timoshenko beam or shaft elements. The shaft elements are two-dimensional, six-degrees of freedom, non-isoparametric elements. The accuracy of the code was checked against a number of geometries and loading conditions with analytic solutions. One such geometry is the cantilevered shaft shown in Figure 3.18. For this example, the deflections, slopes and rotations at the nodes of 10 equally spaced elements are compared to the exact solution in Table 3.4. The maximum difference between the numerical and exact solution at any node is 0.25%.

Using this code, the bearing load and shaft deformation and rotation were evaluated for various combinations of shaft sizes and number and location of bearings. One of the later models for the driving and driven shafts is shown in Figure 3.19. This figure shows the driving shaft supported at four locations, denoted by bearing numbers 1-4. The driven shaft is supported on bearings 5-10. Bearings 7 and 8 are located on either side of the load coupling. One of the objectives of the shaft design was to determine the best position of bearings 7 and 8 or whether they were required at all. Bearings 1-3 and 6-10 are loaded radially while bearings 4 and 5 are loaded radially and axially. Shaft element sizes and the known external loads and maximum gear weights are

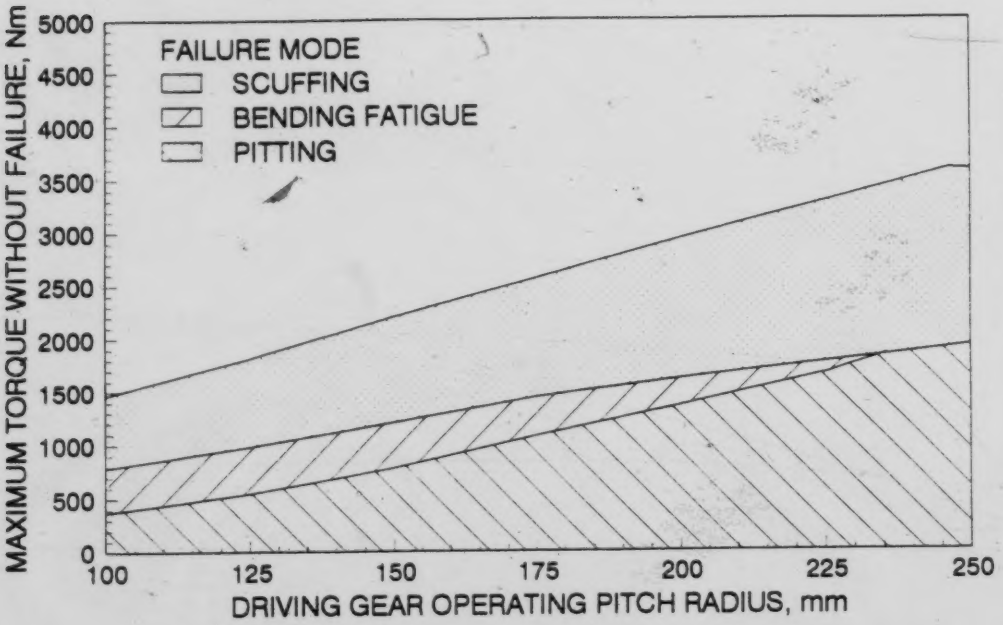

Figure 3.14 - Maximum Allowable Torques without Incurring Gear Failure: Gear Group 2, 500 r.p.m.

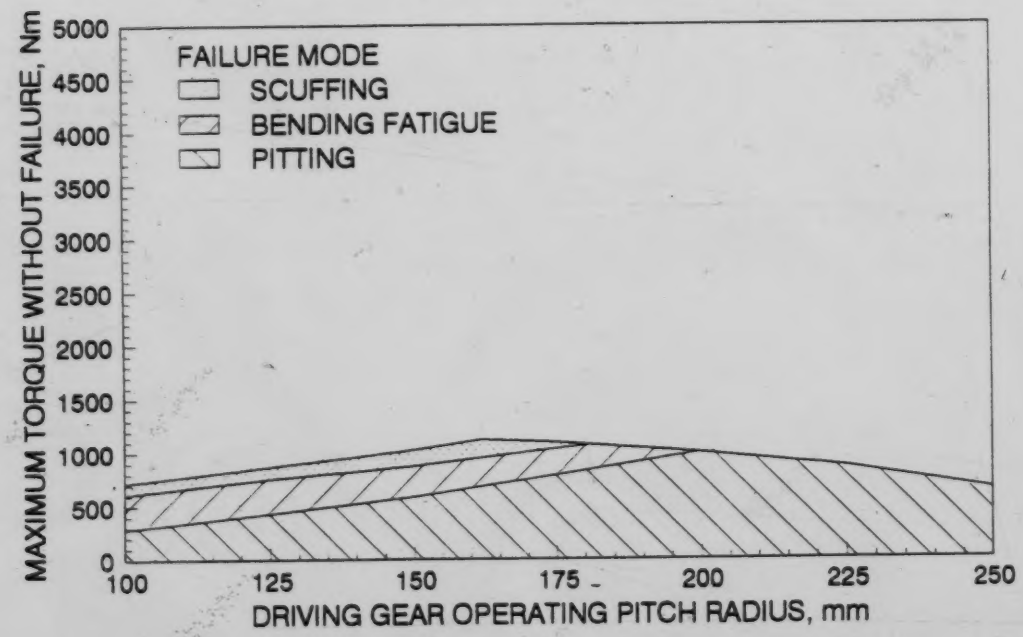

Figure 3.15 - Maximum Allowable Torques without Incurring Gear Failure: Gear Group 2, 1500 r.p.m.

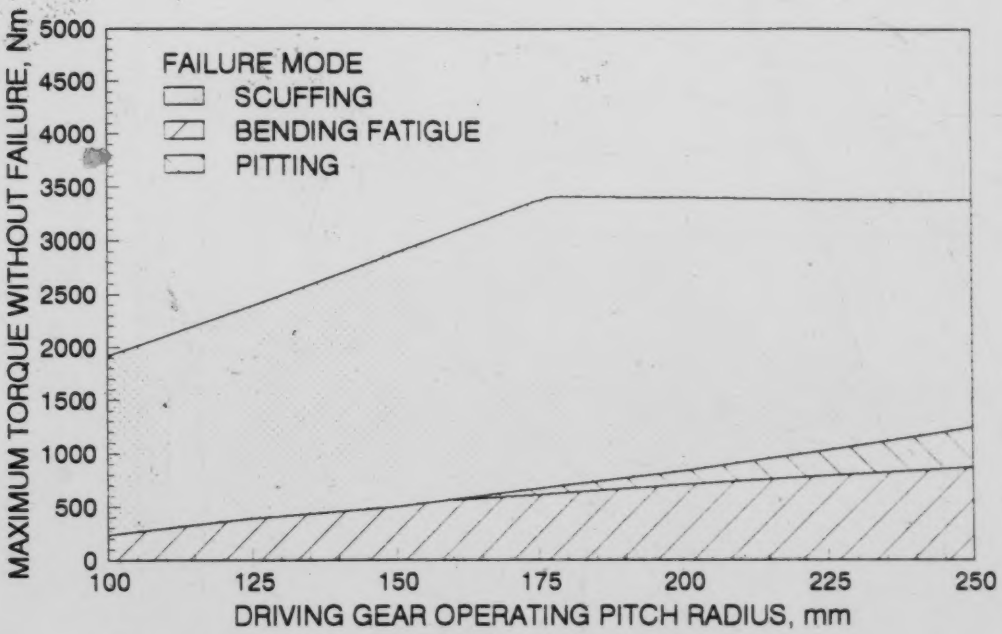

Figure 3.16 - Maximum Allowable Torques without Incurring Gear Failure: Gear Group 3, 500 r.p.m.

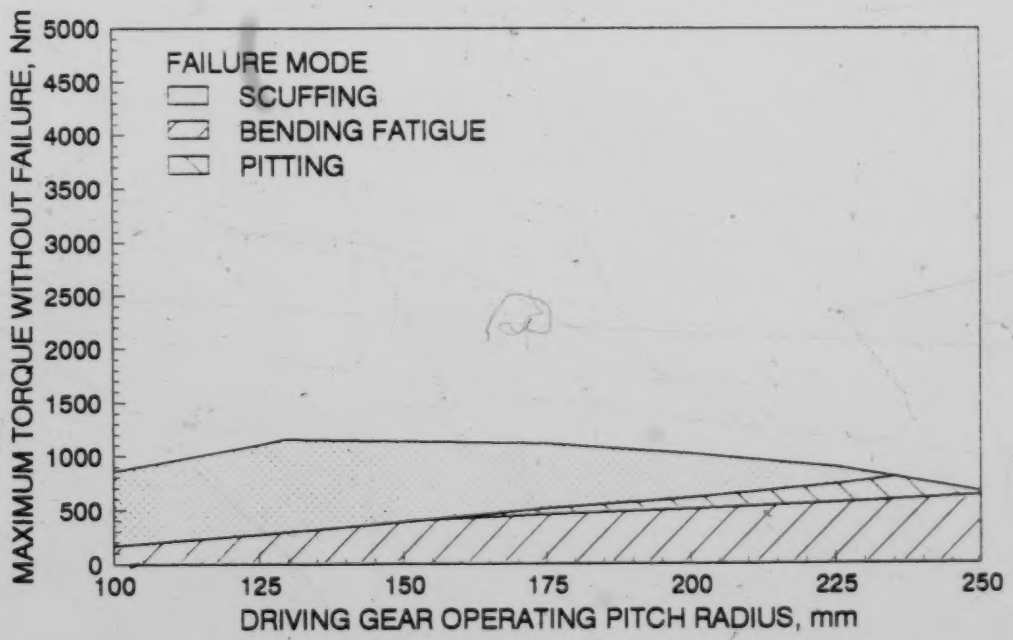

Figure 3.17 - Maximum Allowable Torques without Incurring Gear Failure: Gear Group 3, 1500 r.p.m.

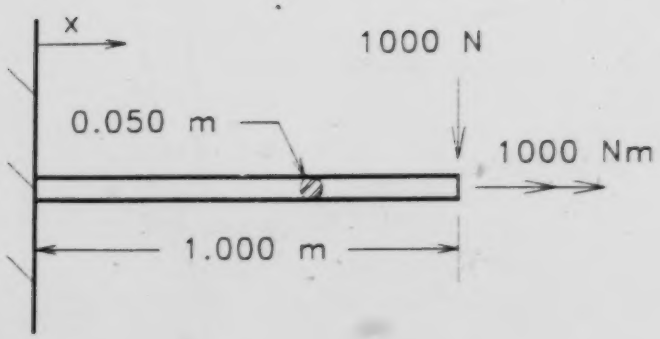

Figure 3.18 - Finite Element Code Test Model

Table 3.4 - Comparison of 10 Element Finite Element Model to the Exact Solution for a Cantilevered Shaft

	Deflection (mm)		Slope (degrees)		Rotation (degrees)	
Distance x (mm)	10 Elements	Exact Solution	10 Elements	Exact Solution	10 Elements	Exact Solution
100	0.0761	0.0753	-0.085	-0.085	-0.118	-0.118
200	0.2926	0.2909	-0.161	-0.161	-0.236	-0.236
300	0.6338	0.6311	-0.228	-0.227	-0.355	-0.353
400	1.0842	1.0804	-0.286	-0.285	-0.473	-0.471
500	1.6282	1.6231	-0.335	-0.335	-0.591	-0.589
600	2.2502	2.2438	-0.375	-0.375	-0.709	-0.707
700	2.9345	2.9268	-0.407	-0.407	-0.826	-0.825
800	3.6657	3.6566	-0.429	-0.429	-0.946	-0.942
900	4.4280	4.4175	-0.442	-0.442	-1.064	-1.060
1000	5.2059	5.1940	-0.447	-0.446	-1.182	-1.178

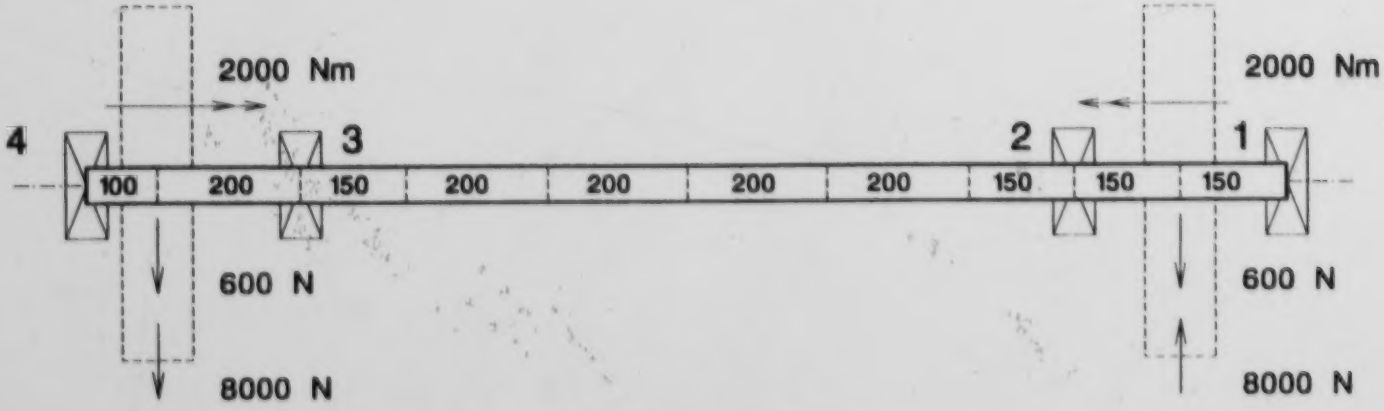

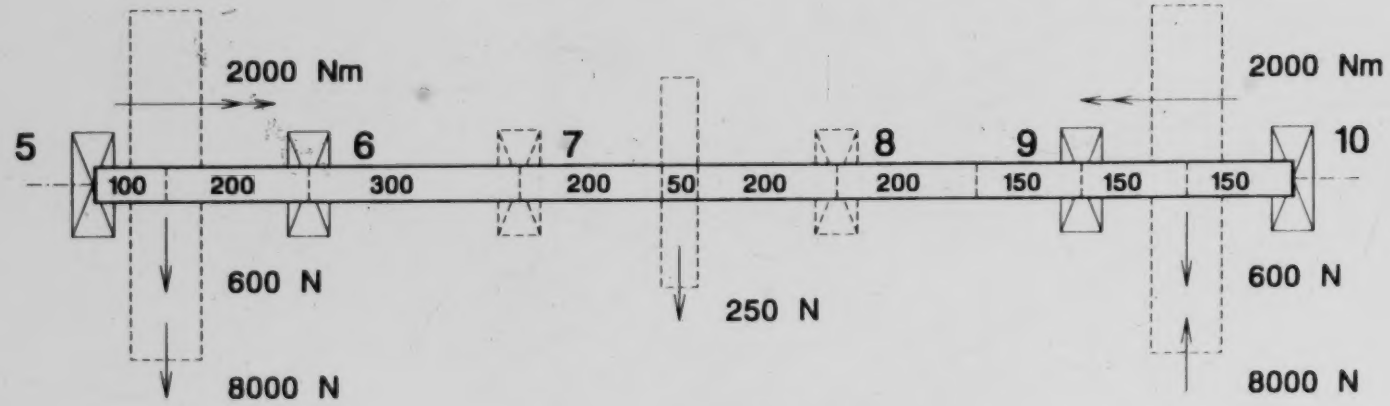

Figure 3.19 - Driving and Driven Shaft Finite Element Models

shown in Figure 3.19. For each shaft size, the shaft weight was calculated and added to the model as nodal forces. Element position is referenced to the x-axis shown on both models. For the bearing arrangement shown, the rotations and slopes were evaluated for shaft diameters of 35-60 mm and driven shafting arrangements including and omitting bearings 7 and 8.

Figures 3.20 and 3.21 show deflections and slopes along the driving shaft model for shaft diameters of 40 mm and 50 mm. The deflections of the driven shaft model including and omitting bearings 7 and 8 are shown in Figures 3.22 and 3.23. The slope along the model for the same conditions are shown in Figures 3.24 and 3.25.

The fatigue life of the shaft was determined for each condition using the Soderberg relation [24]:

$$d(mm) = \{10.185\ n[(\frac{T_{MAX}}{\sigma_y})^2 + (\frac{M_{MAX}}{\sigma_{se}})^2]^{1/2}\}^{1/3}. \qquad (3.9)$$

The maximum torque applied to the gears is known and the maximum bending moment on the shaft was determined from the finite element analysis. Factors of safety for 35, 40, 45, 50, 55 and 60 mm shafts were determined to be 0.996, 1.487, 2.118, 2.905, 3.867 and 5.120, respectively.

As a result of the finite element analysis, it was determined that the driving and driven shafts would be 50 mm in diameter. Also, it was determined that bearings 7 and 8 would be required and that the final bearing arrangement would be based on Figure 3.19. Lastly, it was determined that the shaft designed complied with the appropriate standard, AGMA 260.02 [25].

3.4.2 Bearing Selection

Shaft deflections, bearing position and radial loads were determined from the finite element analysis. Determination of suitable bearings for each location involves investigation of various design parameters:

1. Available space,
2. Bearing life,
3. Static and dynamic load rating,
4. Maximum angular misalignment and tolerances,

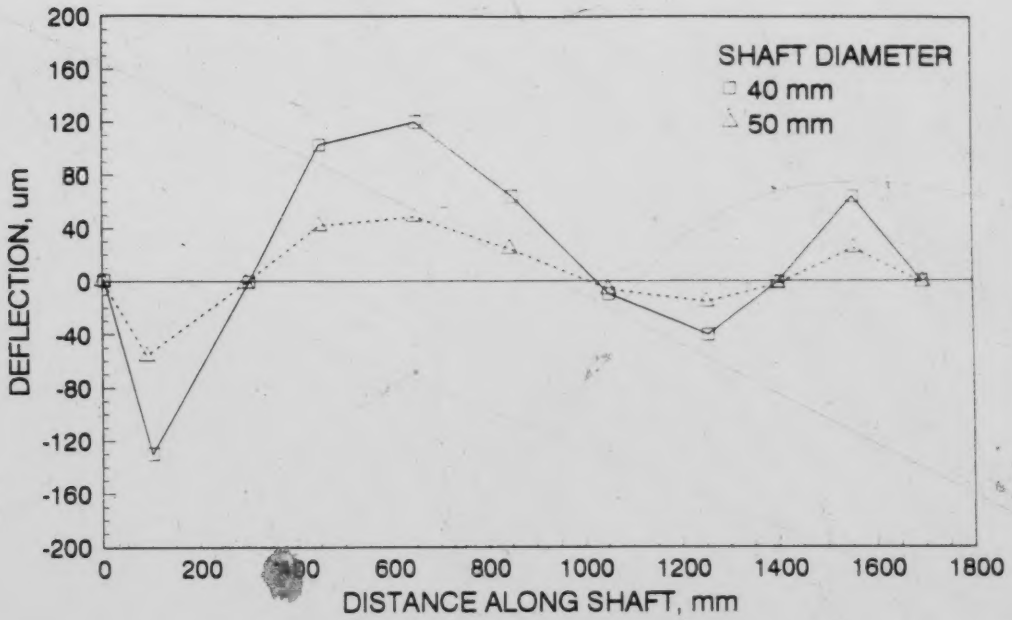

Figure 3.20 - Deflections of the Driving Shaft Finite Element Model

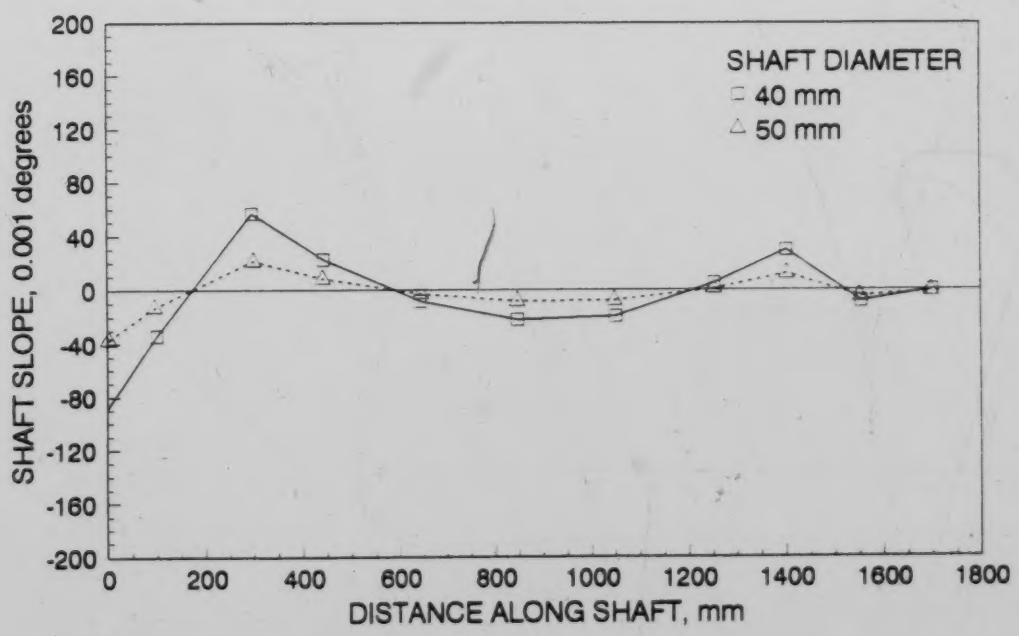

Figure 3.21 - Slopes of the Driving Shaft Finite Element Model

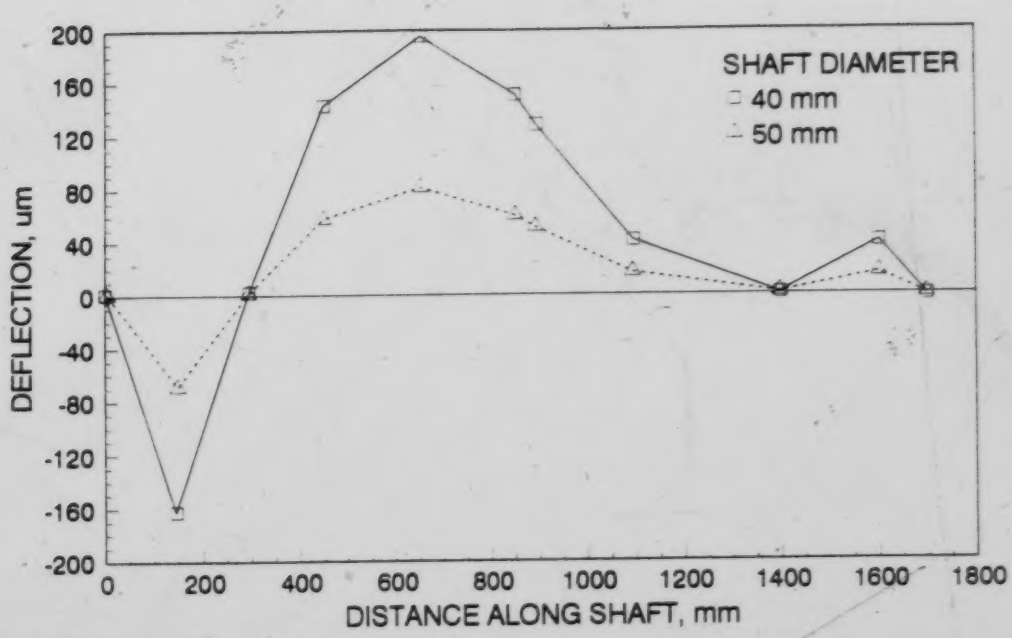

Figure 3.22 - Deflections of the Driven Shaft Finite Element Model: Bearings 7 and 8 Omitted

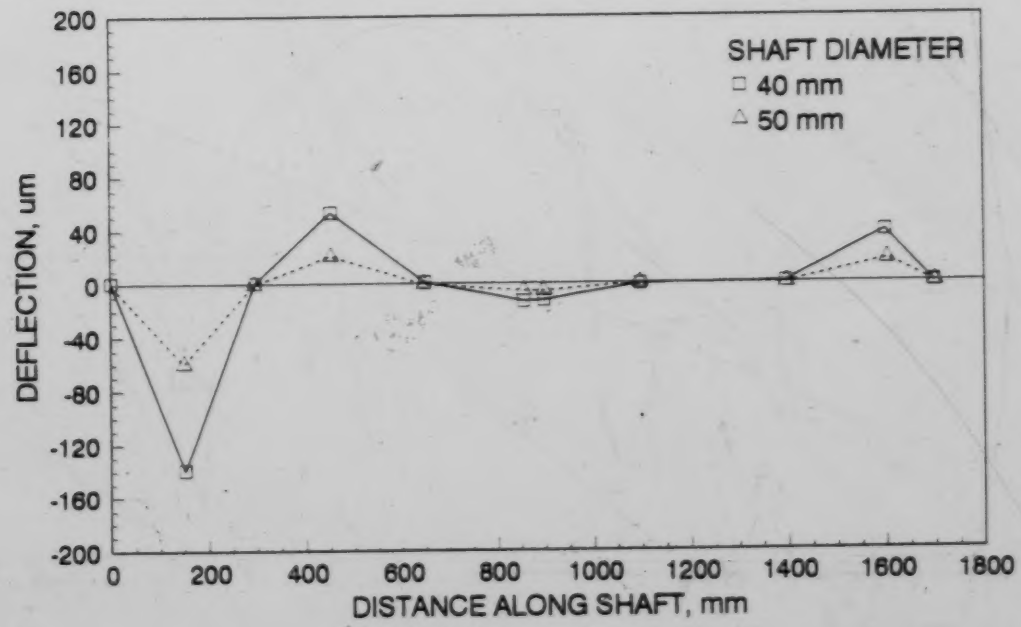

Figure 3.23 - Deflections of the Driven Shaft Finite Element Model: Bearings 7 and 8 Included

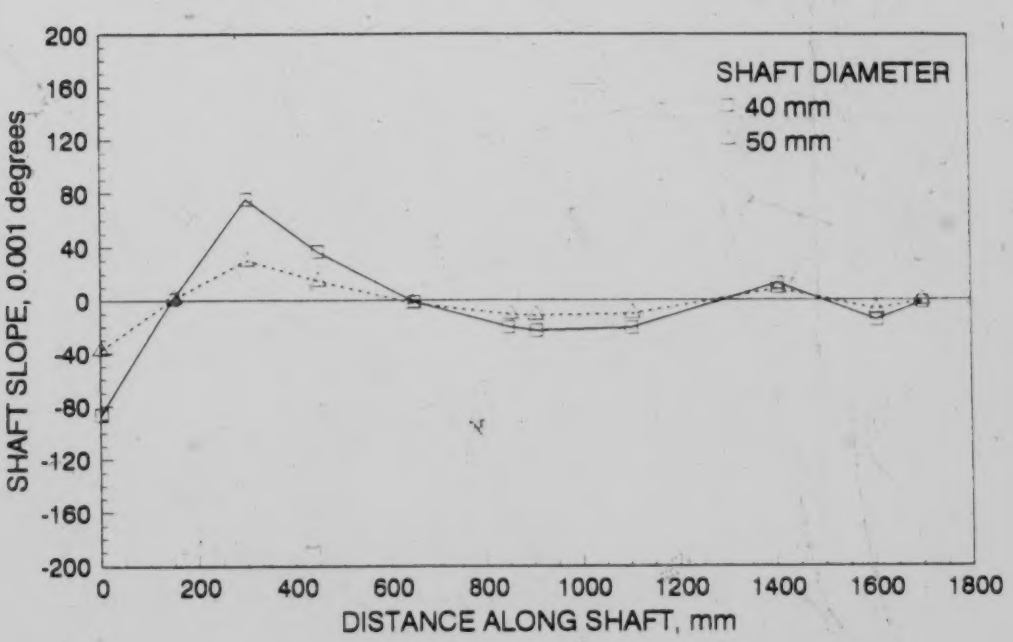

Figure 3.24 - Slopes of the Driven Shaft Finite Element Model: Bearings 7 and 8 Omitted

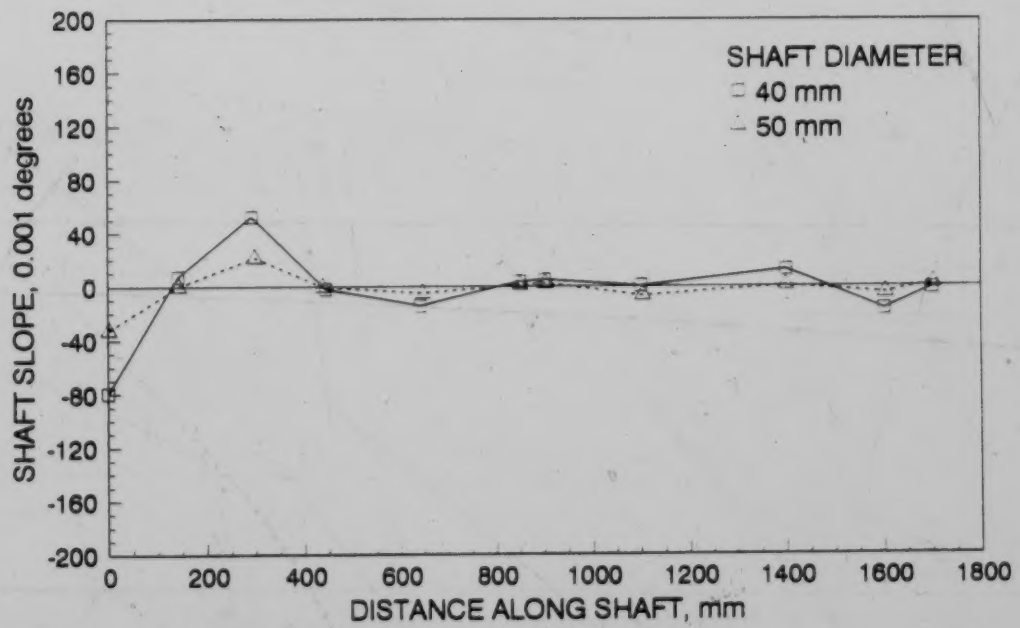

Figure 3.25 - Slopes of the Driven Shaft Finite Element Model: Bearings 7 and 8 Included

5. Maximum speed for grease and oil lubrication, and
6. Mounting and Dismounting procedures.

Twenty-one bearings were examined in terms of these parameters. Details of these calculations will not be presented here, but can be found in any manufacturer's handbook [26] or bearing design textbook [27]. Spherical roller bearings were chosen for the radically loaded bearings and angular contact ball bearings were chosen for the radially and axially loaded bearings. The spherical roller bearings were mounted on tapered sleeves and installed in manufacturers' pillow blocks. Custom housings were machined for the angular contact ball bearings.

3.4.3 Bearing Lubrication

The determination of the bearing lubricant involved the selection of the lubrication method, the correct lubricant viscosity and the relubrication interval and amount. Four common methods of bearing lubrication include grease lubrication, oil bath lubrication, recirculating oil lubrication and oil mist lubrication [27, 28]. The recommended method is strongly dependent upon the bearing operating speed. For this application, grease lubrication is the best choice. The kinematic viscosity range required for the grease is 35-85 cSt at 40 degrees Celsius, with a relubrication rate of 12.5 g every 1500 hours [29, 30]. Parameters important to the selection of a grease include grease consistency, operating temperature range, rust inhibiting properties and load carrying ability. For temperatures exceeding 120 degrees Celsius, lithium 12-hydroxy greases are most commonly used for bearing lubrication [32]. The grease selected was a light greyish yellow LGMT3 mineral oil based lithium grease with a dropping point of 190 degrees Celsius and a kinematic viscosity of 120 cSt at 40 degrees Celsius.

3.5 Gear Lubrication System Design and Gear Lubricant Specifications

3.5.1 Lubrication System Design

The design of a gear lubrication system is a function of gear type, pitch-line velocity, surface finish, gear hardness, transmitted load and lubricant viscosity [19, 33]. The design objectives for the lubrication system are three-fold:

1. To provide an oil film thickness between the meshing tooth surfaces such that premature degradation of the tooth profile does not occur as a result of scoring or from other heat or lubricant related gear failures.
2. To minimize the lubricant power loss occurring at the gears. While this objective is important for any gear pair, it is especially important for gear pairs in a recirculating power testing apparatus.
3. To ensure that the maximum amount of heat is removed from the gears and that oil temperature is maintained within reasonable limits.

The major methods of gear lubrication are identical to the methods of bearing lubrication described in Section 3.4: grease, oil bath, oil jet (force-fed) and oil mist lubrication. The method chosen to lubricate the gears was a force-fed oil system. This method was chosen for the following reasons:

1. The use of greases and other solid lubricants is limited to heavily loaded, slowly turning gear pairs.
2. The use of splash or dip lubrication is limited by the pitch line velocity of the gear pair. Once this maximum velocity is exceeded, centrifugal forces prevent the lubricant from covering an adequate portion of the gear profile. Dudley [19] gives the maximum allowable pitch line velocity for splash or dip lubrication as, approximately, 12.5 m/s. The maximum pitch line velocity anticipated with the gear testing apparatus is 50 m/s.
3. An oil mist gear lubrication system is generally used for operations where the pitch-line velocity is consistently above 80 m/s and where concern exists about excessive lubricant buildup on the gears.

The final specifications of the gear lubrication system will now be discussed. Oil is stored in the master and test gear reservoirs which have a capacity of 10 L each. Each reservoir extends across the full width of the gear testing apparatus and occupies the full width between the gear support bearings to maximize the oil surface area in order to promote cooling. Oil is pumped from the bottom of the reservoirs by a bronze gear pump with a capacity of 16.5 L/min. at 600 r.p.m. The pump is pulley driven by a 0.75 kW electric motor. Oil leaving the gear pump is directed to the valve stand and the filtration tank. On entering the filtration tank, oil passes through a series of metal screens

and cloth filters. The metal screens vary in size from 5 μm. to 1000 μm. Oil is pumped from the filtration tank to the gear pump.

Oil entering the valve stand is directed to the test gear pairs and master gear pairs at a variable flow rate between zero and 8.25 L/min. The minimum required lubricant flow for proper gear lubrication has been estimated by Dudley [33] as 1.5 L/min./100 kW and more recently by Errichello [34] as 2.5 L/min./100 kW. Using either estimate, adequate lubrication can be maintained to the gear pairs. The position of the discharge nozzles are varied as the center distance of the gear pairs change to ensure that oil is introduced directly into the engaging side of the gear mesh. Differences in lubricant flow rate to the master and test gears are compensated for by an overflow line which equalizes the oil quantity in each reservoir.

3.5.2 Lubricant Specification

The lubricant specified for use with the recirculating power gear testing apparatus must satisfy the design requirements of the lubrication system and provide the following [35]:

- protection of the gears from rust and other corrosion,
- cushioning against vibration and shock losses,
- separation of oil from water and air,
- cleaning of the system from contaminants,
- inertness towards all non-metallic parts of the testing apparatus, including its operators,
- retention of physical and chemical properties over time.

In order to meet these requirements, several properties of a lubricant must be considered, including its viscosity, oiliness, oxidation stability, detergent qualities, film strength, foam inhibition, corrosion protection, and metal deactivation and suppression [36 and 37].

Viscosity is the foundation on which most of the key lubricant properties are built [35]. The correct lubricant viscosity ensures that the oil film thickness will be sufficient to prevent contact of the mating surfaces. In general, the viscosity grade of the lubricant is increased with increasing load and decreased with increasing speed. In order to ensure that the viscosity of the lubricant remains as stable as possible over a wide

temperature range, viscosity index improvers are added to the base lubricant. The method presented by Errichello [34] was used to approximate the range of viscosities which would be required for use in the recirculating power gear testing rig. For pitch-line velocities between 5 m/s and 50 m/s, lubricants with viscosities from 223 cSt at 40 degrees Celsius to 70 cSt at 40 degrees Celsius would be required.

Oiliness, also known as lubricity, is defined as the difference in friction noticed when comparing different lubricants which can not be accounted for solely on the basis of lubricant viscosity. Oiliness is caused as a result of the ends of polar molecules adhering to a metal surface and resisting removal by shear. The oiliness of a lubricant is increased with the addition of chemicals such as fatty acids, metallic soaps and organic compounds containing chlorine, nitrogen, phosphorous or sulphur.

Oxidation of a gear lubricant can result in an increase in viscosity, darkening of color, and formation of sludge. Antioxidants fall into one of three classes: inhibitors, peroxide decomposers, and retardants. Inhibitors compete with hydrocarbons in the oil for oxygen and prevent the breakdown of the oil. Peroxide decomposers destroy compounds which might attack oil molecules further. Retardants are compounds which upon oxidation are converted to inhibitors. Compounds which are used commonly as antioxidants include anines, napthoes, disulphides and compounds of phosphorous, antinony, and selenium.

Detergent is a term used to describe two classes of chemicals whose purpose is to prevent the buildup of deposits on the gears. Detergent additives are designed to keep surfaces clean and to prevent deposit formations. Dispersant additives act to keep potential sludge forming insolubles in suspension to prevent them from depositing on metal parts.

Along the pitch-line between heavily loaded spur and helical gears, it is possible to achieve film stresses in the order of 500-700 MPa, as well as high flash temperatures. If common lubricants were used under such conditions, film breakdown would result, leading to asperity welding and scuffing. In order to prevent this from occurring, extreme-pressure additives are added to the base lubricant which chemically combine with the metal surfaces being forced together. While many different compounds are used for extreme-pressure additives [38], the most widely used extreme-pressure additives are

compounds of phosphorous and sulphur.

The rapid movement of the gears causes air to be drawn into the lubricant which causes a tight foam to develop. While the lubrication system is designed to minimize the amount of air being drawn into the oil, foam inhibitors and depressants are required to eliminate the production of foam. Foam inhibitors and depressants operate by coalescing smaller bubbles below the surface, rupturing individual bubbles at the surface and destroying the inherent stability of the liquid film. The most widely used antifoam agents are silicon fluids.

Corrosion inhibitors are polar, surface active components which coat the gear's surface with a water repellent film. Materials commonly used as corrosion inhibitors include barium, calcium and sodium sulfanates.

Certain metals when acted upon by the products of oxidation of mineral oils, can go into solution in the oils as soaps. These metal compounds can act as catalysts and accelerate the decomposition of the oil. The surfaces of the gear teeth can become etched and pitted if contact is prolonged. Metal deactivators form inactive compounds on the metal surface to prevent these reactions.

Many different types of lubricants will be required for the full range of operating conditions of the recirculation power gear test apparatus. The initial lubricant chosen was selected for the experimental stress investigation of moderately loaded spur and helical gears conducted as part of this thesis work. The lubricant chosen was an AGMA Grade 2 [39], ISO viscosity class 100, multi-service sulphur-phosphorous type gear oil. The kinematic viscosity of the lubricant is 115 cSt at 40 degrees Celsius; its viscosity index is 145; and it is rated for API GLS service. Additional compounds included are anti-scuffing agents, corrosion inhibitors, antioxidant detergents and foam inhibitors.

3.6 Final Design

The remaining mechanical design work for the gear teeth apparatus involved the design of supporting plates for the bearing pillow blocks and design of the frame using the finite element code in Section 3.4. The final specifications of the testing apparatus are shown in Table 3.5 and an overall view of the apparatus is shown in Plate 3.1.

Table 3.5 - Specifications of the Recirculating Power Gear Testing Apparatus

Overall Size	3.5 m x 1.5 m x 1.0 m
Drive Motor	15 kW at 1725 r.p.m.
Speed Control	0 - 100% of full speed
Recirculating Power	90 kW - 150 kW
Center Distance Range	200 mm - 500 mm
Maximum Face Width	100 mm
Maximum Gear Torque	2000 Nm

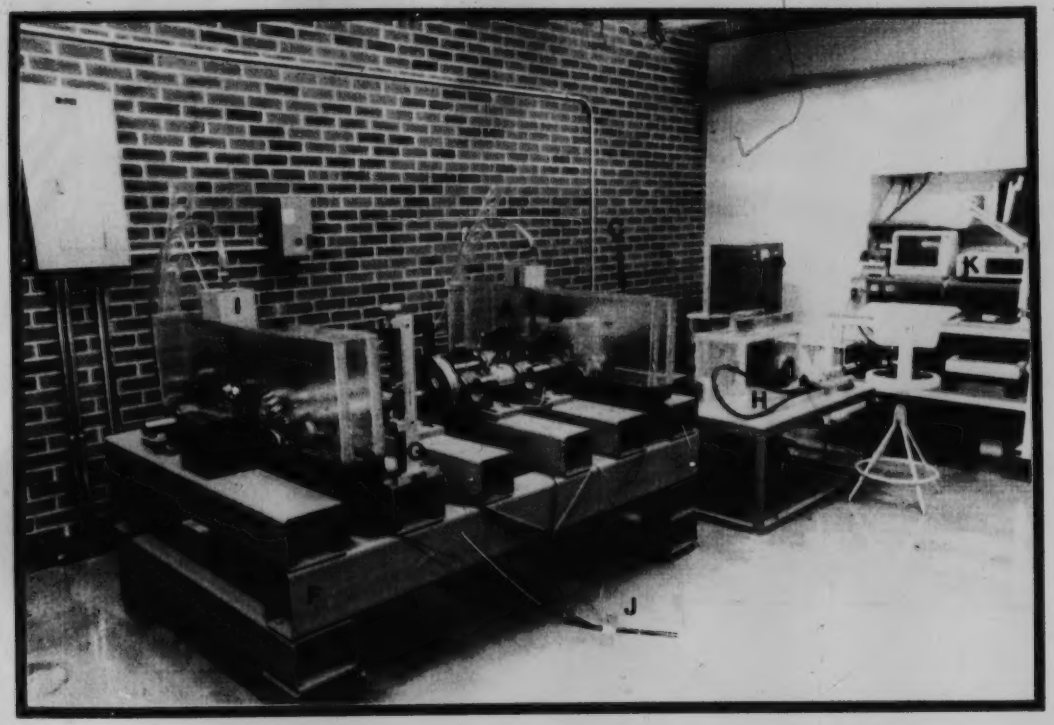

MAJOR COMPONENTS:

A - DRIVING SHAFT AND GEARS
B - DRIVEN SHAFT AND GEARS
C - DRIVE MOTOR
D - SPEED CONTROL
E - LOAD COUPLING
F - FRAME
G - STATIC POSITIONER
H - LUBRICANT PUMP MOTOR
I - LUBRICANT ENTRY POINTS
J - TRANSDUCER LEADS
K - MEASUREMENT EQUIPMENT

Plate 3.1 - Recirculating Power Gear Testing Apparatus

Chapter 4: Instrumentation

4.1 Transducers

As discussed in Chapter 3, the gear testing apparatus was designed to conduct gear research in several areas. During construction of the apparatus, transducers were installed which would meet the needs of the current study as well as possible future studies. The types of transducers installed on the test rig are shown schematically in Figure 4.1, while the position and appearance of the transducers are shown in Plate 4.1. The purpose of each of the transducers is described below.

The rotational speed of the driving shaft is monitored with an infra-red emitter detector pair indicated by "A" in Figure 4.1 and Plate 4.1. The sensor is triggered by a 20 band black and white removable strip (The strip is not shown in Plate 4.1.). Signals from the infra-red emitter detector pair are sent directly to a microcomputer be discussed further in Section 4.2.

J-type thermocouples "B" are used to monitor the outer race temperature of the spherical roller and angular contact ball bearings. The thermocouples are installed in cavities which were machined into the bearing housings. The thermocouple heads are in direct contact with the bearings' outer races, and are also immersed in, approximately, 10 ml of bearing grease in order to ensure good thermal contact to the outer race. Output from the ten thermocouples is amplified, and then multiplexed onto one analog input channel of the microcomputer data acquisition board. Bearing temperatures are monitored during any future unattended operation of the test rig in order to ensure operational safety. Ten additional thermocouples are available for monitoring drive motor bearing temperature or gear lubricant temperature during future lubricant and wear tests.

During periods of unattended operation, it is important to know that proper lubricant flow is being maintained to the gears. If lubricant line breakage, gear pump stalling, pump motor failure, or some other condition should develop which would stop the flow of lubricant to the gears, it is important that current operating status be logged, and the test rig be stopped. In order to ensure that the presence or absence of lubricant flow to the gears is known at all times, a low cost flow sensor was developed. These sensors "C" are installed directly above the gear meshes as shown in Plate 4.1. The

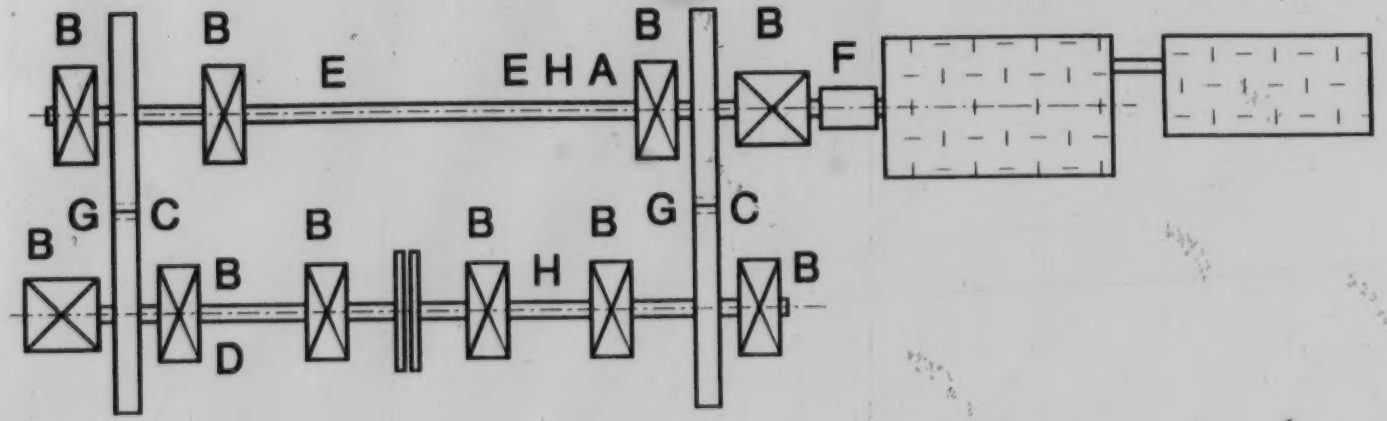

TRANSDUCER DESCRIPTION:

A - INFRA-RED EMITTER DETECTOR PAIR (SHAFT SPEED)
B - J TYPE THERMOCOUPLES (BEARING TEMPERATURE)
C - FLOW SENSORS
D - HALL EFFECT TRANSDUCER (EVENT TRIGGERING)
E - 4 ARM STRAIN GAGE BRIDGES (GEAR TORQUE MEASUREMENT)
F - 4 ARM STRAIN GAGE BRIDGES (MOTOR TORQUE MEASUREMENT)
G - 1 OR 2 ARM STRAIN GAGE BRIDGES (GEAR FILLET STRAIN)
H - COMPLETION BRIDGES AND FM/FM TRANSMITTER (DATA TRANSMISSION)

Figure 4.1 - Schematic of Transducer Locations

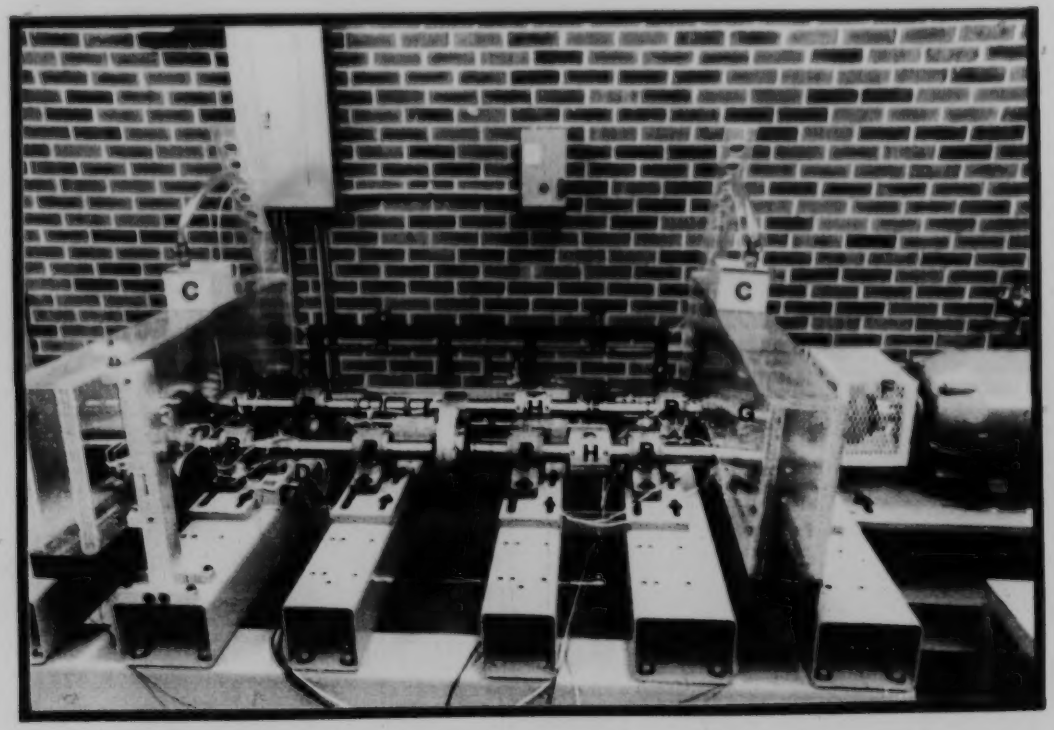

TRANSDUCER DESCRIPTION:

A - INFRA RED EMITTER DETECTOR (SHAFT SPEED MEASUREMENT)
B - J TYPE THERMOCOUPLES (BEARING TEMPERATURE)
C - FLOW SENSORS
D - HALL EFFECT TRANSDUCER (EVENT TRIGGERING)
E - 4 ARM STRAIN GAGE BRIDGES (GEAR TORQUE)
F - 4 ARM STRAIN GAGE BRIDGE (DRIVE MOTOR TORQUE)
G - 1 AND 2 ARM STRAIN GAGES (GEAR FILLET STRAIN)
H - COMPLETION BRIDGES AND FM/FM TRANSMITTERS (DATA TRANSMISSION)

Plate 4.1 - Transducer Location on the Gear Testing Apparatus

sensors will output one of three voltages which will indicate either a nominal flow, no flow, or sensor error condition to the microcomputer.

For various types of tests, it is beneficial to have a trigger signal available from the shaft. For example, when dynamically measuring the strain in the fillet of a gear tooth, data is required only as the tooth of interest passes through the mesh. Collecting data continuously from a gear tooth in this type of test would likely overload the storage and data transfer capabilities of the microcomputer. A much better method of data collection would be to use a trigger which would start data collection just prior to the tooth entering the mesh. A measured shaft's rotational speed, and the theory discussed in Chapter 2 could be used to determine when the tooth would have left the mesh. Data collection could, of course, be stopped at this point. A Hall Effect transducer is mounted adjacent to the driven shaft as shown in Figure 4.1 and Plate 4.1. It is coupled with a magnet which is bonded to a carrier which can be rotated to any position on the shaft. This carrier permits a coarse determination of trigger position. The output of a Schmidt trigger attached to the Hall Effect transducer is sent to a custom built delay generator. The delay generator will invert and delay the Schmidt trigger signal's arrival at the microcomputer by 0 - 9990 microseconds in 10 microsecond intervals. This will permit more precise triggering.

Strain gage bridges are mounted in three locations on the driving shaft. Two four-arm bridges are mounted between the master and test gears as indicated by "E" in Figure 4.1 and Plate 4.1. These gages are used to measure the driving shaft strain which can be used to determine gear torque and recirculating power. The four-arm bridge indicated by "F" is mounted on the output shaft of the drive motor, and is used to determine the input power to the test rig. Comparison of the input power to the recirculating power can be used to determine the fraction of recirculating power which is lost to friction from Equation 3.2.

During testing, gears will be instrumented with a variety of strain and/or temperature sensors. These sensors will be mounted somewhere on the gear body or teeth as indicated by "G" in Plate 4.1. Wires from these sensors lead out of the gear housings and underneath the bearings along specially machined keyways. Four FM/FM telemetry systems (two strain and two temperature) are available for mounting in

housings indicated by "H" in Plate 4.1. These split housings have been machined to accommodate the FM/FM transmitter, power supply and any completion bridge necessary for the circuit. Signals from the transmitters are received by rigid concentric antennae which forward the signal to the FM/FM receivers and microcomputer. Details of the locations and types of strain gages used in this investigation will be discussed in Chapter 5.

4.2 Microcomputer Based Data Acquisition System

A 80286 microcomputer is used as the basis of the data acquisition system. The microcomputer contains a MetraByte Dash 8 data acquisition board which is attached to a STA-08 interface module. The STA-08 interface module is directly attached to all of the transducers described in Section 4.1. A block diagram and specifications from the Dash 8 board are shown in Figure 4.2. The connection of the STA-08 interface module to the transducers is shown in Figure 4.3. The various pieces of measurement equipment which send signals to the STA-08 interface module are shown in Plate 4.2.

The Dash 8 data acquisition card is controlled by the microcomputer through a series of subroutines which may be interpreted under MS-BASIC or GW-BASIC, or compiled directly with MS QuickBasic. The author has written a number of subroutines which perform calibrations, collect data and check the operational status of each of the transducers previously described. These subroutines may be combined in various ways depending on the needs of a particular test program.

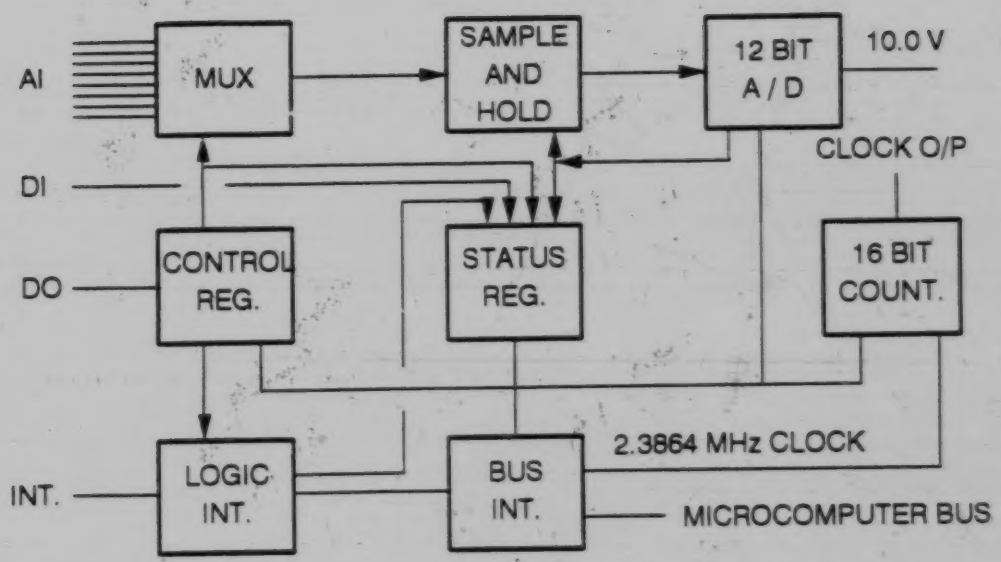

ANALOG INPUT		A/D SPECIFICATIONS		COUNTER / TIMER		SAMPLE / HOLD	
Resolution	12 bits	Type	Successive Approximation	Type	8253-5 Prog. Int.	Acqui. Time	15 µs
Accuracy	0.01% +/- 1 bit	Conversion Time	25-35 µs	Counters	3 Down 16 bit	Dynamic Error	1 bit @ 2000 V/s
Full Scale	+/- 5 V	Linearity	+/- 1 bit	Maximum Frequency	2.6 MHz		
Coding	Offset Binary	Zero Drift	10 ppm / °C	Active Count Edge	Negative	INTER.	INPUTS
Overvoltage	+/- 35 V	Gain Drift	50 ppm / °C	Max. Clock Pulse Width	230 ns high 150 ns low	Edge Triggered	Positive
Type	Single Ended	Throughput	30000 samples/sec.			Level	2 - 7
Input Current	100 nA max.						

Figure 4.2 - Block Diagram and Specifications for the MetraByte Dash 8 Data Acquisition Board

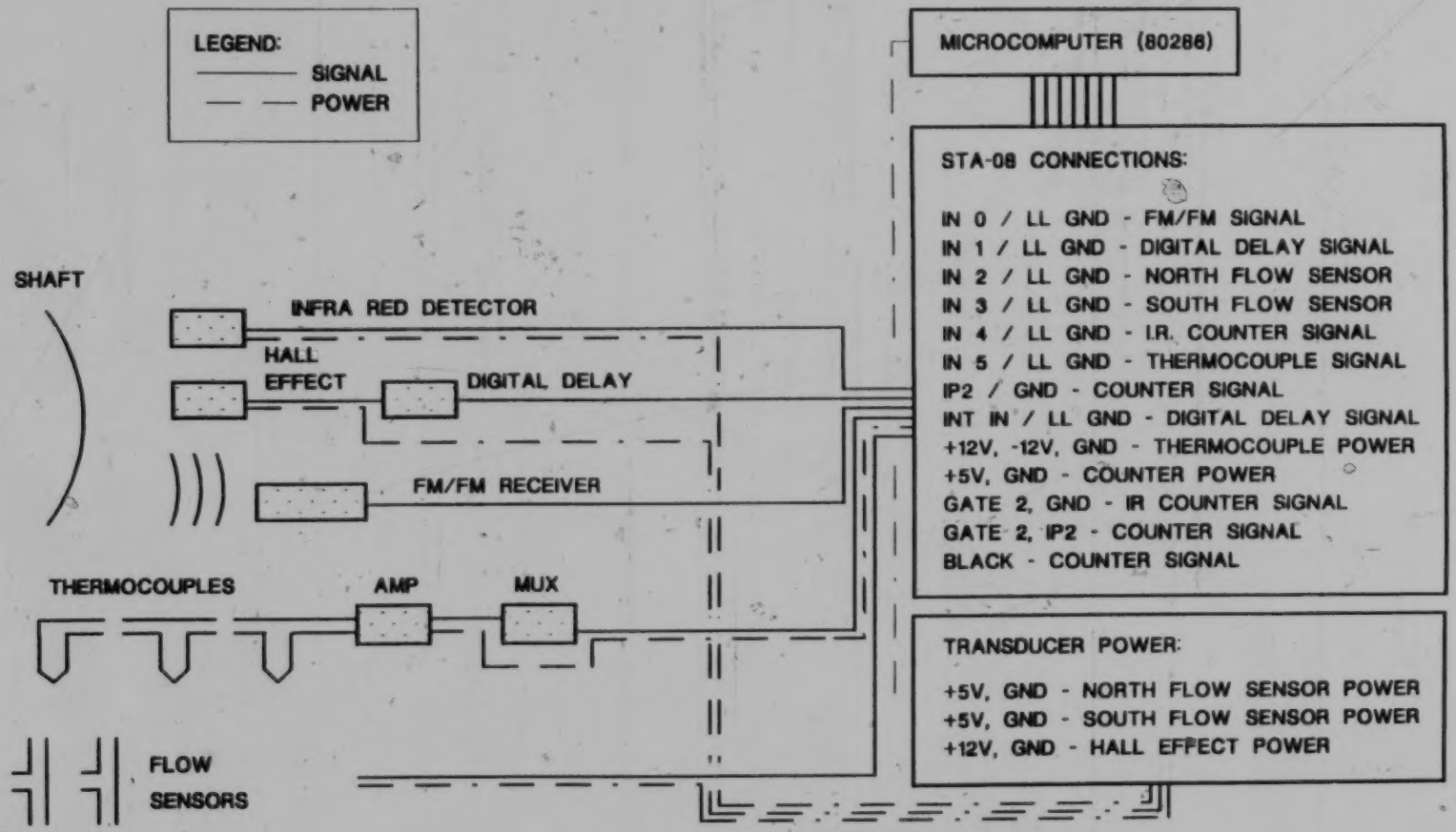
LEGEND:
SIGNAL
POWER
MICROCOMPUTER (80286)
STA-08 CONNECTIONS:
IN 0 / LL GND - FM/FM SIGNAL
IN 1 / LL GND - DIGITAL DELAY SIGNAL
IN 2 / LL GND - NORTH FLOW SENSOR
IN 3 / LL GND - SOUTH FLOW SENSOR
IN 4 / LL GND - I.R. COUNTER SIGNAL
IN 5 / LL GND - THERMOCOUPLE SIGNAL
IP2 / GND - COUNTER SIGNAL
INT IN / LL GND - DIGITAL DELAY SIGNAL
+12V, -12V, GND - THERMOCOUPLE POWER
+5V, GND - COUNTER POWER
GATE 2, GND - IR COUNTER SIGNAL
GATE 2, IP2 - COUNTER SIGNAL
BLACK - COUNTER SIGNAL
TRANSDUCER POWER:
+5V, GND - NORTH FLOW SENSOR POWER
+5V, GND - SOUTH FLOW SENSOR POWER
+12V, GND - HALL EFFECT POWER
SHAFT
INFRA RED DETECTOR
HALL EFFECT
DIGITAL DELAY
FM/FM RECEIVER
THERMOCOUPLES
AMP
MUX
FLOW SENSORS

Figure 4.3 - Schematic of Signal and Data Line Connections Between the Gear Testing Apparatus and the Microcomputer Based Data Acquisition System

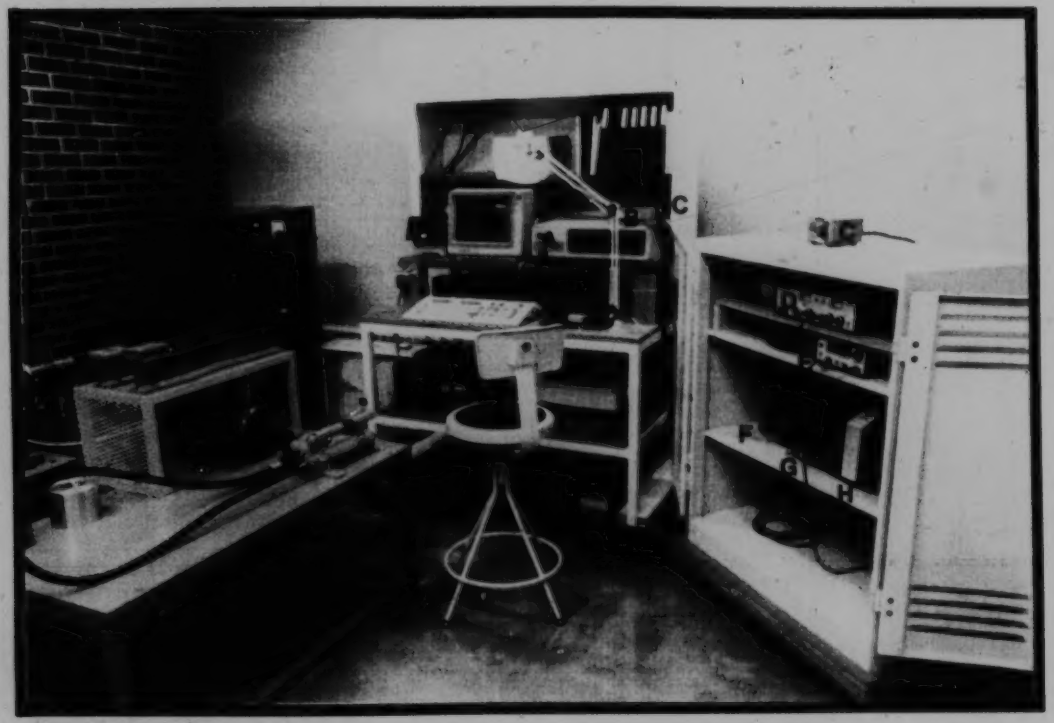

EQUIPMENT DESCRIPTION:

A - 80286 BASED MICRCOMPUTER WITH DASH 8 CARD
B - STA-08 INTERFACE MODULE
C - TRANSDUCER POWER
D - FM/FM TELEMETRY RECEIVER
E - DELAY GENERATOR
F - THERMOCOUPLE AMPLIFIER
G - THERMOCOUPLE MULTIPLEXER
H - ICE POINT REFERENCE

Plate 4.2 - Gear Testing Apparatus Measurement Equipment

Chapter 5: Experimental Investigation

5.1 Introduction

An experimental investigation was performed in order to measure the variation of tensile fillet strain throughout the meshing process for various classes of spur and helical gears. The measured value of the maximum fillet strain is compared to the value predicted by Colbourne's method which was described in Chapter 2. The location along the path of contact at which the maximum fillet strain occurs is compared to the location predicted by Colbourne's method and AGMA 2001-B88 [1].

5.2 Test Gear Design

5.2.1 Gear Tooth Profile

The subject of spur and helical gear design is discussed in many gear tests [19, 32, 33, 40]. Also, individual investigators have performed studies on specific aspects of gear design such as improving efficiency [18, 20], minimizing static transmission errors [41] and preventing gear tooth interference [42]. From all of these investigations, a common set of spur and helical gear design parameters can be formed:

1. The gear set must satisfy design speed and power requirements.
2. The design life of the gear must be known.
3. A gear material must be chosen which possesses the necessary strength and endurance limit.
4. A heat treatment and machining method must be prescribed which ensures that the required tooth surface hardness is achieved, and the surface roughness is below the specified level.
5. The tooth proportions must be reasonable, that is, the tooth must not be too long or pointed.
6. The pinion and gear are often designed to be of equal strength.
7. Tooth tip interference must be eliminated.
8. Profile modifications such as crowning may be prescribed.
9. The design should minimize the adverse effects of manufacturing errors (profile, spacing, and runout errors).
10. The cost of the gears must be acceptable.

Four spur gears and four helical gears were designed for the experimental investigation. To meet the goals of the current investigation, and of future dynamic testing, the following additional requirements were imposed:

11. All of the gear pairs should be capable of transmitting the maximum recirculating power which can be produced by the testing apparatus.
12. The gear fillets should be sufficiently large enough to permit the mounting of strain and temperature gages.
13. In order to minimize manufacturing costs, gear ratios equal to 1 and identical tooth profiles were specified for meshing gear pairs.
14. The number of teeth in each of the gear pairs were not to be multiples of each other, so as to permit unique identification of each gear's pair's vibration spectra during dynamic testing.
15. The two helical gear pairs were to be designed with face contact ratios of approximately 0.5 and 1.0. A helical gear pair with a face contact ratio of 0.5 should undergo a wide variation of load intensity throughout the meshing cycle while the load intensity should remain constant for a helical gear pair with a face contact ratio of 1.0.

The gears were designed using software written by Colbourne and modified by the author. The software, for the case of helical gears, inputs the normal module, normal pressure angle, desired operating center distance, number of teeth, rack cutter addendum, tip radius, and either the standard helix angle or axial pitch. The profile shift of each tooth in the gear pair was varied until the following conditions were met:

- there was no undercutting in either gear,
- clearances were greater than 0.25 m_n,
- the profile contact ratio was greater than 1.2, and
- there was no interference at either gear tip.

5.2.2 Gear Body Design and Manufacture

Once the design of the gear tooth profiles was complete, the gear blank and hub were designed. Both integral blank and hub and separable blank and hub designs

were considered. The separable blank and hub design offered the following advantages:

- This design had significantly lower material and machining costs.
- Separable blanks could be stacked in the hobbing machine thereby significantly reducing gear cutting cost.

The gear blanks were machined from AISI 4340 through hardened round bar, and the gear hubs were machined from AISI 1020 round bars. Two options were investigated for attaching the hub to the blank: welding, and a pin and bolt connection. The welding procedure would involve preheating at 275 degrees Celsius, welding with an E 8018 C1 electrode, and stress relieving at 625 degrees Celsius. As appropriate facilities for this procedure could not be obtained on an ongoing basis, the pin and bolt connection design was chosen.

The gear blanks and hubs were prepared at the University of Alberta, and the gear teeth were cut by a local manufacturer on a Barber-Colman type "D" hobbing machine. No subsequent heat treating or machining was performed. The final specifications for the gears are shown in Table 5.1.

5.3 Test Procedure

5.3.1 Strain Gage Locations

The eight test gears were instrumented with 27 bondable strain gages. The gages were mounted on tensile driven tooth fillets in such a manner that the gage backing extended as closely as possible to the gears' form radius while providing sufficient clearance for the gage backing, grid, and lead wires. Three different types of gages were used and were compared in terms of ease of installation and performance. The location of the strain gages is shown in Table 5.2.

5.3.2 Test Procedure

In order to measure accurately the variation of static tensile fillet strains through the meshing cycle, a device was required which would permit the gears to be rotated in increments of less than 0.1 degrees. This was accomplished with the use of a static positioner which is shown schematically in Figure 5.1. The device consists of a straight bar with its one end attached to the driving shaft of the gear testing rig by

Table 5.1 - Test Gear Description

Gear Number	S1	S2	S3	S4	H1	H2	H3	H4
Normal Pressure Angle, degrees	20.00	20.00	20.00	20.00	20.00	20.00	20.00	20.00
Normal Module, mm	5.00	5.00	8.00	8.00	6.00	6.00	8.00	8.00
Number of Teeth	64	64	40	40	48	48	36	36
Face Width, mm	25.00	25.00	25.00	25.00	45.45	45.45	30.00	30.00
Blank Diameter, mm	330.00	330.00	336.00	336.00	332.00	332.00	336.00	336.00
Standard Helix Angle, degrees	0	0	0	0	24.76	24.76	24.76	24.76
Axial Pitch, mm	-	-	-	-	45.00	45.00	60.00	60.00
Face Contact Ratio	0	0	0	0	1.01	1.01	0.50	0.50
Chordal Addendum, mm	5.05	5.05	8.12	8.12	10.30	10.30	13.41	13.41
Chordal Tooth Thickness, mm	7.68	7.68	12.34	12.34	7.33	7.33	9.28	9.28
Cutter Addendum, mm	6.10	6.10	10.11	10.11	7.54	7.54	10.11	10.11
Cutter Tip Radius, mm	1.60	1.60	3.16	3.16	2.25	2.25	3.16	3.16
Blank Material (AISI)	4340	4340	4340	4340	4340	4340	4340	4340
Through Hardness, BHN	300	300	300	300	300	300	300	300
Ultimate Strength, MPa	1035	1035	1035	1035	1035	1035	1035	1035
Yield Strength, Mpa	860	860	860	860	860	860	860	860

Table 5.2 - Strain Gage Locations

Gage Number	Gear Number	Fillet Number	z / F	Gage Type	Gage Factor
1	S3	1	0.50	CEA-06-062UW-350	2.17
2	S3	2	0.50	CEA-06-062UW-350	2.17
3	S3	17	0.50	CEA-06-062UW-350	2.17
4	S3	29	0.50	CEA-06-062UW-350	2.17
5	S4	1	0.50	CEA-06-062UW-350	2.17
7	S4	14	0.50	CEA-06-062UW-350	2.17
8	S4	26	0.50	CEA-06-062UW-350	2.17
9	S4	27	0.50	CEA-06-062UW-350	2.17
10	S1	1	0.50	EA-06-060EK-350	2.055
11	S2	1	0.50	EA-06-060EK-350	2.055
12	S2	48	0.50	EA-06-060EK-350	2.055
13	H3	1	0.50	CEA-06-062WT-350	2.12
14	H3	7	0.50	CEA-06-062WT-350	2.12
16	H3	20	0.50	CEA-06-062WT-350	2.12
17	H3	30	0.50	CEA-06-062WT-350	2.12
18	H4	1	0.50	CEA-06-062UW-350	2.17
19	H4	16	0.50	CEA-06-062UW-350	2.17
20	H4	23	0.50	CEA-06-062UW-350	2.17
21	H4	30	0.50	CEA-06-062UW-350	2.17
22	H1	1	0.50	EA-06-060EK-350	2.055
23	H1	17	0.20	EA-06-060EK-350	2.055
24	H1	18	0.35	EA-06-060EK-350	2.055
25	H1	19	0.50	EA-06-060EK-350	2.055
26	H2	1	0.50	EA-06-060EK-350	2.055
27	H2	17	0.50	EA-06-060EK-350	2.055
28	H2	25	0.50	EA-06-060EK-350	2.055
29	H2	37	0.50	EA-06-060EK-350	2.055

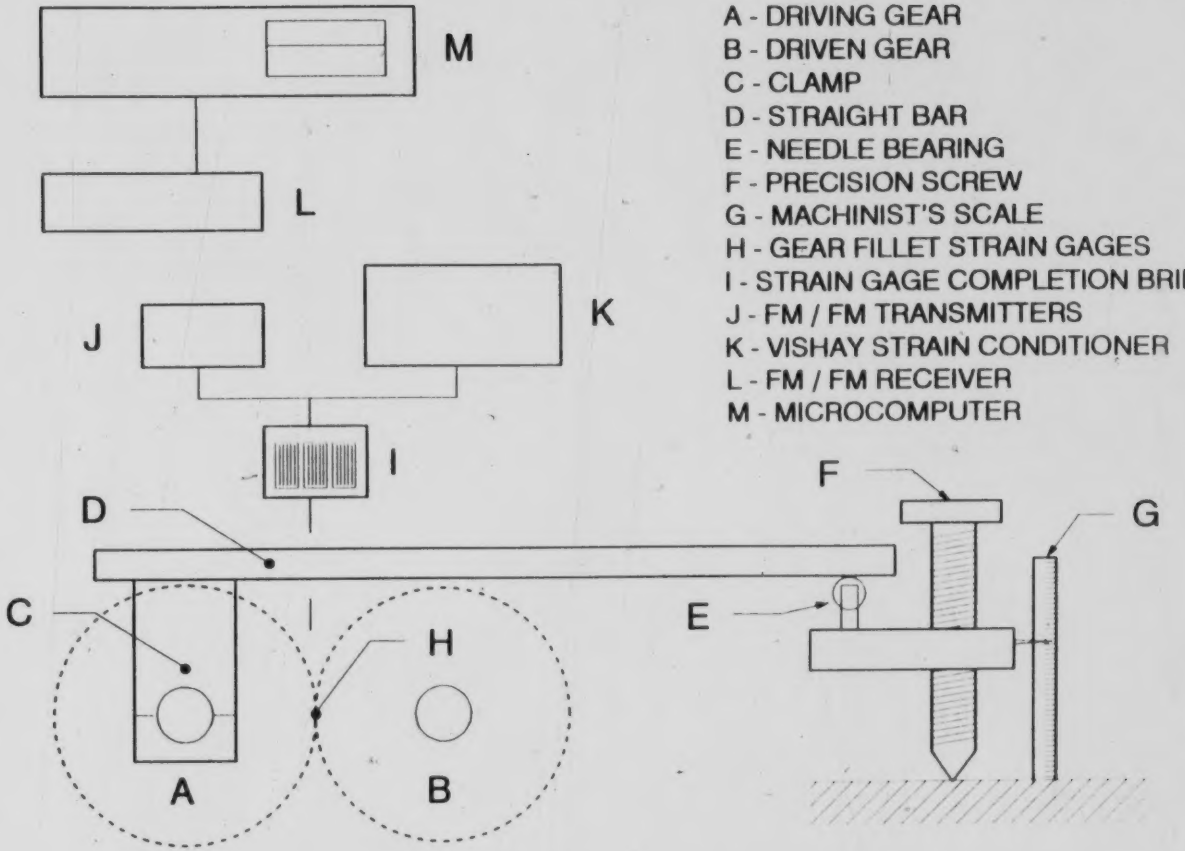

Figure 5.1 - Static Positioner Schematic

means of a removable clamp. The other end of the bar rides on a small needle bearing mounted in a housing which can be raised or lowered by means of a precision instrument screw. The position of the bearing housing is indicated on the machinist's scale attached to the vertical member of the positioner. The absolute height of the bearing housing can be directly related to the angle of the straight bar with respect to the horizontal as shown in the calibration curve of Figure 5.2. Any angular rotation of the bar is equal to the angular rotation of the gear on the driving shaft. The relative rotation of the gear can be related to a change of contact point location along the line of contact with Equation 2.2.

During testing, the static positioner was used to locate the gear at various positions throughout the meshing cycle. As shown in Figure 5.1, the tensile fillet strain would then be read by either the Vishay strain conditioner or the FM/FM telemetry receiver. Voltages corresponding to the tensile fillet strain were sent directly to the IBM PC compatible computer from the FM/FM telemetry receiver while the strain conditioner readings were manually entered.

Testing first involved running the gears in for approximately 1000 000 cycles at 1000 r.p.m. with half of the cycles transmitting 100 Nm, the other half transmitting 500 Nm. Static strain levels were then measured throughout the meshing process at 27 strain gage locations for input torque levels of 413 Nm, 827 Nm, and 1241 Nm. As mentioned in Chapter 4, input torque levels were monitored on the two four arm driving shaft strain gage bridges. These torque levels were chosen for the following reasons:

- Tooth loading resulting from these torques is consistent with other investigations.
- The resulting strains covered a significant portion of the measurement equipment's range.
- These static stress levels are consistent with stress levels which would be statically applied prior to future full speed dynamic testing.

At the completion of each test, the contact pattern between the gear teeth was determined by covering the driven tooth's surface with a thin coating of machinists blue and by then passing the tooth through the contact region two to four times. The contact pattern was transferred directly to paper, allowed to dry, and then digitized.

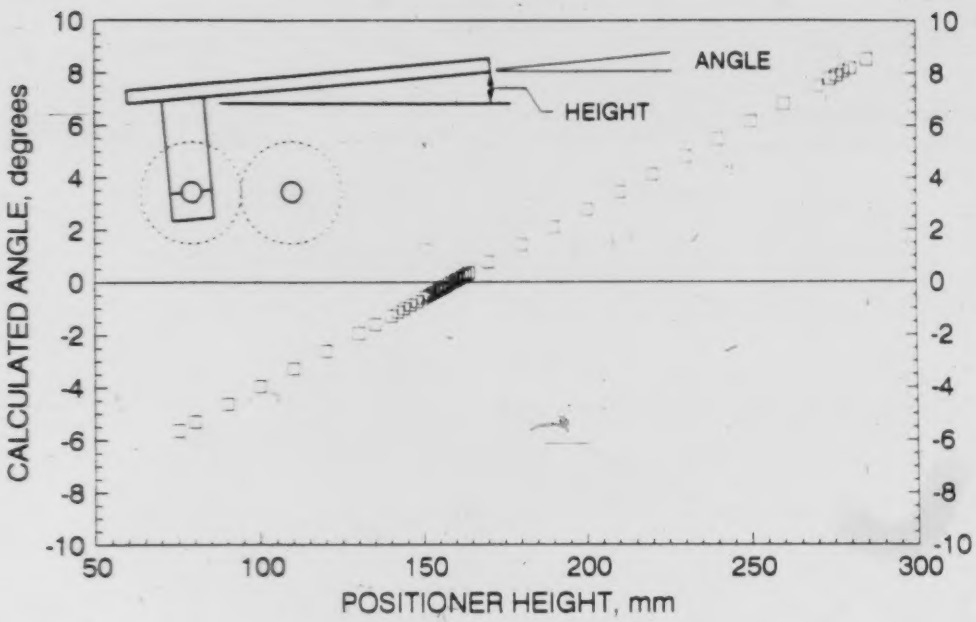

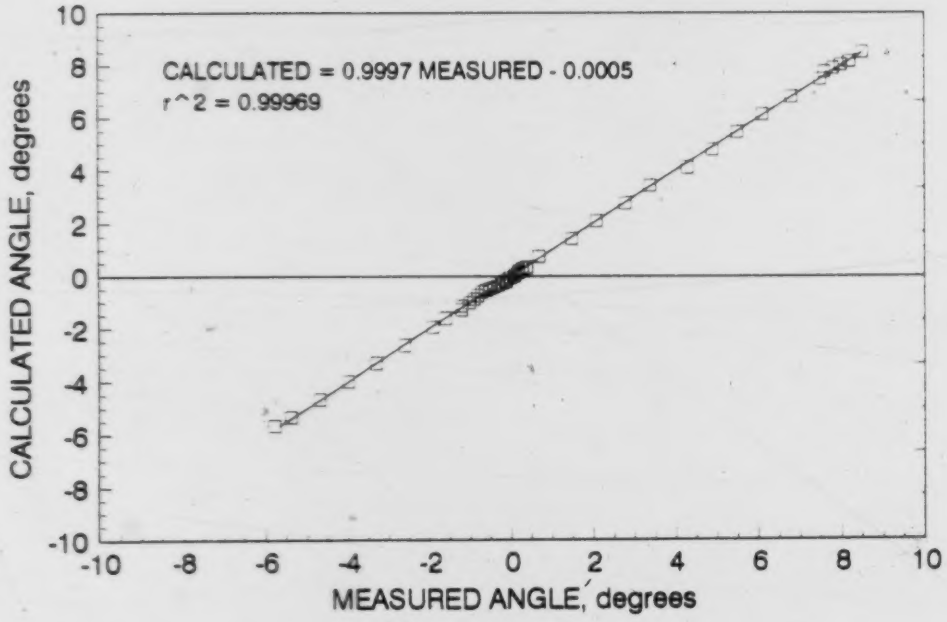

Figure 5.2 - Static Positioner Calibration Curve

5.4 Test Results

5.4.1 Theoretical Variation of Strain Through the Meshing Cycle of Spur Gears S1-S4

The variation of tensile fillet strain through the meshing cycle can be better understood by examining the variation of two of its major components - load intensity and load radius - through the meshing cycle. Figure 5.3 shows the variation of tensile fillet strain, load intensity, and load radius along a line of contact for the 5 module spur gears (Gears S1 and S2). The quantities shown have been normalized: tensile fillet strain and load intensity with respect to their maximum values, and load radius as a fraction of total load radius. The reader will recall from Figure 2.8 that since the lines of contact of a spur gear are parallel to the top and bottom sides of the plane of contact, the values shown in Figure 5.3 are, therefore, equally valid for all transverse sections. From Figure 5.3, it is obvious that the normalized load radius decreases as the contact point moves from s_{max} to s_{min} (Δs is defined as was shown in Figure 2.6). The rate of decrease of normalized load radius is slightly nonlinear, being a maximum at $\Delta s/s_{TOT} = 0$ and a minimum at $\Delta s/s_{TOT} = 1$. The normalized load intensity remains constant from $\Delta s/s_{TOT} = 0$ to $\Delta s/s_{TOT} = 0.45$. Between $\Delta s/s_{TOT} = 0.45$ and $\Delta s/s_{TOT} = 0.55$, the normalized load intensity achieves its maximum value. This zone corresponds to the region of single tooth contact of the gear pair. After the load point passes through the region of single tooth contact, the normalized load intensity remains constant at half its maximum value. The combination of these two curves is shown in the normalized tensile fillet strain curve. As was discussed in Chapter 2, for accurately cut spur gears, load intensity is the parameter which contributes most significantly towards the value of the tensile fillet strain. This is shown in Figure 5.3 in that the maximum normalized tensile fillet strain occurs at the point of maximum load intensity, not maximum load radius.

Figure 5.4 shows the theoretical variation of normalized tensile fillet strain, load intensity and load radius along a line of contact for the 8 module spur gears S3 and S4. The behaviour of these curves is very similar to the corresponding curves of Figure 5.3. The location of the points of highest and lowest single tooth contact are

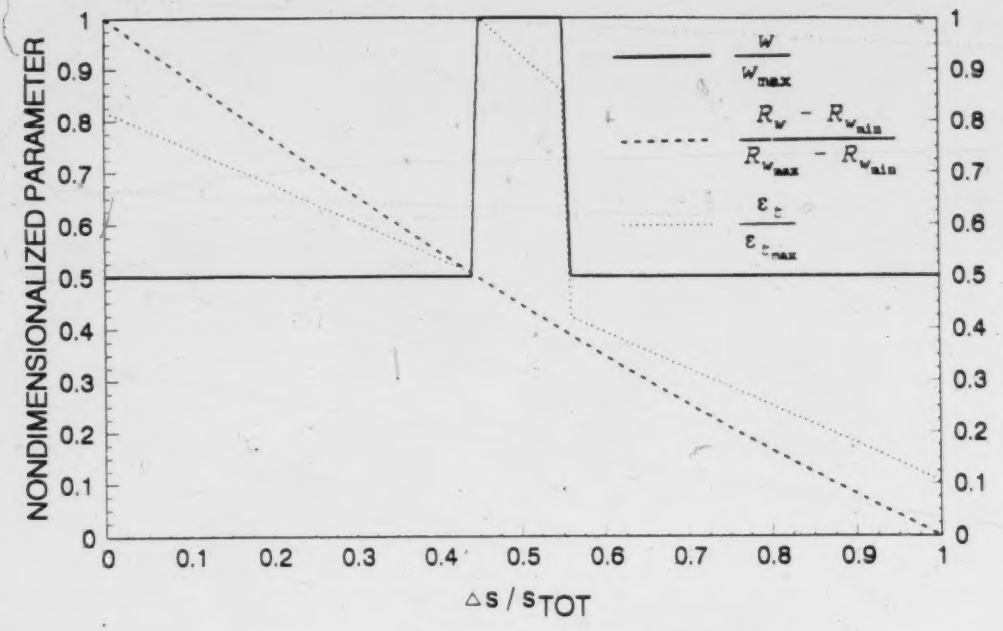

Figure 5.3 - Theoretical Normalized Tensile Fillet Strain, Load Intensity, and Load Radius Variation, 5 Module Spur Gears

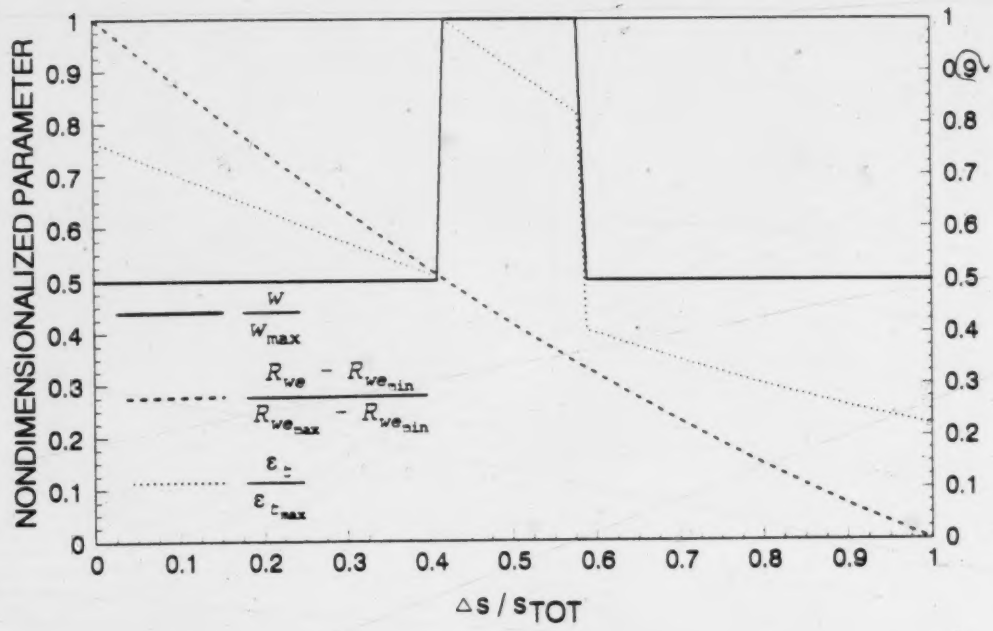

Figure 5.4 - Theoretical Normalized Tensile Fillet Strain, Load Intensity, and Load Radius Variation, 8 Module Spur Gears

different than those of the 5 module spur gears, and the region of single tooth contact is longer.

5.4.2. Measured Strain Variation for 5 Module Spur Gears S1 and S2

Figures 5.5 and 5.6 show the measured variation of strain along the line of contact and the contact patterns for Gages 10-12 with an applied torque of 413 Nm. Theoretical strains are those predicted by Colbourne's method and have been modified by the AGMA 2001-B88 [1] load distribution factor. The contact patterns are shown with the area of contact shaded, and an arrow indicating the strain gage location along the face width. From these figures, it is apparent that the measured strains are significantly lower than the theoretical strains, especially at the point of initial contact. The location of the maximum strain corresponds roughly to the region of single tooth contact. However, the increase in strain magnitude measured in this region is much smaller than theory would predict. Inspection of the contact patterns reveals that the gear teeth are lightly loaded, especially the tooth corresponding to Gage 10.

Figures 5.7 and 5.8 show the variations of strain at Gages 10-12 and the corresponding contact patterns when the transmitted torque is increased to 827 Nm. While the measured strains remain below those predicted by theory, the development of a region of higher strains corresponding to the region of single tooth contact is evident. This is especially true as the contact point leaves the region of single tooth contact and the measured strains drop noticeably. The strains observed during initial contact remained significantly below their predicted values. The increased load resulted in better contact across the tooth face, although Gage 10 still appears to be lightly loaded.

When the applied torque is increased to 1241 Nm, the resulting measured strain variations and contact patterns for the three gages are shown in Figures 5.9 and 5.10. In Figure 5.10, regions of maximum strain comparable in magnitude and shape to the region of single tooth contact are evident. In Figure 5.9, an extended region of maximum strain is shown: this is possible evidence of unequal load sharing between the instrumented tooth and the other tooth in mesh. The contact pattern for the tooth associated with Gage 10 is consistent with this tooth's contact pattern at lower applied torques. However, the contact patterns of the teeth associated with Gages 11 and 12 are

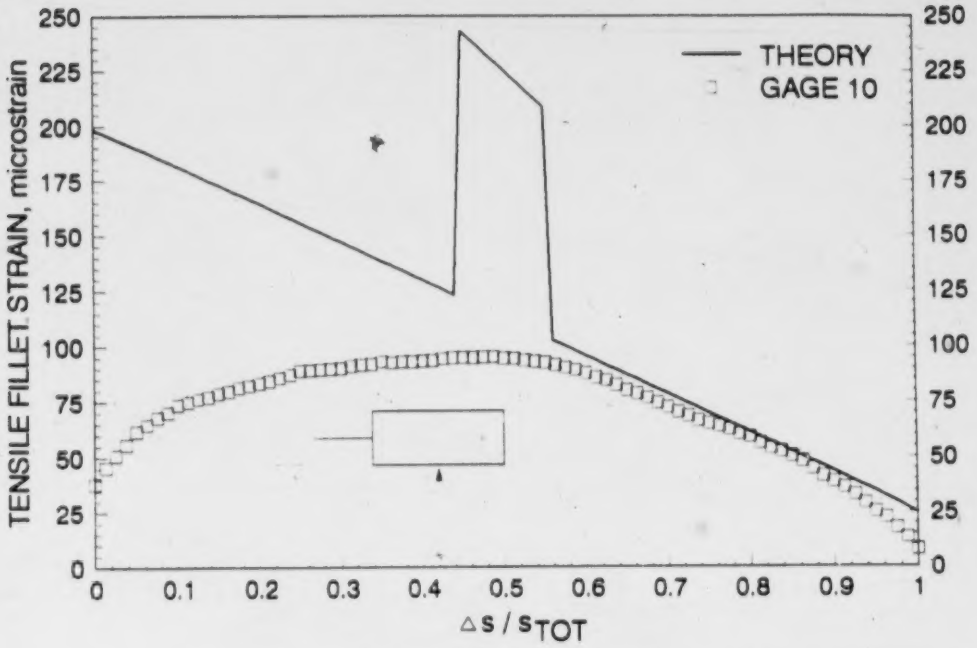

Figure 5.5 - Measured Variation of Strain Along the Line of Contact and Contact Pattern for Gage 10, Torque = 413 Nm

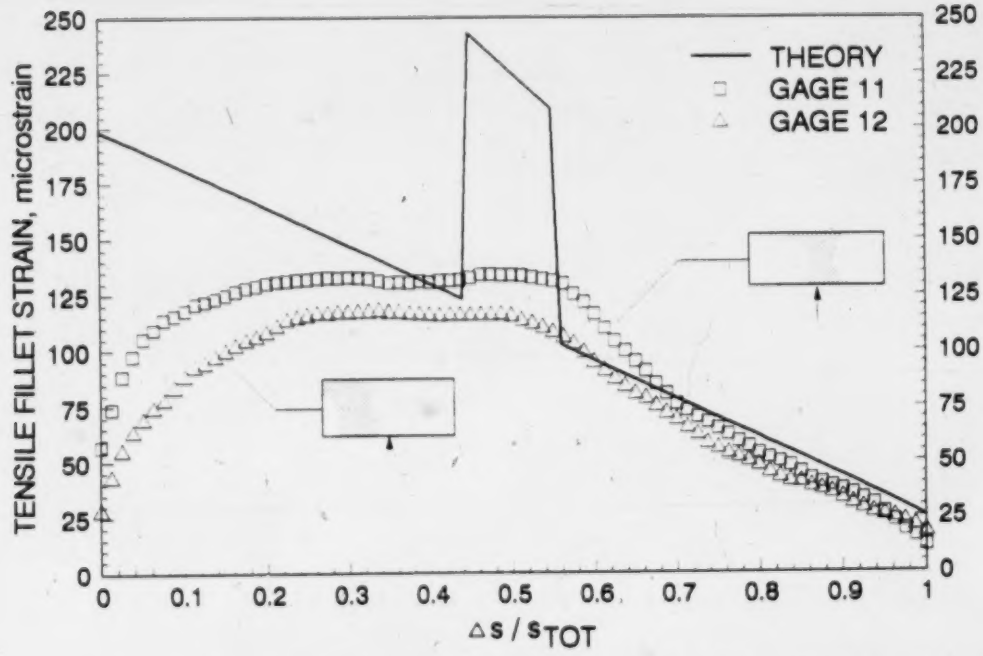

Figure 5.6 - Measured Variation of Strain Along the Line of Contact and Contact Patterns for Gages 11 and 12, Torque = 413 Nm

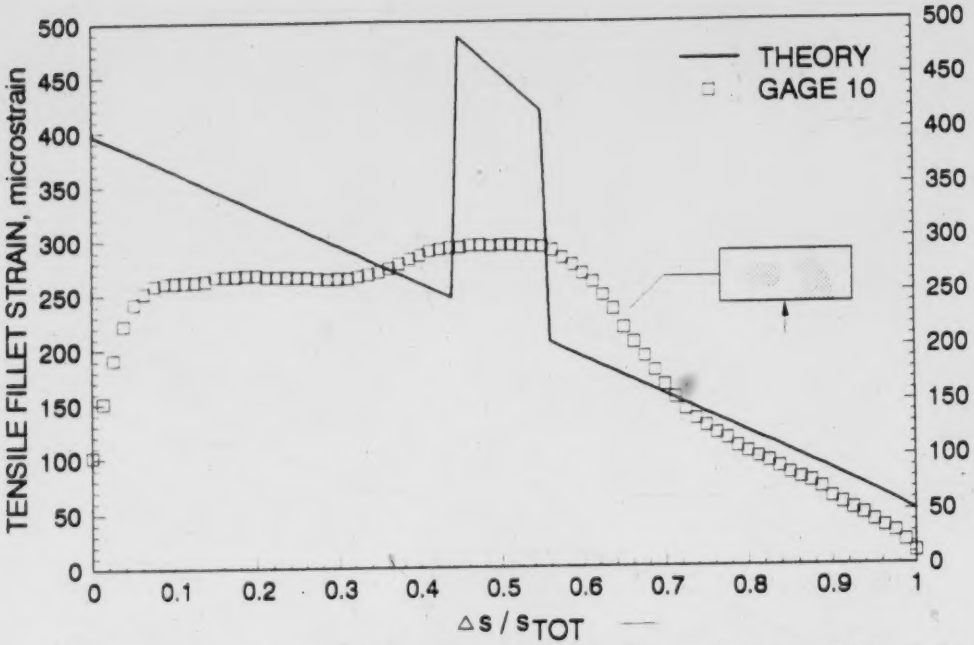

Figure 5.7 - Measured Variation of Strain Along the Line of Contact and Contact Pattern for Gage 10, Torque = 827 Nm

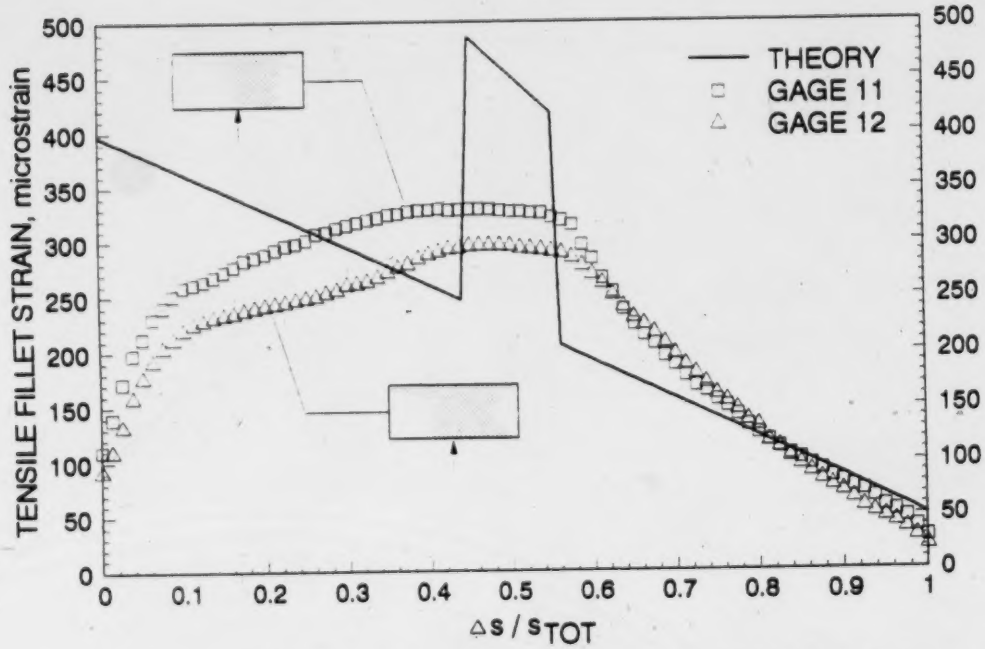

Figure 5.8 - Measured Variation of Strain Along the Line of Contact and Contact Patterns for Gages 11 and 12, Torque = 827 Nm

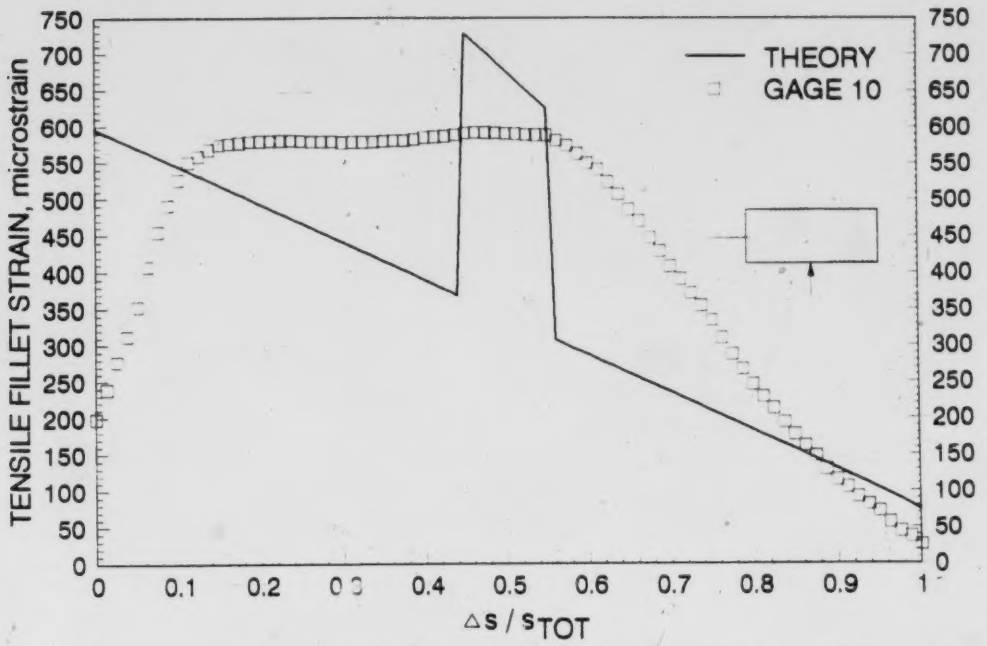

Figure 5.9 - Measured Variation of Strain Along the Line of Contact and Contact Pattern for Gage 10, Torque = 1241 Nm

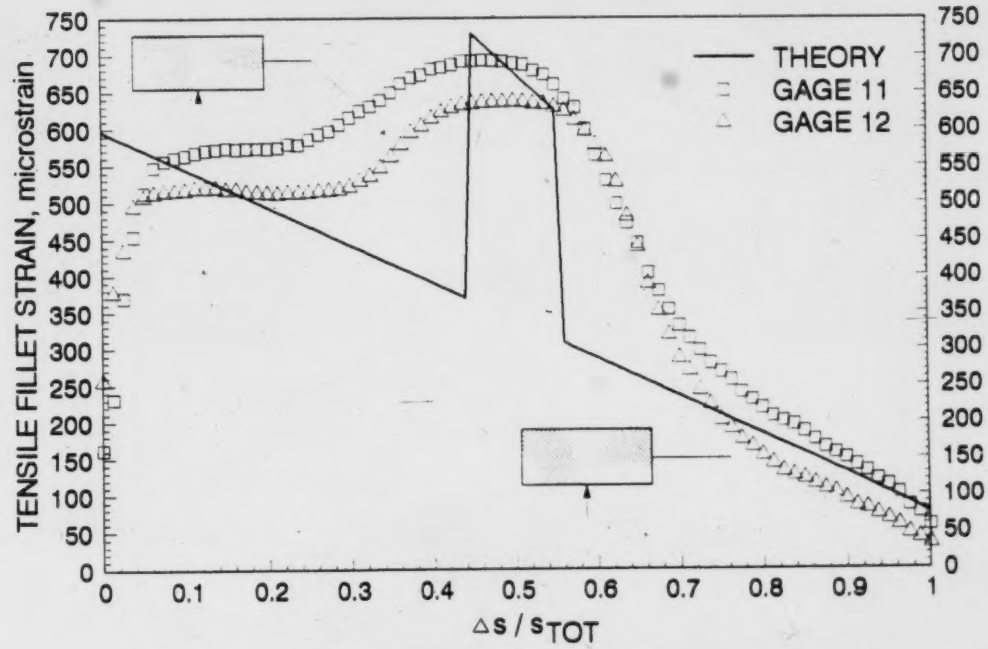

Figure 5.10 - Measured Variation of Strain Along the Line of Contact and Contact Patterns for Gages 11 and 12, Torque = 1241 Nm

different than the contact patterns at lower torques indicating a redistribution of load across these teeth's surfaces as the applied torque increases.

A collection of all of the strain measurements on the 5 module spur gears is shown in Figures 5.11-5.13 for applied torques of 413 Nm, 827 Nm, and 1241 Nm, respectively. For each of these figures, the arithmetic average and uncertainty band of all of the measured strain readings is shown. From these figures it is apparent that as the applied torque is increased, the measured variation of strain more closely approximates the theoretical curve. While the maximum strains observed are less than the theoretical maximums, the maximum measured strains occur in a zone of elevated strain corresponding approximately to the region of single tooth contact. The fillet strains observed upon entry of a contact line in the plane of contact are significantly less than the predicted values while the measured decrease in strain as the contact line leaves the plane of contact is comparable to theory.

The limited space available for mounting gages on the 5 module spur gear teeth, combined with the difficulty in mounting these gages resulted in their placement at locations comparatively low on the gear fillet. In all cases, portions of the gages extended into the root of the gear teeth. It is believed that the gage placement desensitized the gages' output to lower applied torques. As the applied torque became larger and the fillet and root region became more highly stressed, the net gage output more closely approached theoretical values.

5.4.3 Measured Strain Variation for 8 Module Spur Gears S3 and S4

Figures 5.14-5.17 show the variation of strain along the line of contact for Gages 1-9 with an applied torque of 413 Nm. As was observed for the 5 module spur gears, measured strains for the case of tip loading are less than those predicted by theory. The location of the maximum measured strain corresponds to the theoretical region of single tooth contact. In some cases, such as Gage 1, the region of single tooth contact is preceded by a region of poor load sharing between the teeth. Other locations, such as Gage 7, exhibited more ideal load distribution. The maximum measured strains varied between 40% and 72% of the theoretical maximums. A wide range of contact patterns were observed. Some patterns were indicative of light tooth loading or poor load sharing

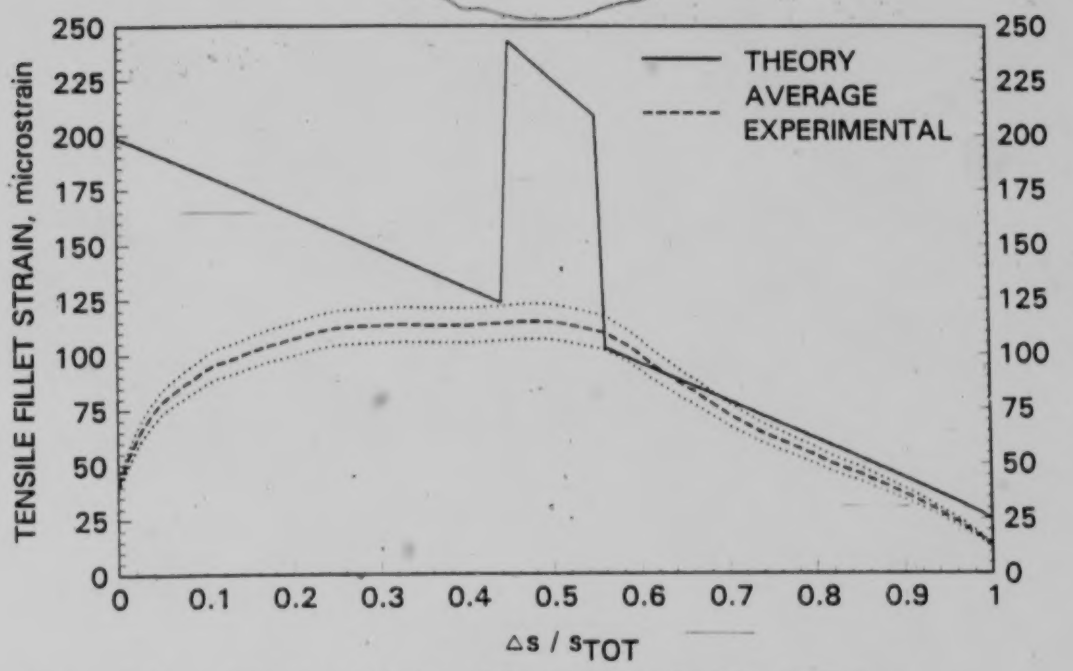

Figure 5.11 - Measured Variation of Strain Along the Line of Contact on 5 Module Spur Gears: Composite Data, Torque = 413 Nm

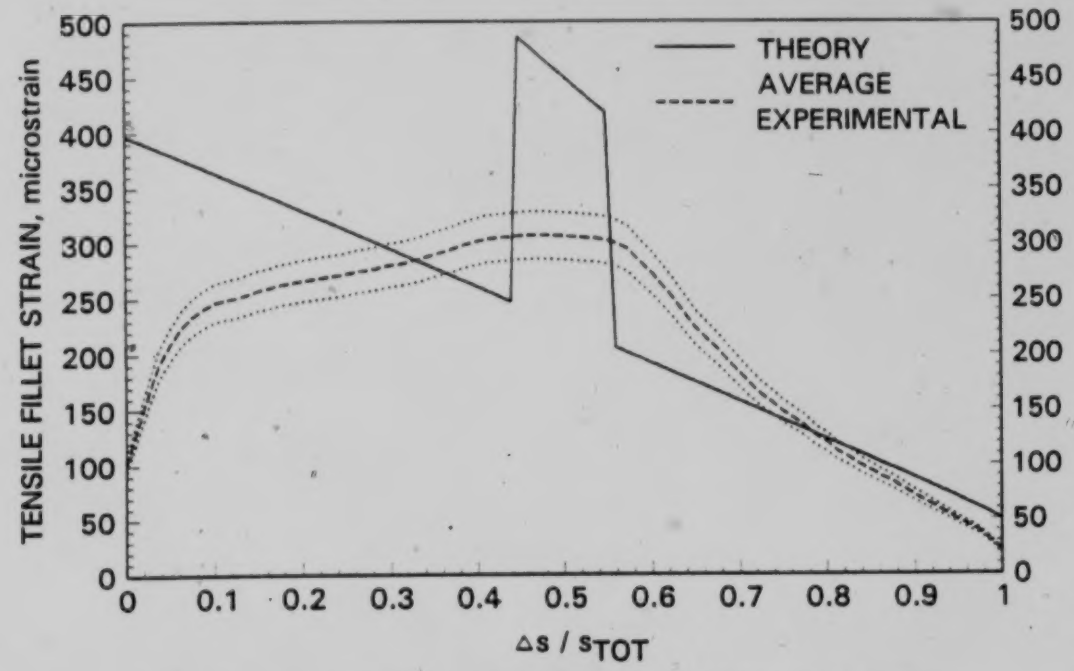

Figure 5.12 - Measured Variation of Strain Along the Line of Contact on 5 Module Spur Gears: Composite Data, Torque = 827 Nm

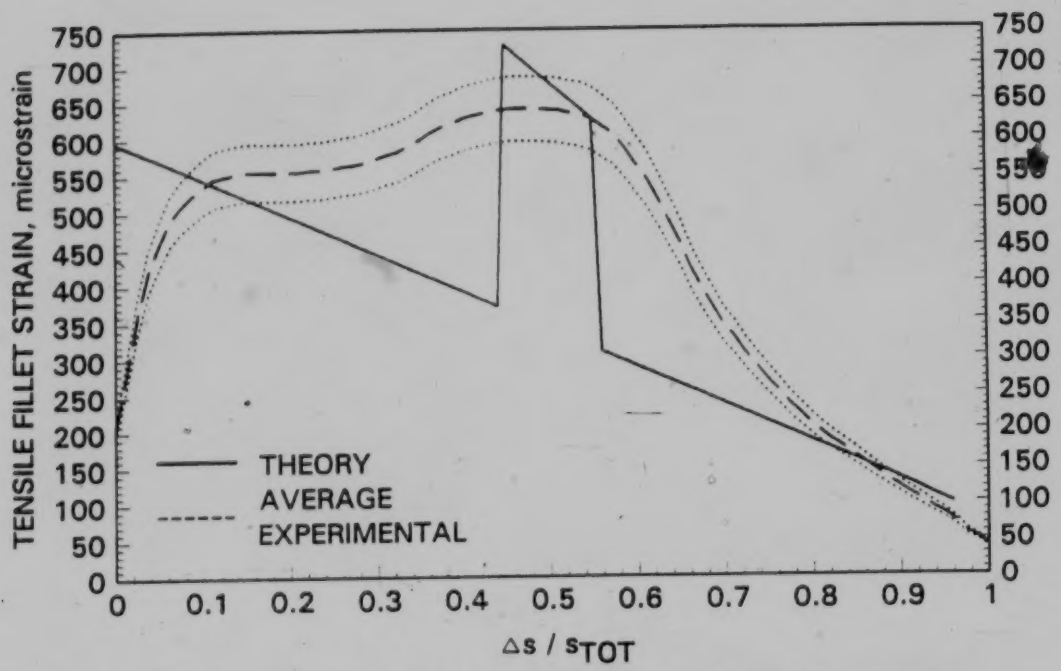

Figure 5.13 - Measured Variation of Strain Along the Line of Contact on 5 Module Spur Gears: Composite Data, Torque = 1241 Nm

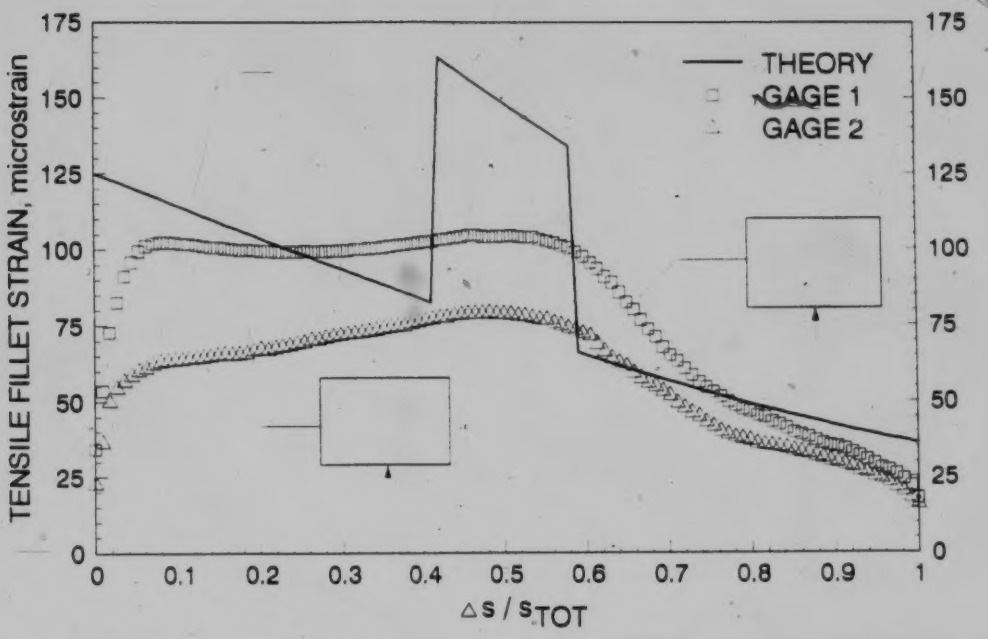

Figure 5.14 - Measured Variation of Strain Along the Line of Contact and Contact Patterns for Gages 1 and 2, Torque = 413 Nm

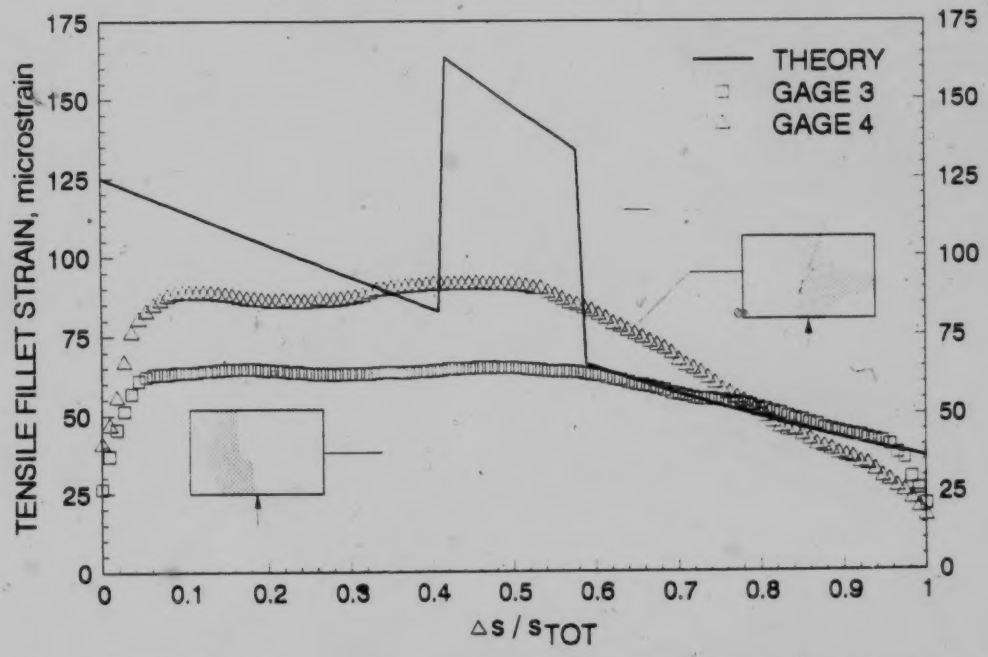

Figure 5.15 - Measured Variation of Strain Along the Line of Contact and Contact Patterns for Gages 3 and 4, Torque = 413 Nm

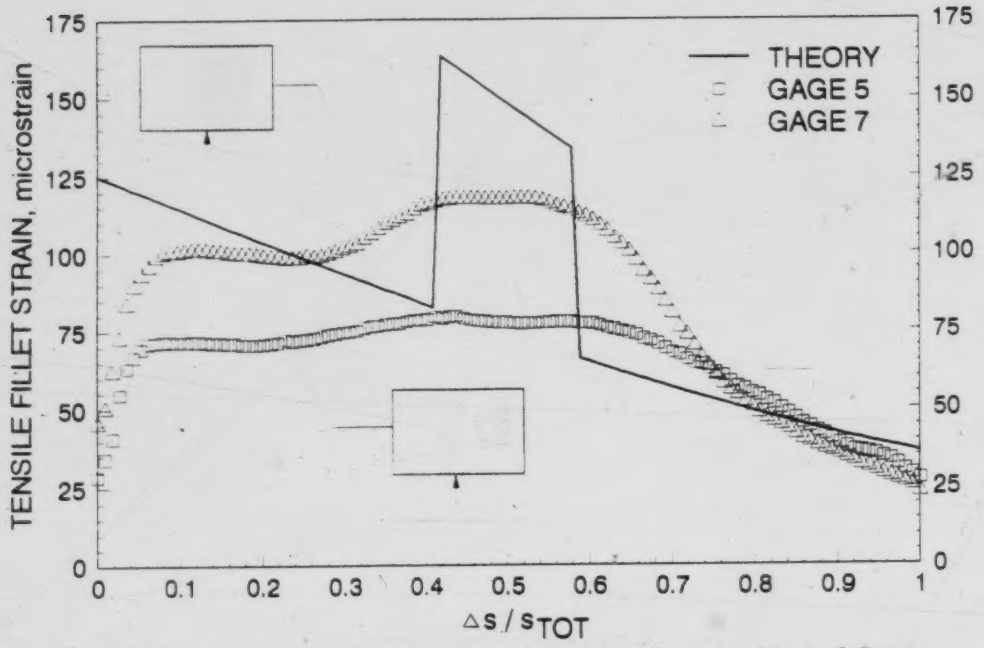

Figure 5.16 - Measured Variation of Strain Along the Line of Contact and Contact Patterns for Gages 5 and 7, Torque = 413 Nm

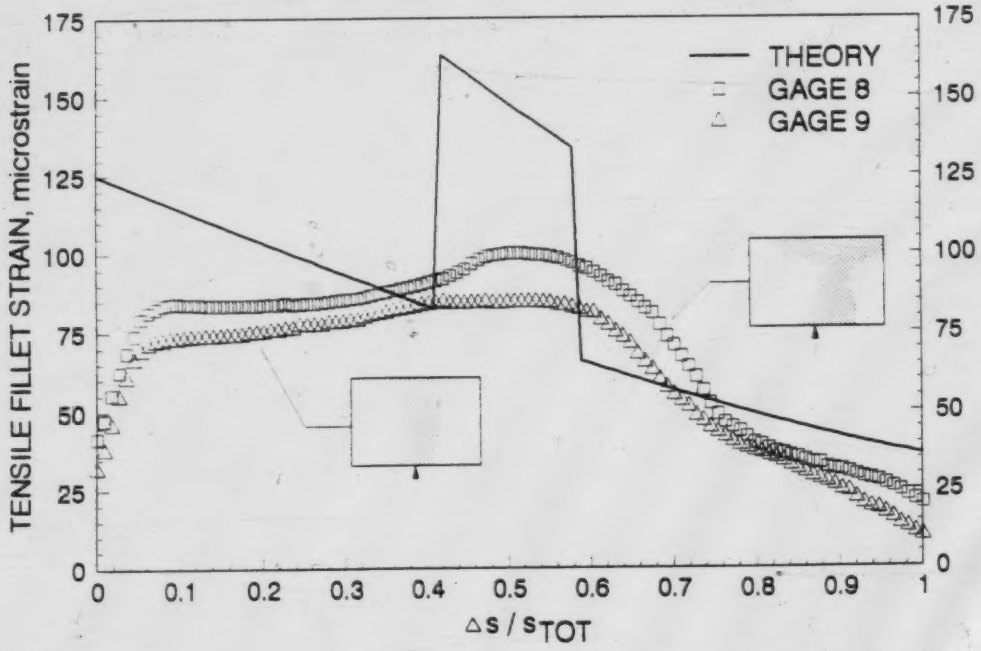

Figure 5.17 - Measured Variation of Strain Along the Line of Contact and Contact Patterns for Gages 8 and 9, Torque = 413 Nm

such as Gages 3 and 5, while Gages 1 and 7 exhibited more uniform loading.

Most gages exhibited elevated strain levels associated with regions of single tooth contact when the applied torque was increased to 827 Nm. The variation of strain and contact patterns for these cases are shown in Figures 5.18-5.21. Maximum measured strains varied between 63% and 90% of the maximum theoretical values. All contact patterns were consistent in shape with the patterns produced with an applied torque of 413 Nm. The pattern associated with Gage 3 was indicative of unsymmetrical loading while the pattern of Gage 1 exhibited approximately 85% full face contact. The rate of strain reduction as the contact line left the plane of contact was similar to theory, although the observed strain values were less than theoretical values in all cases.

The variation of strain along the lines of contact and the contact patterns resulting from an applied torque of 1241 Nm are shown in Figures 5.22-5.25. While the contact pattern associated with Gage 3 still reflects unsymmetrical loading, the remainder of the contact patterns exhibit greater than 70% full face contact. The region of single tooth contact is identifiable on all strain traces with the measured maximum strains varying between 81% and 102% of the theoretical values.

Figures 5.26-5.28 show the combined experimental and theoretical results for the 8 module spur gear tests. The average strains detected by the eight strain gages is shown for each torque level as well as an uncertainty band on the average reading. From these figures, it is apparent that the maximum measured strains occurred in the region of single tooth contact, and that the theory appears to overestimate the actual strain at both the beginning and end of the meshing cycle. The value of the average measured maximum strains were 55%, 79%, and 90% of the theoretical maximum strains for applied torques of 413 Nm, 817 Nm, and 1241 Nm, respectively.

5.4.4 Theoretical Variation of Strain Through the Meshing Cycle of Helical Gears H1-H4

Unlike spur gears, the variation of load radius, load intensity, and tensile fillet strain with position along a line of contact of a helical gear tooth is dependent upon the location of the transverse section containing the line of contact. Figure 5.29 shows the variation of normalized tensile fillet strain, load intensity, and load radius along a contact

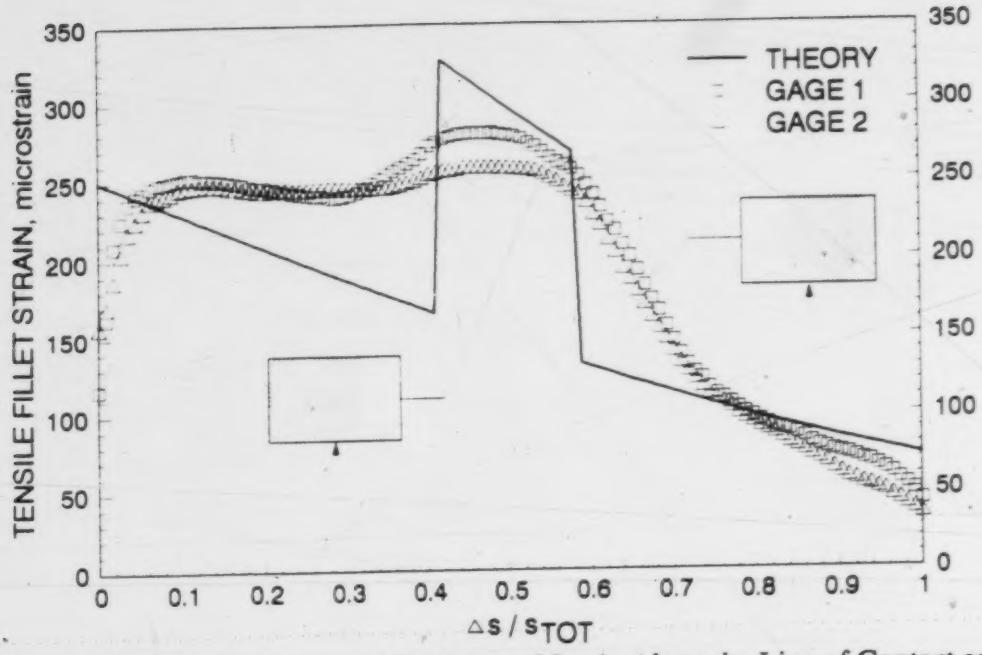

Figure 5.18 - Measured Variation of Strain Along the Line of Contact and Contact Patterns for Gages 1 and 2, Torque = 827 Nm

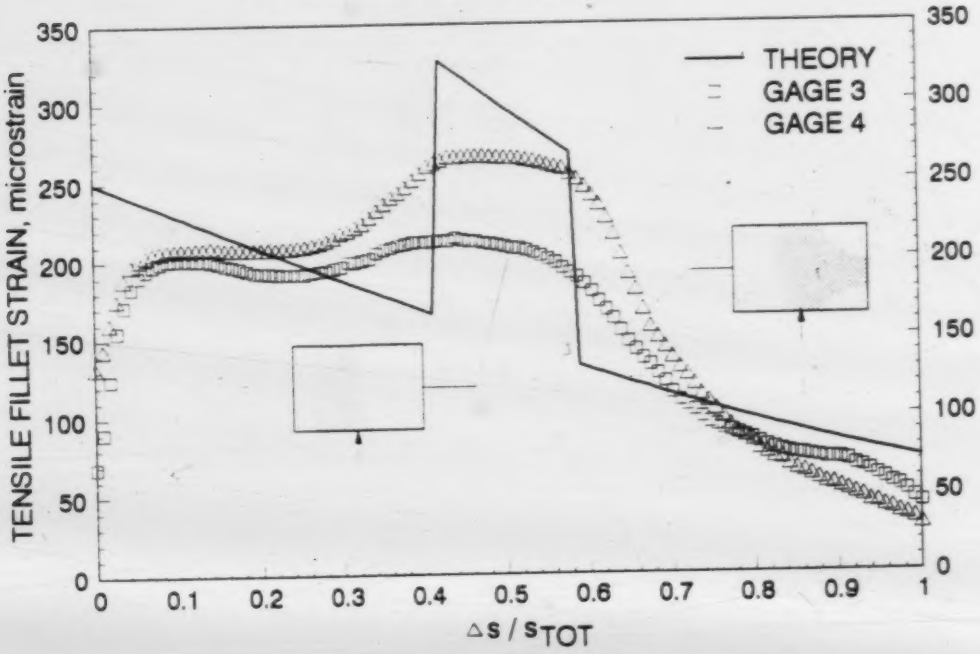

Figure 5.19 - Measured Variation of Strain Along the Line of Contact and Contact Patterns for Gages 3 and 4, Torque = 827 Nm

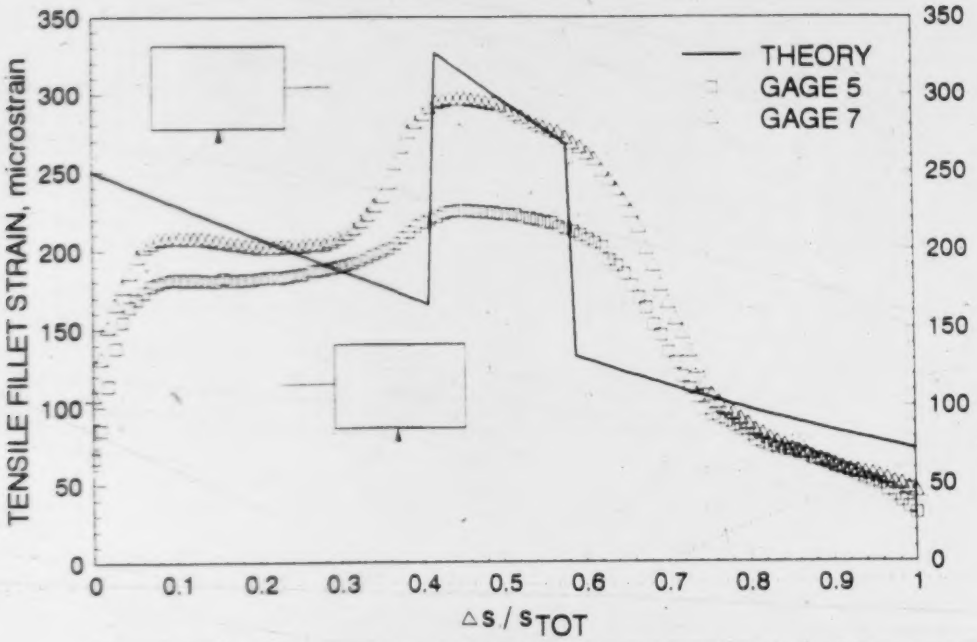

Figure 5.20 - Measured Variation of Strain Along the Line of Contact and Contact Patterns for Gages 5 and 7, Torque = 827 Nm

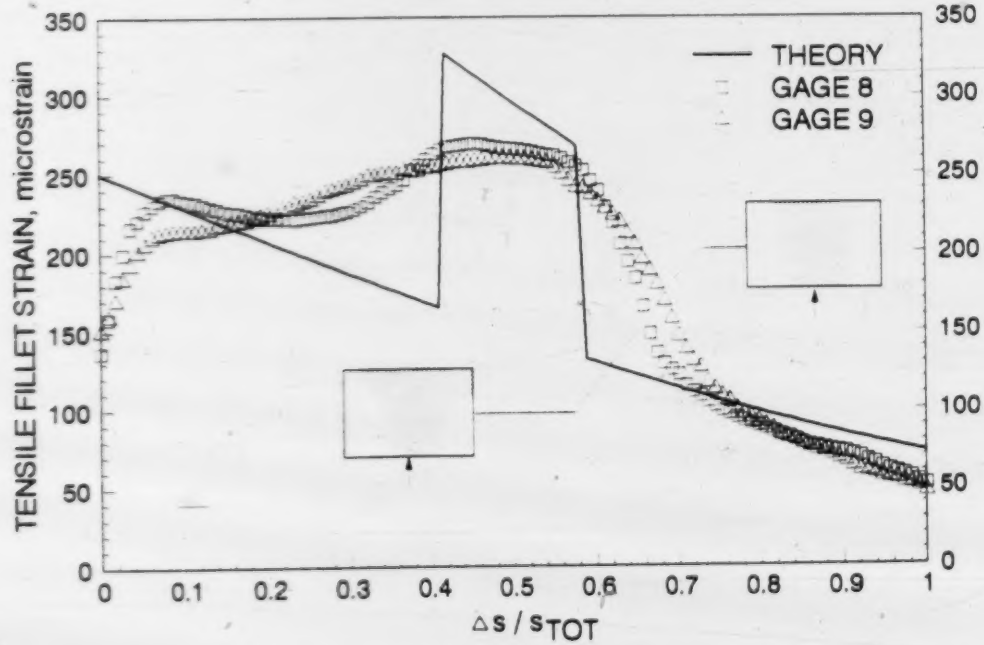

Figure 5.21 - Measured Variation of Strain Along the Line of Contact and Contact Patterns for Gages 8 and 9, Torque = 827 Nm

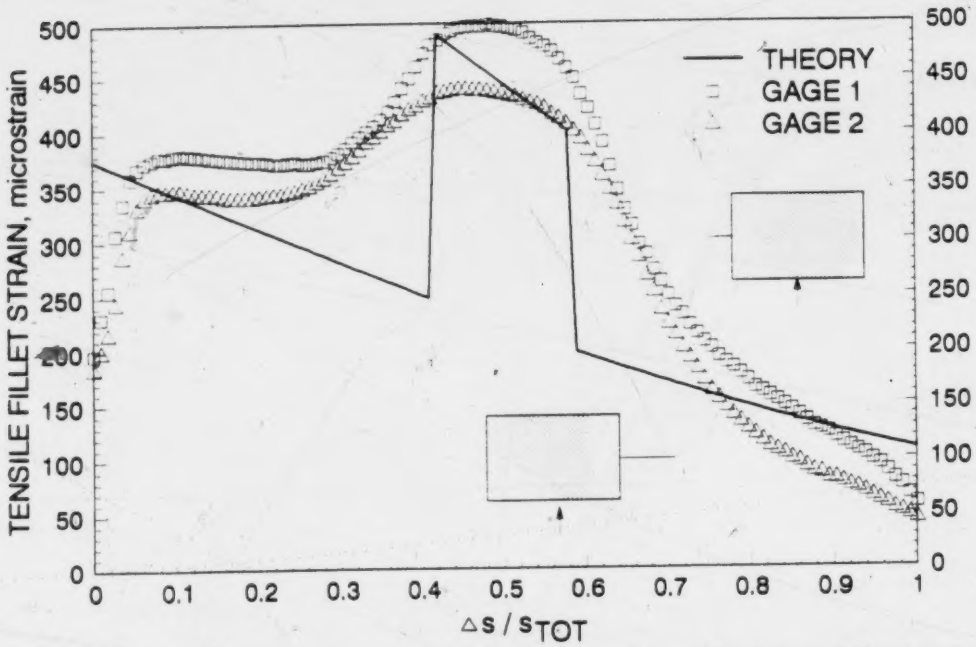

Figure 5.22 - Measured Variation of Strain Along the Line of Contact and Contact Patterns for Gages 1 and 2, Torque = 1241 Nm

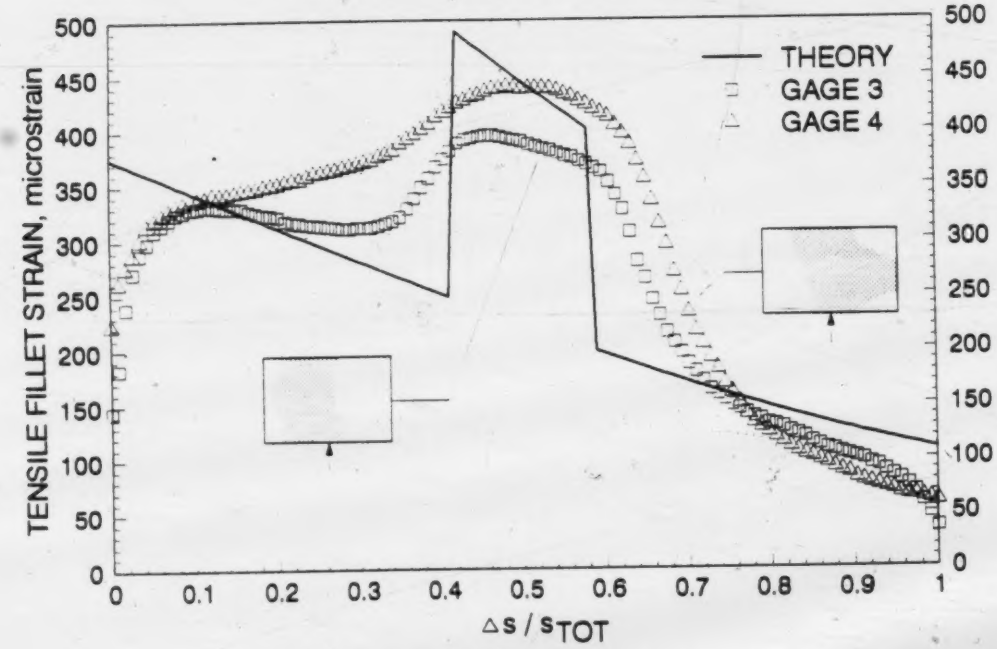

Figure 5.23 - Measured Variation of Strain Along the Line of Contact and Contact Patterns for Gages 3 and 4, Torque = 1241 Nm

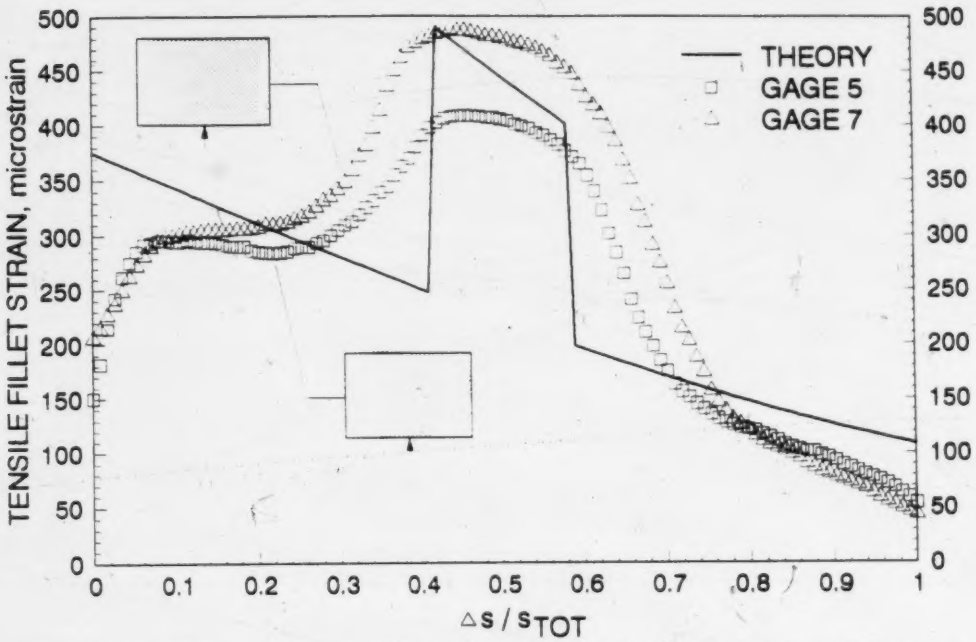

Figure 5.24 - Measured Variation of Strain Along the Line of Contact and Contact Patterns for Gages 5 and 7, Torque = 1241 Nm

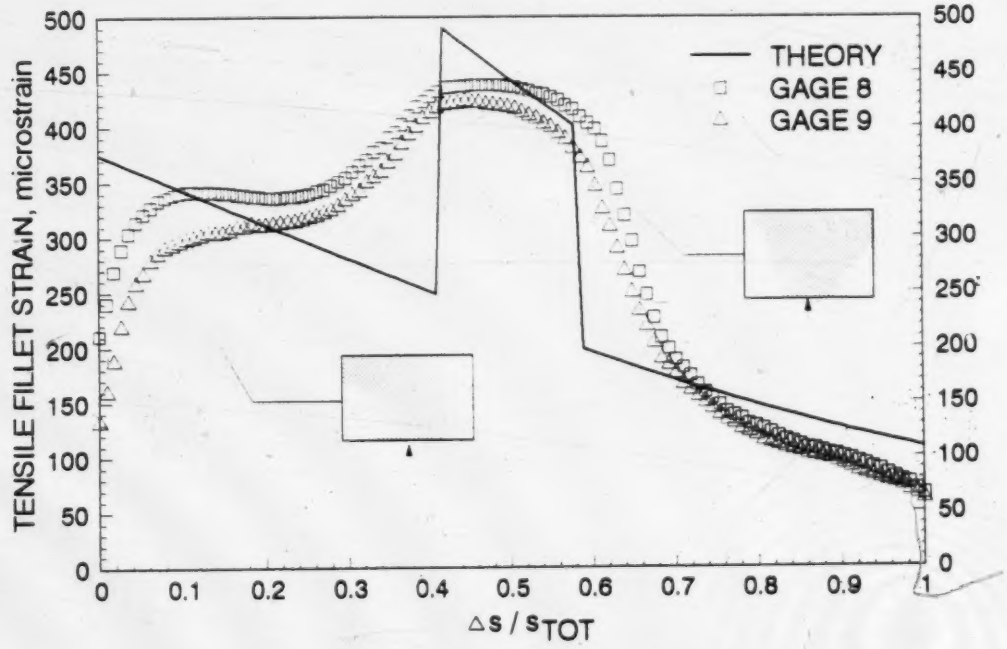

Figure 5.25 - Measured Variation of Strain Along the Line of Contact and Contact Patterns for Gages 8 and 9, Torque = 1241 Nm

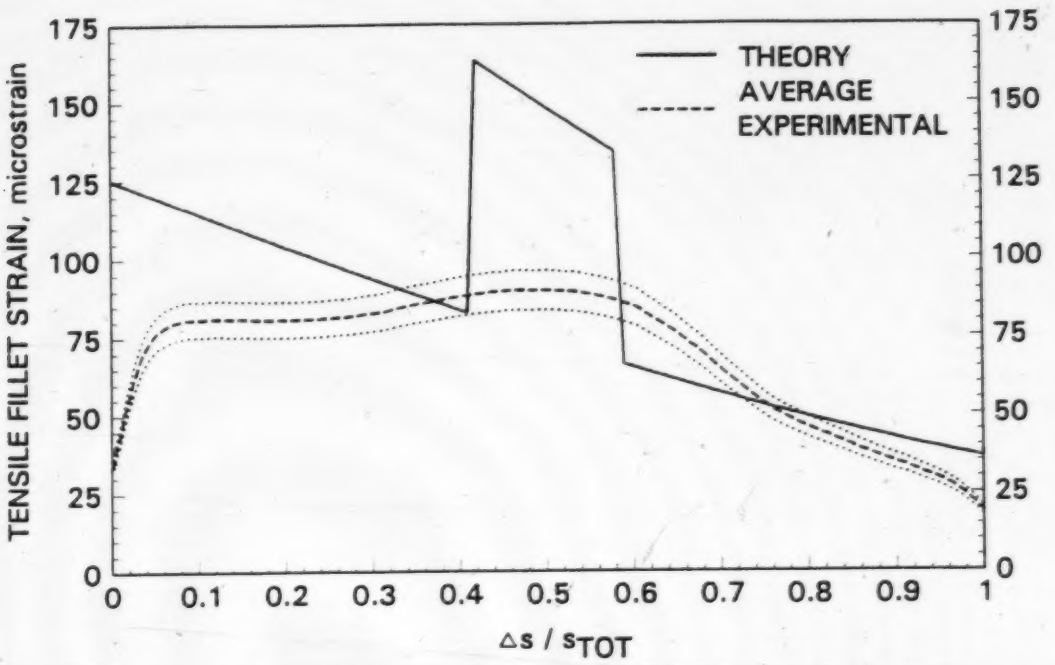

Figure 5.26 - Measured Variation of Strain Along the Line of Contact on 8 Module Spur Gears: Composite Data, Torque = 413 Nm

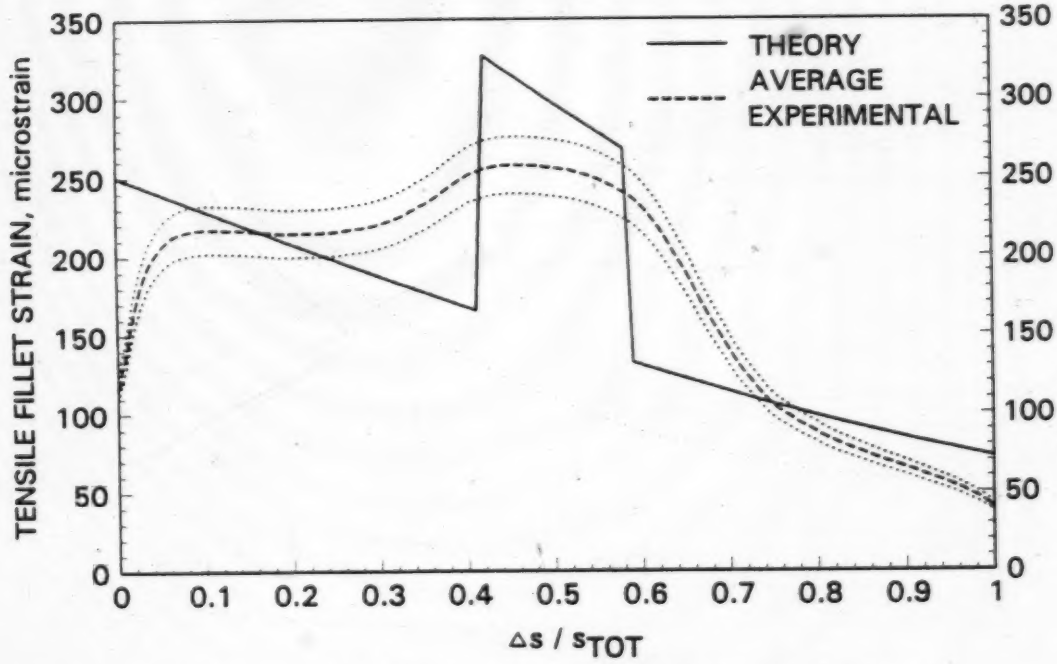

Figure 5.27 - Measured Variation of Strain Along the Line of Contact on 8 Module Spur Gears: Composite Data, Torque = 827 Nm

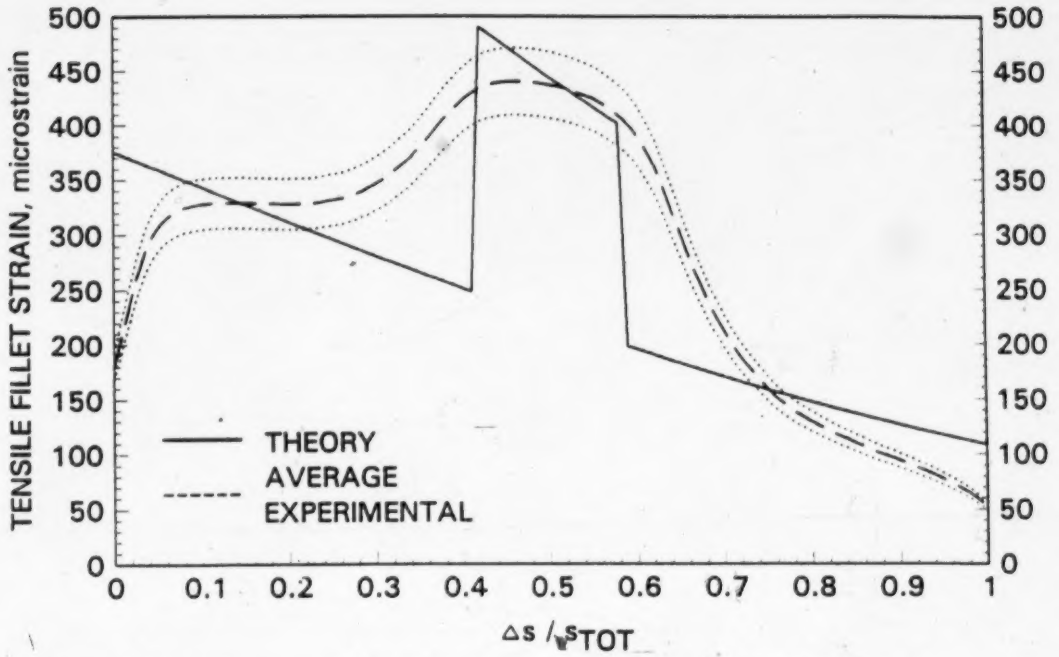

Figure 5.28 - Measured Variation of Strain Along the Line of Contact on 8 Module Spur Gears: Composite Data, Torque = 1241 Nm

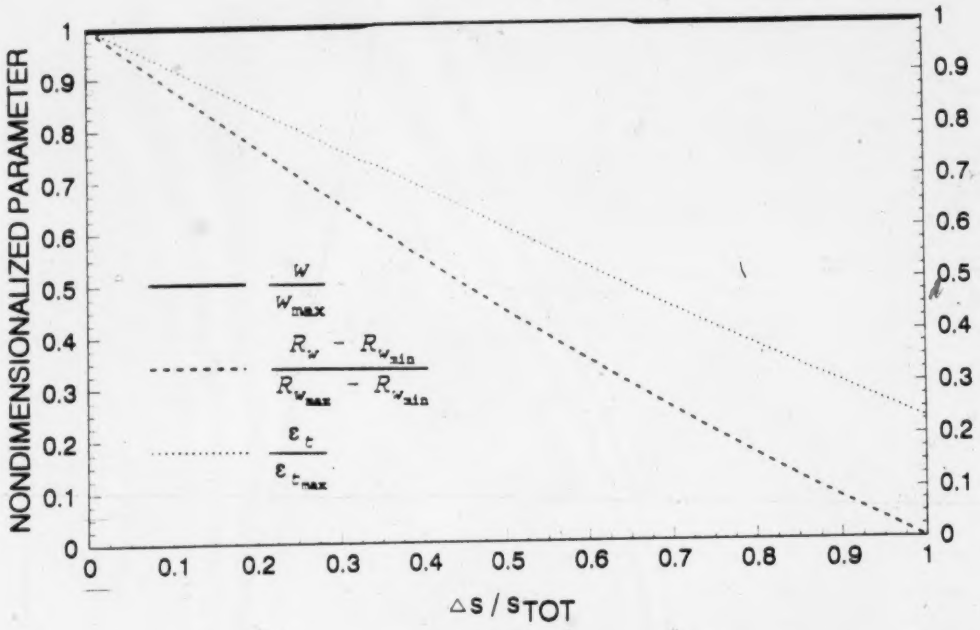

Figure 5.29 - Theoretical Normalized Tensile Fillet Strain, Load Intensity, and Load Radius Variation, 6 Module Helical Gears, z/F=1.0

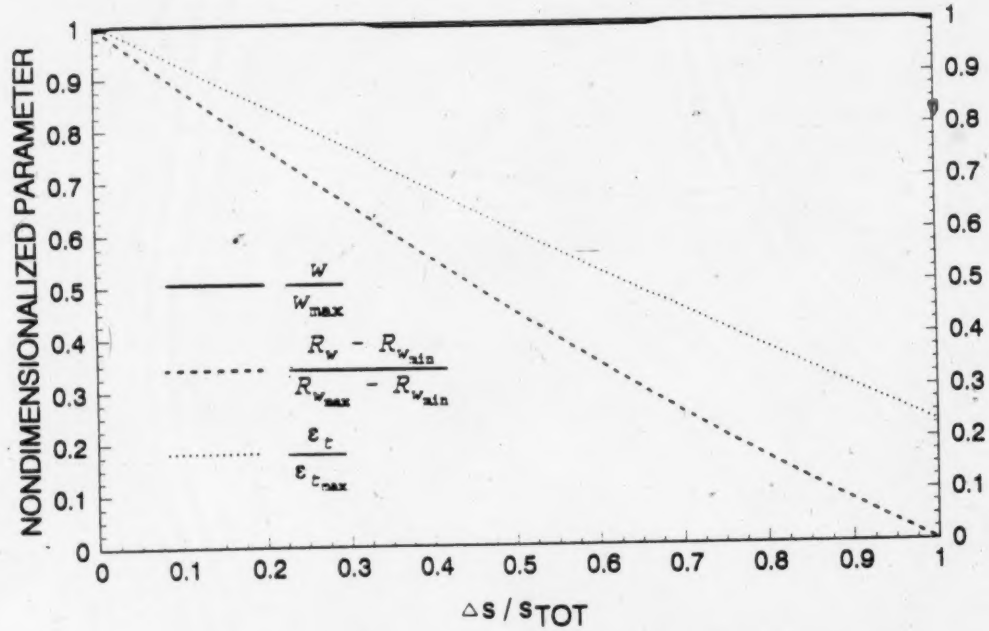

Figure 5.30 - Theoretical Normalized Tensile Fillet Strain, Load Intensity, and Load Radius Variation, 6 Module Helical Gears, z/F=0.5

line located in the z/F = 1.0 transverse plane for the 6 module helical gears, H1 and H2. The tensile fillet strain, load intensity, and load radius have been normalized following the definitions used in Figures 5.3 and 5.4. The variation of normalized load radius is non-linear and has been previously discussed. In order to understand the variation of load intensity with load position along the line of contact, the reader is referred to Figure 2.11.

At the beginning of the meshing cycle $\Delta s/s_{TOT} = 0$, and the contact line passes through T_{1F}. As the contact line passes through T_{1F}, the total contact length will be a maximum and the normalized load intensity a minimum of 0.97 as shown in Figure 5.29. The face contact ratio for gears M1 and M2 is 1.01 so the contact line passing through T_{1F} will intersect the z = 0 transverse plane slightly below Q_0. A second contact line will originate slightly below Q_0' and extend up to the top of the plane of contact. A final contact line will originate at Q_F and extend down to the bottom of the plane of contact. The normalized load intensity will remain a minimum until the original contact point approaches Q_F'. As the contact line approaches Q_F', the total contact length decreases to a minimum and the normalized load intensity increases to 1.0. The normalized load intensity will remain equal to unity until the contact point approaches Q_F. By the time the contact point reaches Q_F, the normalized load intensity will have decreased to a minimum of 0.97. It should be apparent that with such limited variation of the load intensity through the meshing cycle that the value of the normalized tensile fillet strain will be largely controlled by the normalized load radius. This is in fact the case as shown in Figure 5.29 in that the increase in load intensity between z/F = 0.35 and z/F = 0.65 has a limited affect on the normalized fillet strain, and that the maximum normalized fillet strain occurs when the normalized radius is a maximum.

Figures 5.30 and 5.31 show the variation of normalized tensile fillet strain, load intensity, and load radius for the 6 m helical gears in the z/F = 0.5 and z/F = 0.0 transverse planes. In each of these planes, the relationship between contact point position along the path of contact and the total contact length will be different resulting in the

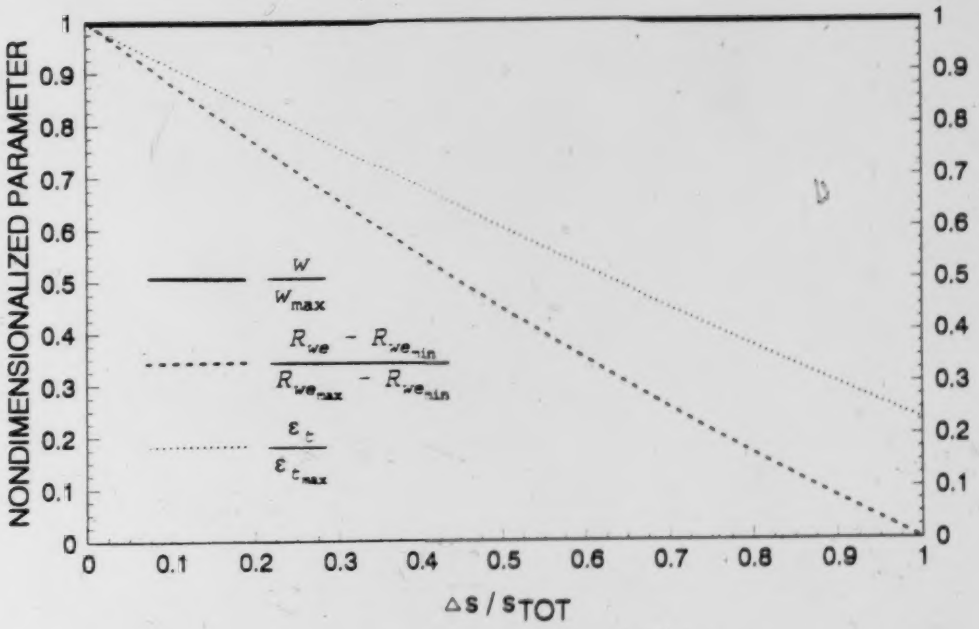

Figure 5.31 - Theoretical Normalized Tensile Fillet Strain, Load Intensity, and Load Radius Variation, 6 Module Helical Gears, z/F=0.0

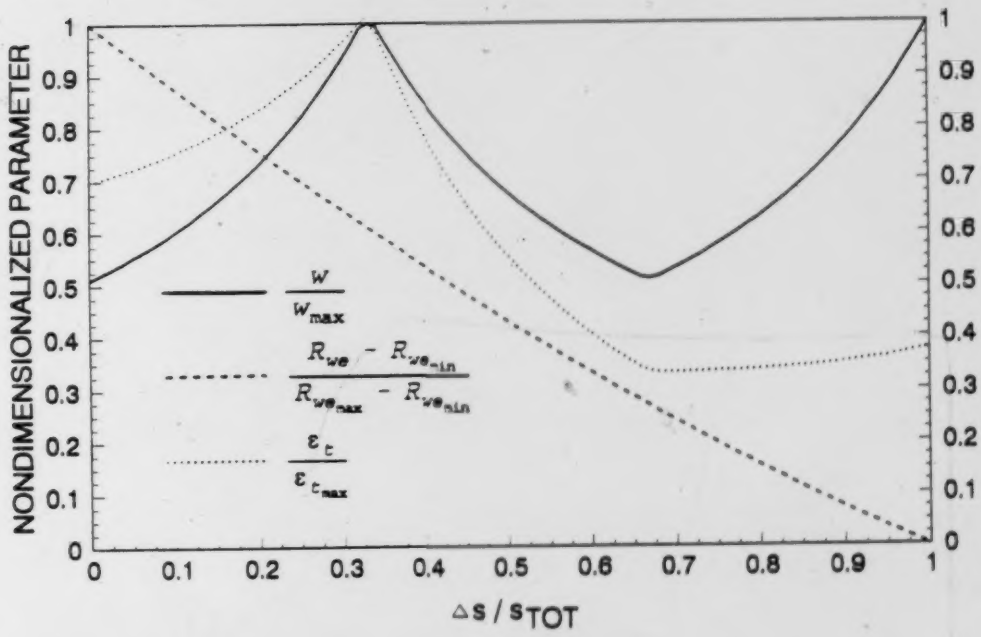

Figure 5.32 - Theoretical Normalized Tensile Fillet Strain, Load Intensity, and Load Radius Variation, 8 Module Helical Gears, z/F=1.0

normalized load intensity and tensile fillet strain plots shown.

The variation of the normalized tensile fillet strain, load intensity, and load radius for the 8 module helical gears H3 and H4 in the $z = F$ transverse plane is shown in Figure 5.32. The variation of normalized load radius proceeds in a manner as previously discussed. The face contact ratio for these gears is 0.50, and consequently, large changes of normalized load intensity are expected throughout the meshing cycle. Inspection of Figure 5.32 reveals this to be the case with minimum normalized load intensity values occurring at $\Delta s/s_{TOT} = 0$ and $\Delta s/s_{TOT} = 0.67$, and maximum normalized load intensity values occurring at $\Delta s/s_{TOT} = 0.33$ and $\Delta s/s_{TOT} = 1.00$. In the region of $\Delta s/s_{TOT} = 0$ to $\Delta s/s_{TOT} = 0.33$, the normalized load radius is dropping while the normalized load intensity is rising. The normalized load intensity is the dominant parameter, so the normalized tensile fillet strain climbs to its maximum value. Between $\Delta s/s_{TOT} = 0.33$ and $\Delta s/s_{TOT} = 0.66$, both the normalized load radius and intensity fall resulting in a rapid decrease in normalized tensile fillet strain. Finally, for $\Delta s/s_{TOT} > 0.66$ the normalized load intensity rises while the normalized load radius falls resulting in a decrease in normalized tensile fillet strain. The variation of normalized load intensity was calculated for the 8 module helical gears in the $z/F = 0.5$ and $z/F = 0.0$ transverse planes and is shown along with the normalized load radii and tensile fillet strain in Figures 5.33 and 5.34.

5.4.5 Measured Strain Variations for the 6 Module Helical Gears H1 and H2

The variation of strain along the lines of contact for the 6 module helical gears with an applied torque of 413 Nm is shown in Figures 5.35-5.40. Gages 22 and 25-29 were centered on the $z/F = 0.5$ transverse plane while Gage 23 was centered on the $z/F = 0.2$ transverse plane, and Gage 24 was located on the $z/F = 0.35$ transverse plane. The decrease of measured strain values with increasing values of $\Delta s/s_{TOT}$ was consistent with theory, although the strains measured as the instrumented tooth entered and left the meshing region were consistently lower than predicted. The maximum

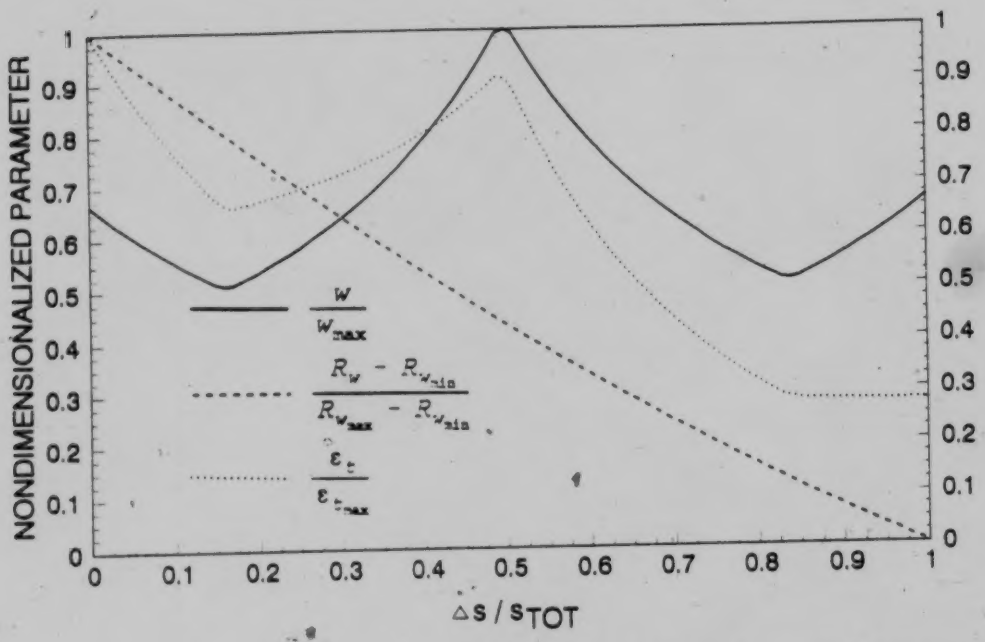

Figure 5.33 - Theoretical Normalized Tensile Fillet Strain, Load Intensity, and Load Radius Variation, 8 Module Helical Gears, z/F=0.5

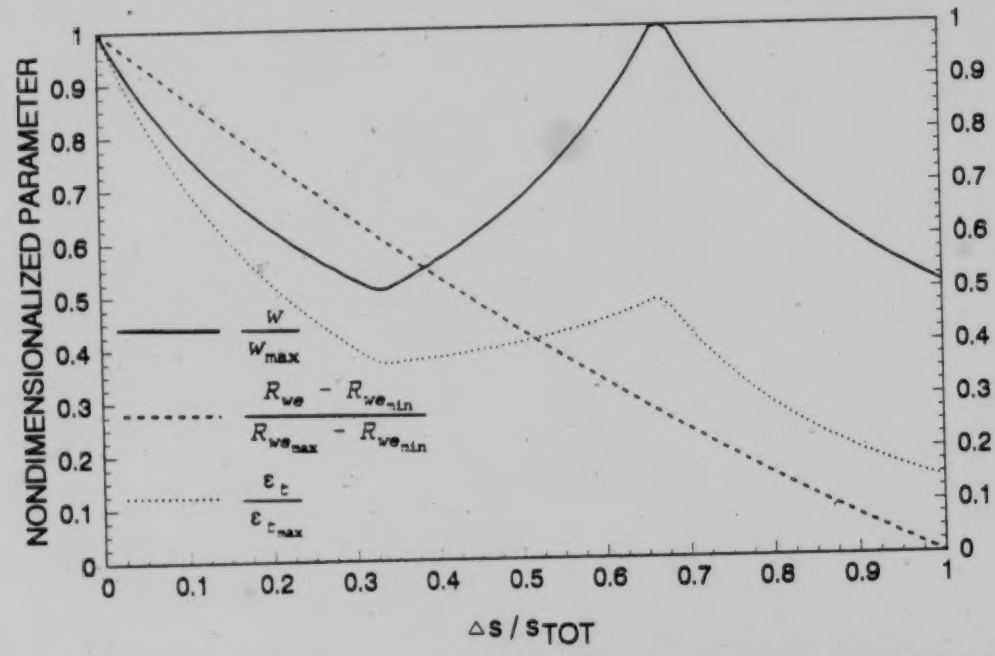

Figure 5.34 - Theoretical Normalized Tensile Fillet Strain, Load Intensity, and Load Radius Variation, 8 Module Helical Gears, z/F=0.0

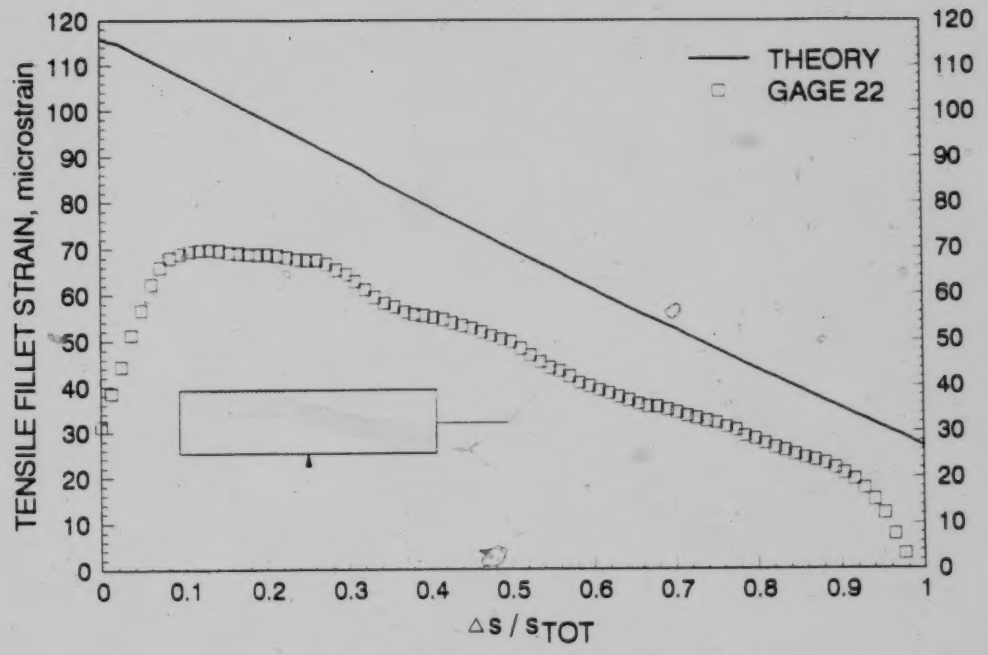

Figure 5.35 - Measured Variation of Strain Along the Line of Contact and Contact Pattern for Gage 22, Torque = 413 Nm, z/F=0.5

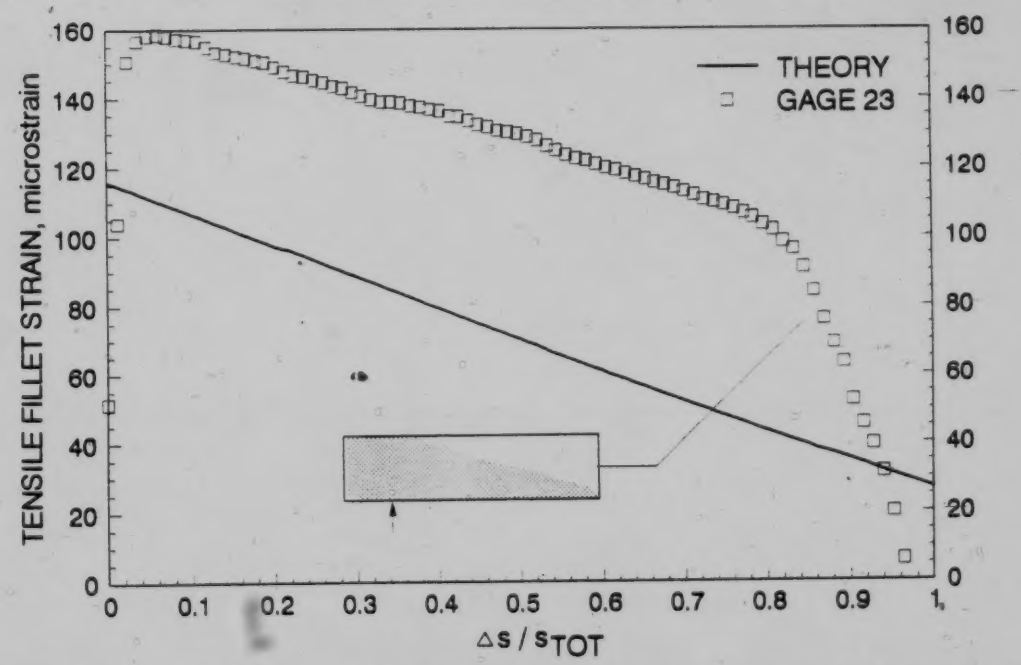

Figure 5.36 - Measured Variation of Strain Along the Line of Contact and Contact Pattern for Gage 23, Torque = 413 Nm, z/F=0.2

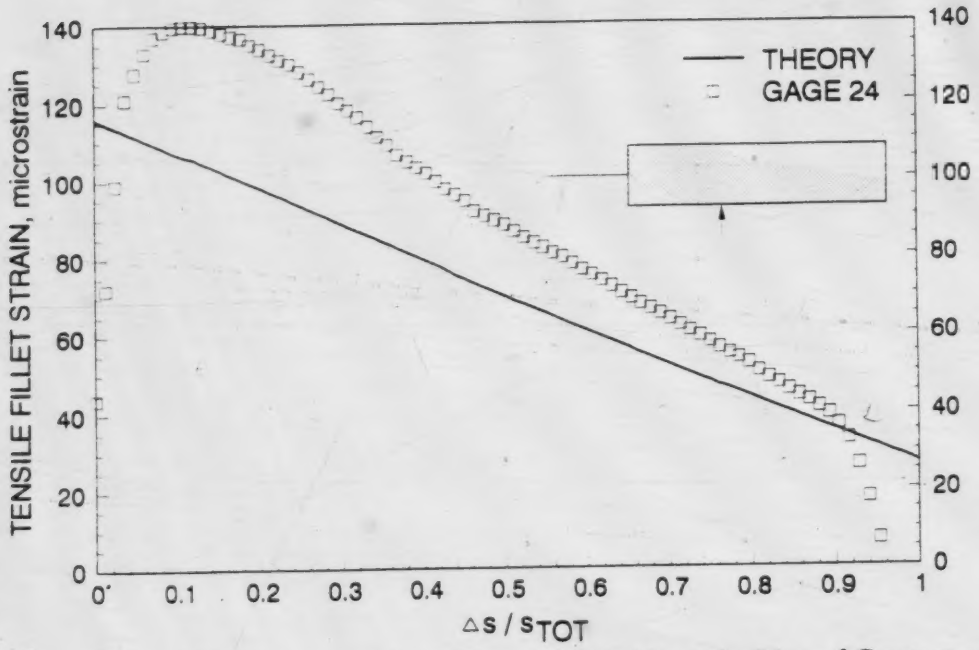

Figure 5.37 - Measured Variation of Strain Along the Line of Contact and Contact Pattern for Gage 24, Torque = 413 Nm, z/F=0.35

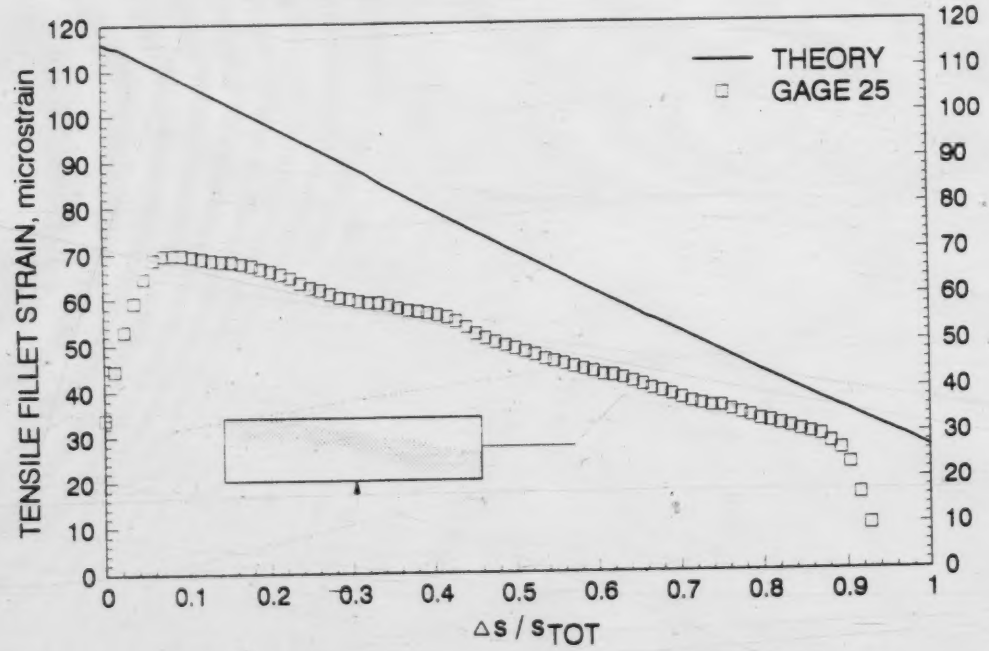

Figure 5.38 - Measured Variation of Strain Along the Line of Contact and Contact Pattern for Gage 25, Torque = 413 Nm, z/F=0.5

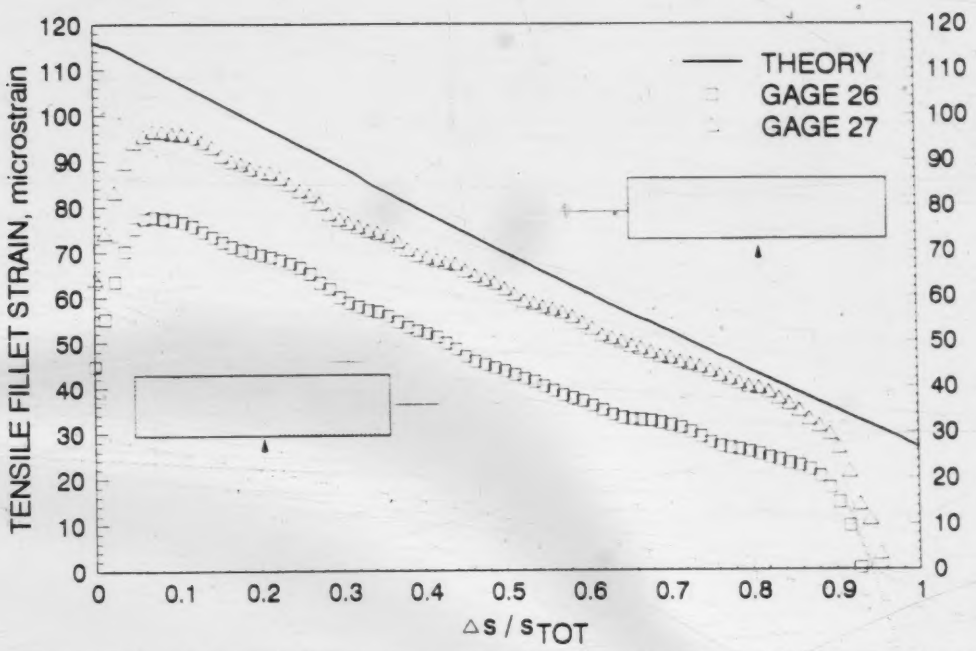

Figure 5.39 - Measured Variation of Strain Along the Line of Contact and Contact Patterns for Gages 26 and 27, Torque = 413 Nm, z/F=0.5

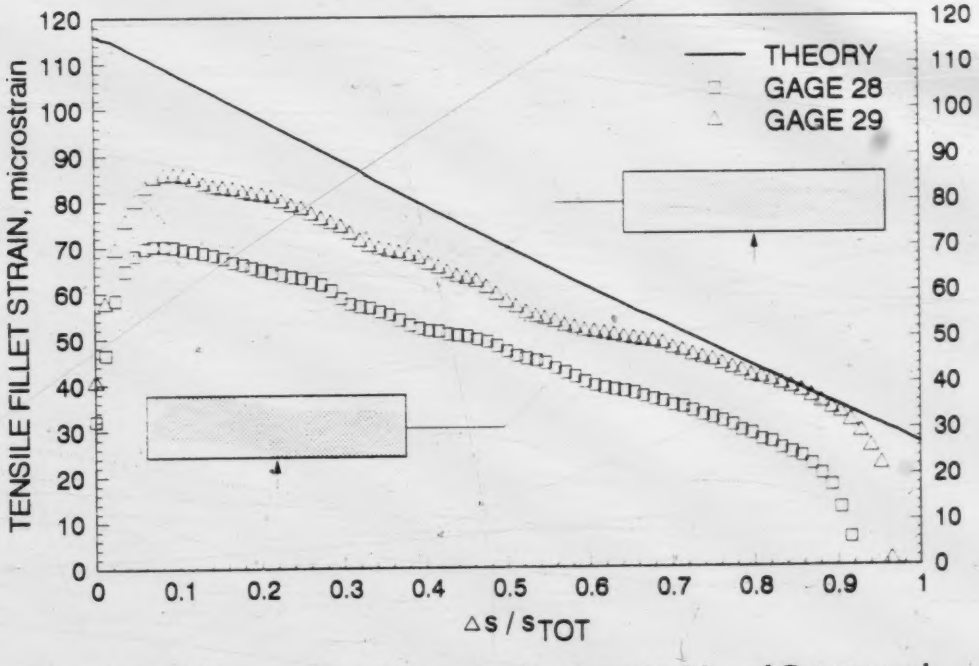

Figure 5.40 - Measured Variation of Strain Along the Line of Contact and Contact Patterns for Gages 28 and 29, Torque = 413 Nm, z/F=0.5

strains were measured when the contact point was close to the tooth tip in the measurement plane. The maximum strains measured in the z/F = 0.5 transverse section were between 60% and 83% of the maximum theoretical values. The maximum measured strains in the z/F = 0.2 and z/F = 0.35 transverse planes were 136% and 120% of the maximum theoretical values, respectively. Inspection of the contact patterns indicated that all of the instrumented locations were experiencing full face contact although some locations, such as Gages 22 and 25 appeared to be less heavily loaded than locations such as Gage 26 and 28. The contact patterns of Gage 23 and 24 are indicative of load concentration towards the z = 0 transverse section. This apparent load concentration is consistent with the larger than expected measured tensile fillet strains shown in Figures 5.36 and 5.37.

When the applied torque was increased to 827 Nm, similar trends of the distribution of tensile fillet strain were observed as is shown in Figures 5.41-5.46. The measured tensile fillet strains decreased with increasing $\Delta s/s_{TOT}$ values in a manner consistent with theory. The maximum measured fillet strains for the gages centered on the z/F = 0.5 transverse plane varied between 54% and 83% of the maximum theoretical value. Contact patterns at these locations were approximately the same shape and size of those patterns produced with an applied torque of 413 Nm. The maximum measured fillet strains for gages centered on the z/F = 0.2 and z/F = 0.35 transverse planes were 125% with 95% of their theoretical maximums. Symmetrical contact patterns were again observed at these locations.

For a maximum applied torque of 1241 Nm, the variation of strain through the meshing process and contact patterns for the eight gage locations are shown in Figures 5.47-5.52. The gages centered on the z/F = 0.5 transverse plane exhibited almost full face contact with maximum measured strains ranging between 66% and 91% of the maximum theoretical strains. The gages centered on the z/F = 0.2 and z/F = 0.35 transverse planes produced maximum tensile fillet strains equal to 130% and 99% of the predicted values. For this applied torque, the contact patterns for these teeth showed that most of the tooth face was carrying load, although the teeth were still more

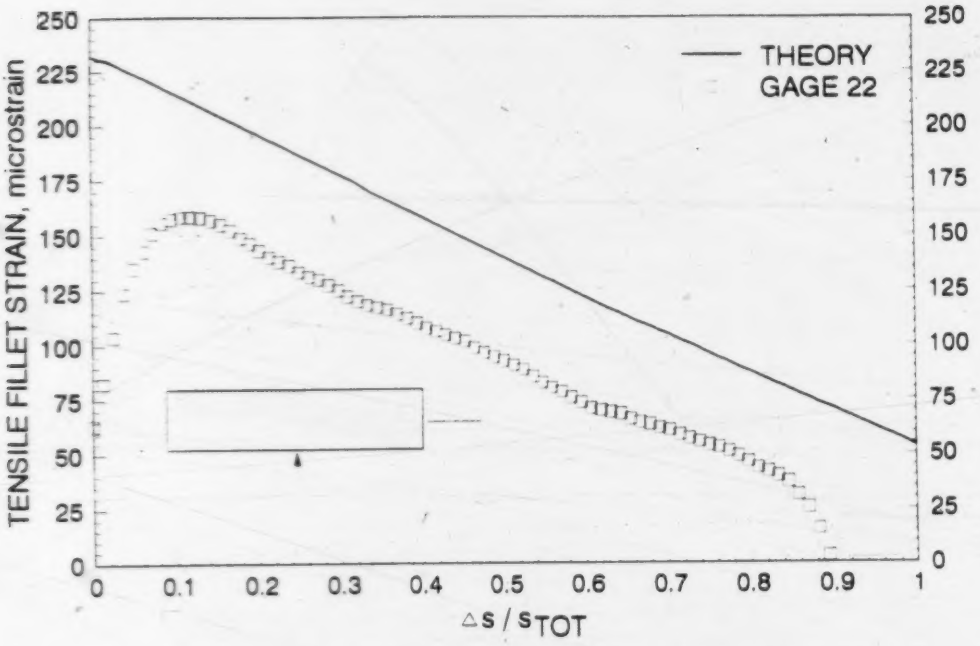

Figure 5.41 - Measured Variation of Strain Along the Line of Contact and Contact Pattern for Gage 22, Torque = 827 Nm, z/F=0.5

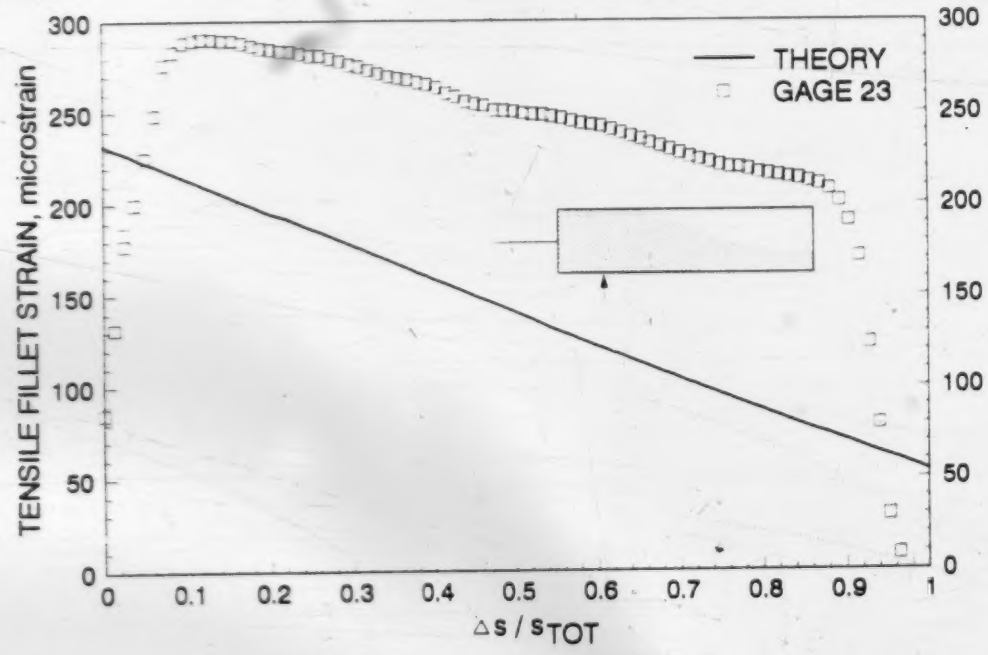

Figure 5.42 - Measured Variation of Strain Along the Line of Contact and Contact Pattern for Gage 23, Torque = 827 Nm, z/F=0.2

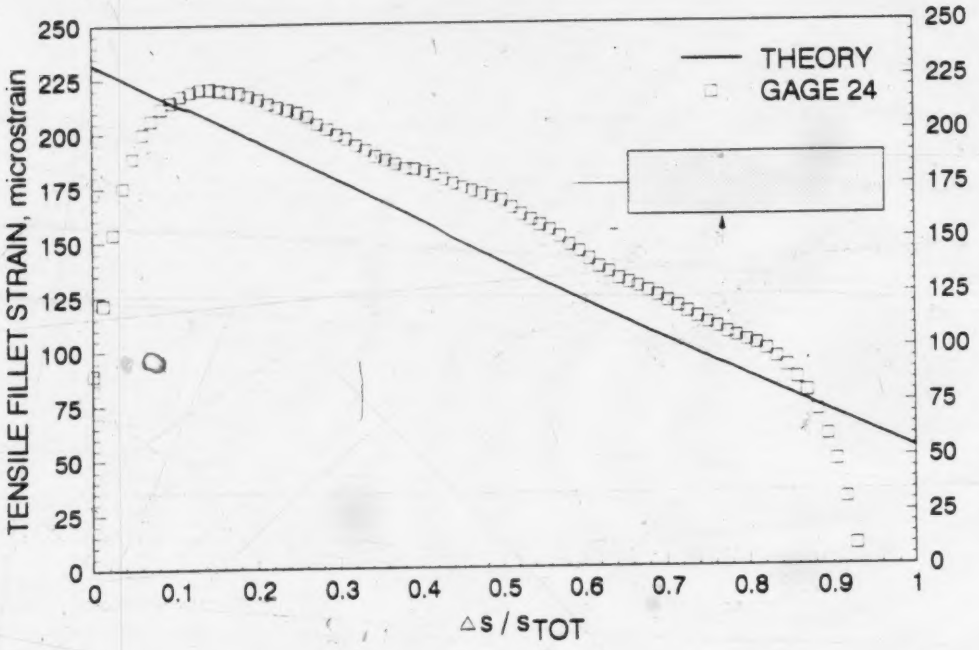

Figure 5.43 - Measured Variation of Strain Along the Line of Contact and Contact Pattern for Gage 24, Torque = 827 Nm, z/F=0.35

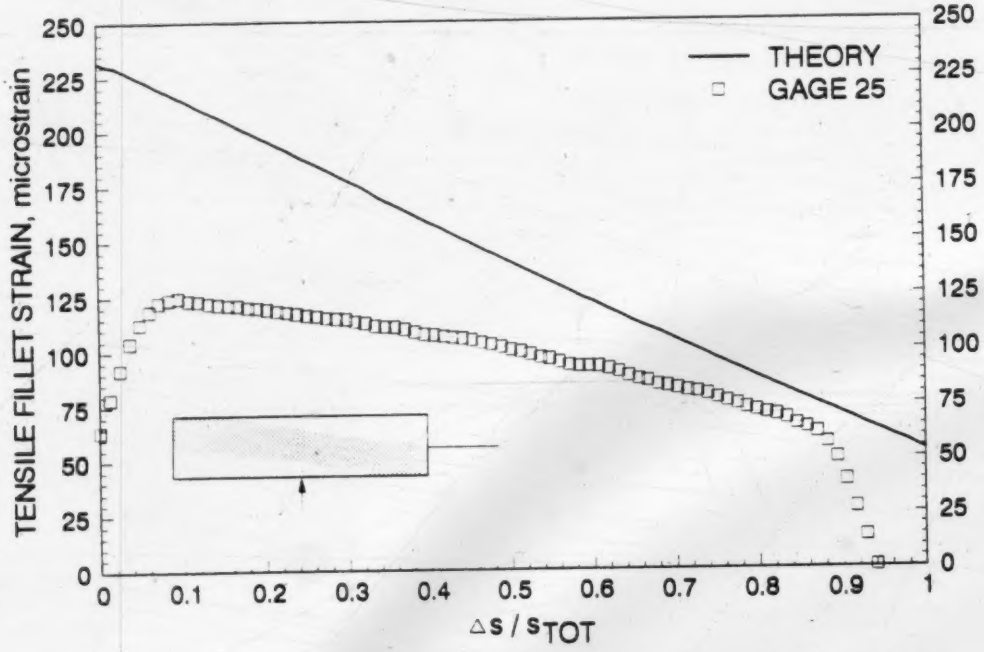

Figure 5.44 - Measured Variation of Strain Along the Line of Contact and Contact Pattern for Gage 25, Torque = 827 Nm, z/F=0.5

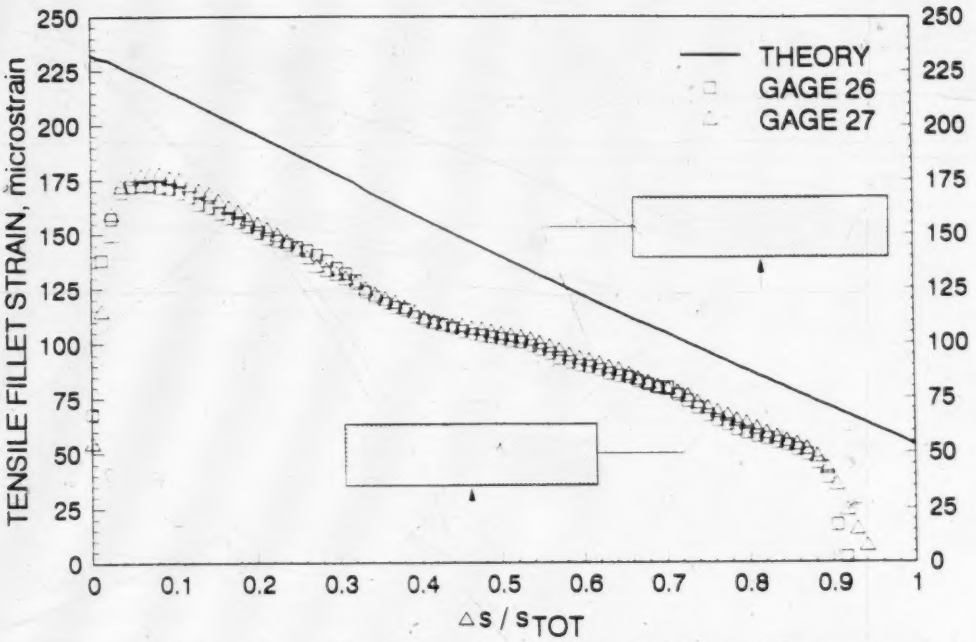

Figure 5.45 - Measured Variation of Strain Along the Line of Contact and Contact Patterns for Gage 26 and 27, Torque = 827 Nm, z/F=0.5

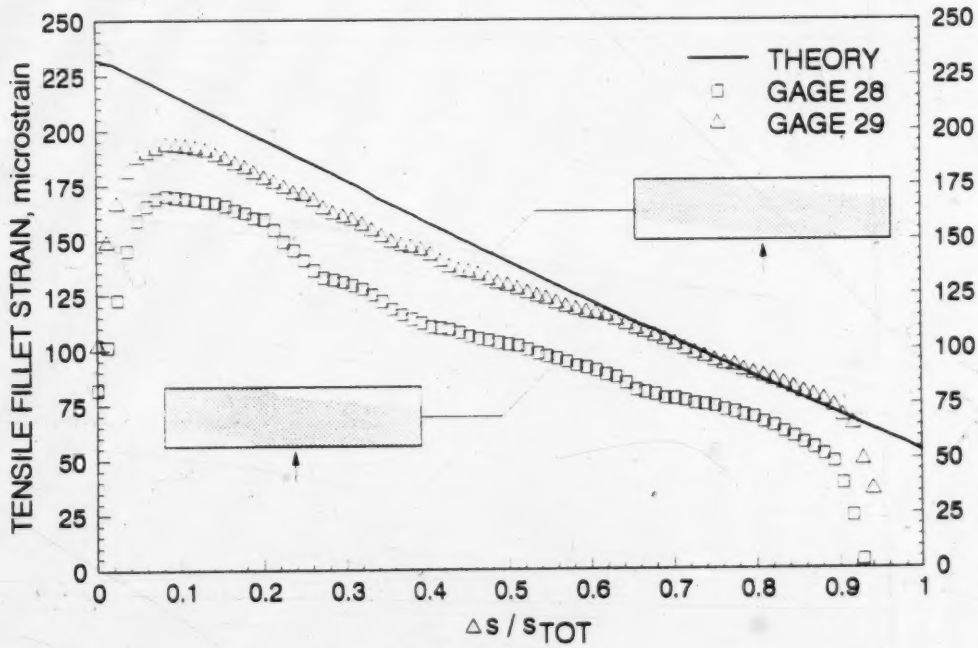

Figure 5.46 - Measured Variation of Strain Along the Line of Contact and Contact Patterns for Gage 28 and 29, Torque = 827 Nm, z/F=0.5

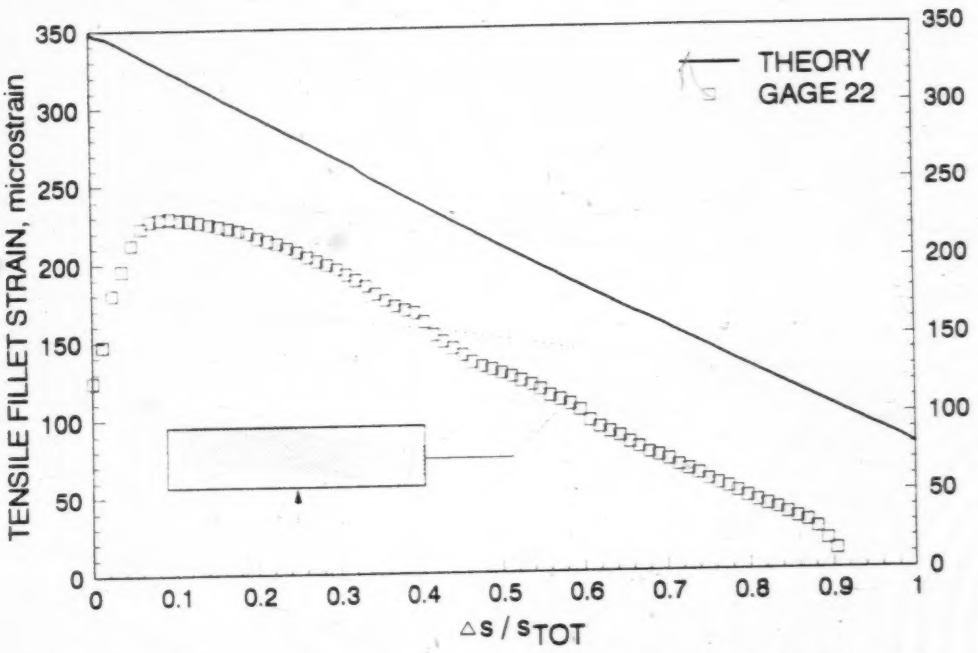

Figure 5.47 - Measured Variation of Strain Along the Line of Contact and Contact Pattern for Gage 22, Torque = 1241 Nm, z/F=0.5

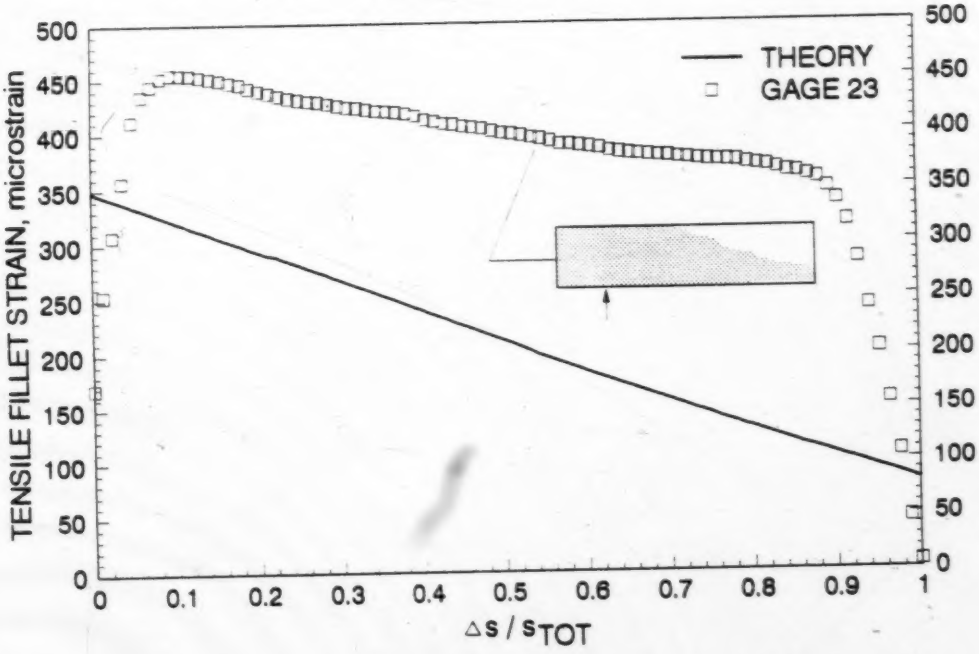

Figure 5.48 - Measured Variation of Strain Along the Line of Contact and Contact Patterns for Gage 23, Torque = 1241 Nm, z/F=0.2

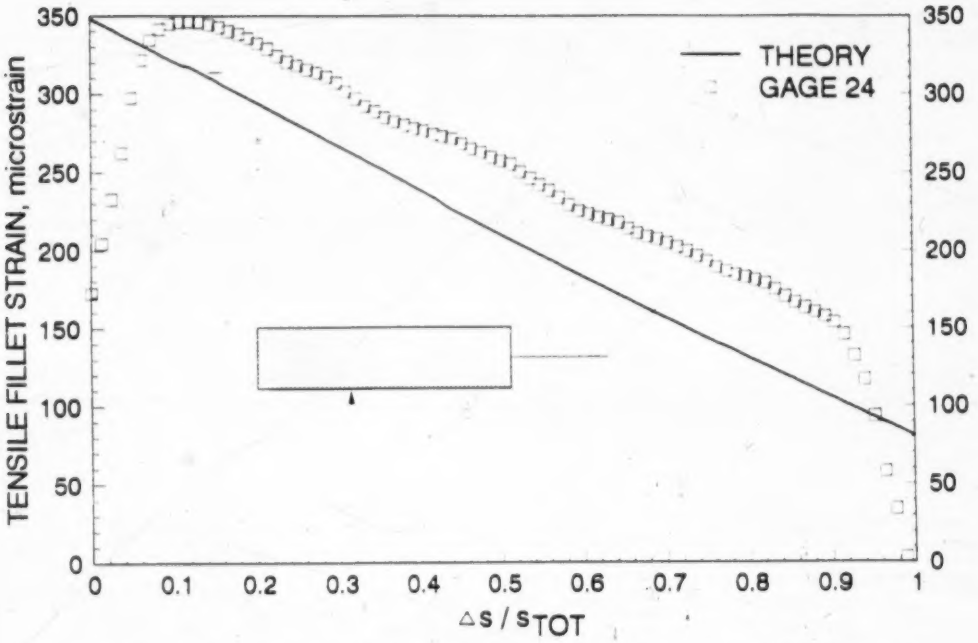

Figure 5.49 - Measured Variation of Strain Along the Line of Contact and Contact Pattern for Gage 24, Torque = 1241 Nm, z/F=0.35

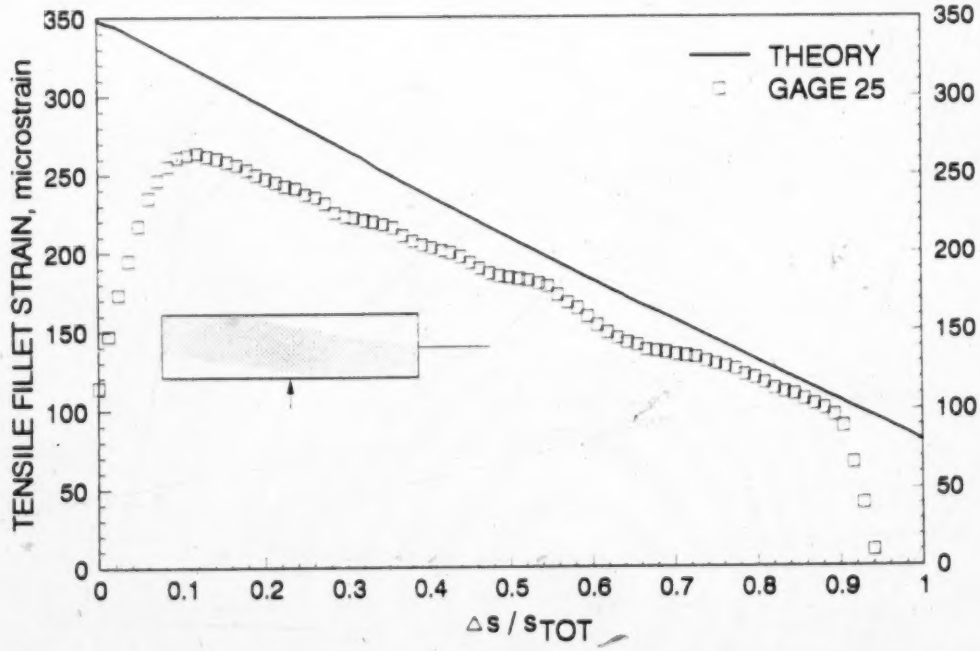

Figure 5.50 - Measured Variation of Strain Along the Line of Contact and Contact Patterns for Gage 25, Torque = 1241 Nm, z/F=0.5

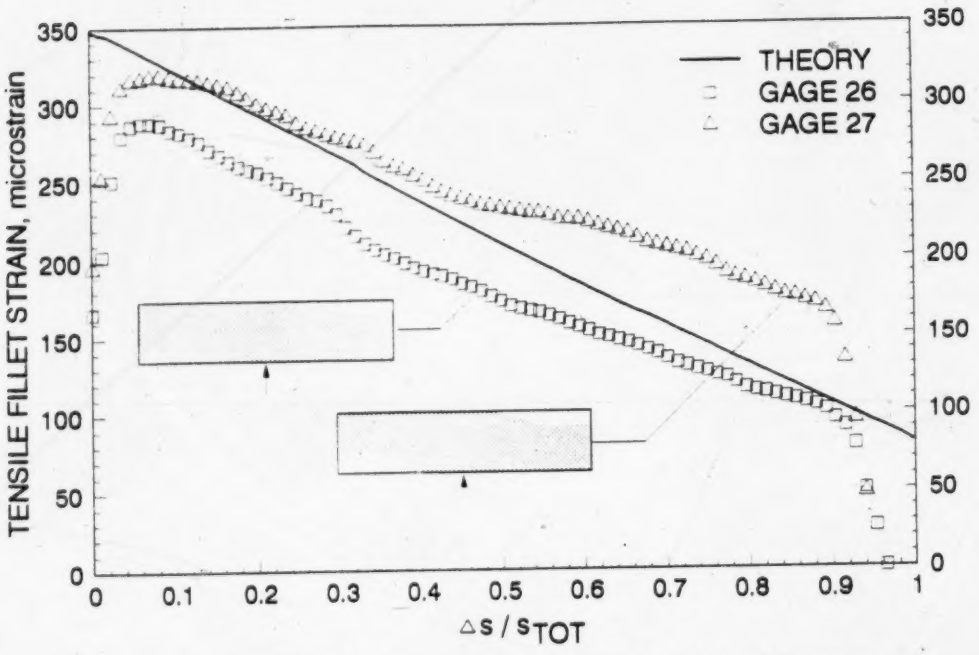

Figure 5.51 - Measured Variation of Strain Along the Line of Contact and Contact Patterns for Gage 26 and 27, Torque = 1241 Nm, z/F=0.5

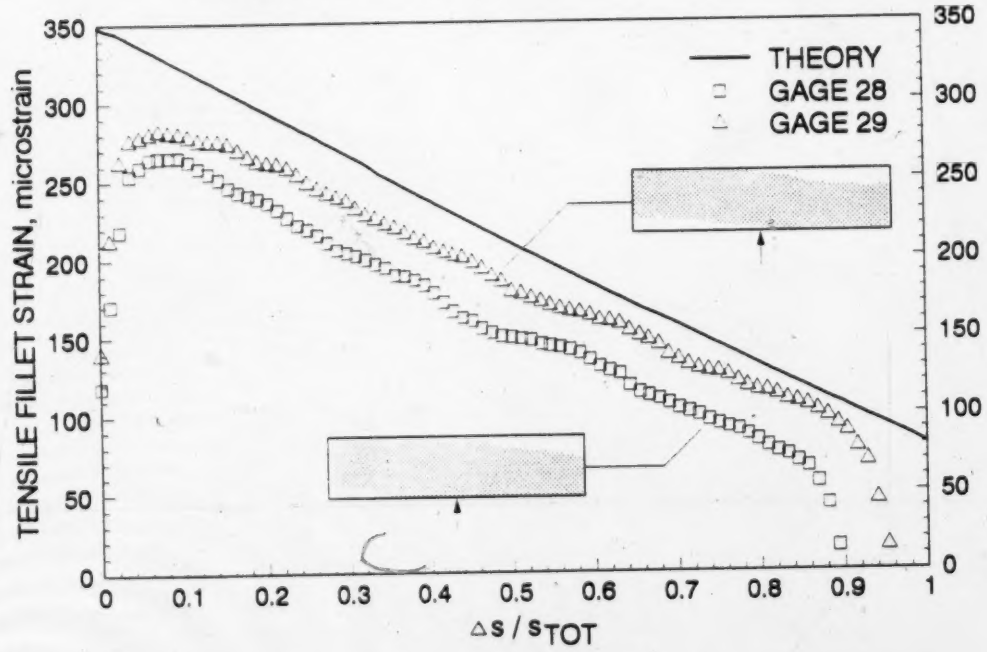

Figure 5.52 - Measured Variation of Strain Along the Line of Contact and Contact Patterns for Gage 28 and 29, Torque = 1241 Nm, z/F=0.5

heavily loaded towards the z/F = 0 transverse plane.

A collection of all of the tensile fillet strain measurements made at the z/F = 0.5 transverse plane location for the 6 module helical gears is shown in Figures 5.53-5.55. These figures show the strain data collected for applied torques of 413 Nm, 827 Nm, and 1241 Nm, respectively. Each of these plots shows the arithmetic average of the results of the six strain gages. From these results, it is apparent that the average experimental strain traces closely approximate the theoretical curves.

5.4.6 Measured Strain Variations for the 8 Module Helical Gears H3 and H4

The measured variation of strain along the line of contact and contact patterns for Gages 13-21 loaded with an applied torque of 413 Nm is shown in Figures 5.56-5.59. All of these strain gages were centered on the z/F = 0.5 transverse section. From these figures, it is apparent that the theory appears to overestimate the tensile fillet strain at the beginning and end of the meshing cycle. This behaviour is consistent with the other gear pairs examined, and is discussed in more detail in Section 5.4.7. The location along the line of contact where the maximum tensile fillet strains were measured is consistent with the location of maximum theoretical tensile fillet strain and maximum load intensity as was shown in Figure 5.33. However, the measured strain was indicated by a zone of maximum tensile fillet strain rather than the distinct maximum fillet strain predicted by theory. The maximum measured fillet strain varied between 76% and 126% of the maximum theoretical strain at $\Delta s/s_{TOT}$ = 0.49. The contact patterns of all of the instrumented teeth exhibited full face width contact. However, indications of light and slightly unsymmetrical loading were present in the contact patterns of the teeth associated with Gages 14 and 18.

When the applied torque was increased to 827 Nm, the variation of tensile fillet strain is as shown in Figures 5.60-5.63. The measured strain traces exhibited, as was noted for an applied torque of 413 Nm, a rapid increase as the teeth entered the meshing region and a rapid decrease as the teeth left the meshing region. The maximum measured fillet strains maintained a nearly constant value for approximately 20% of the total contact length. At the location of maximum stress intensity at z/F = 0.49, the

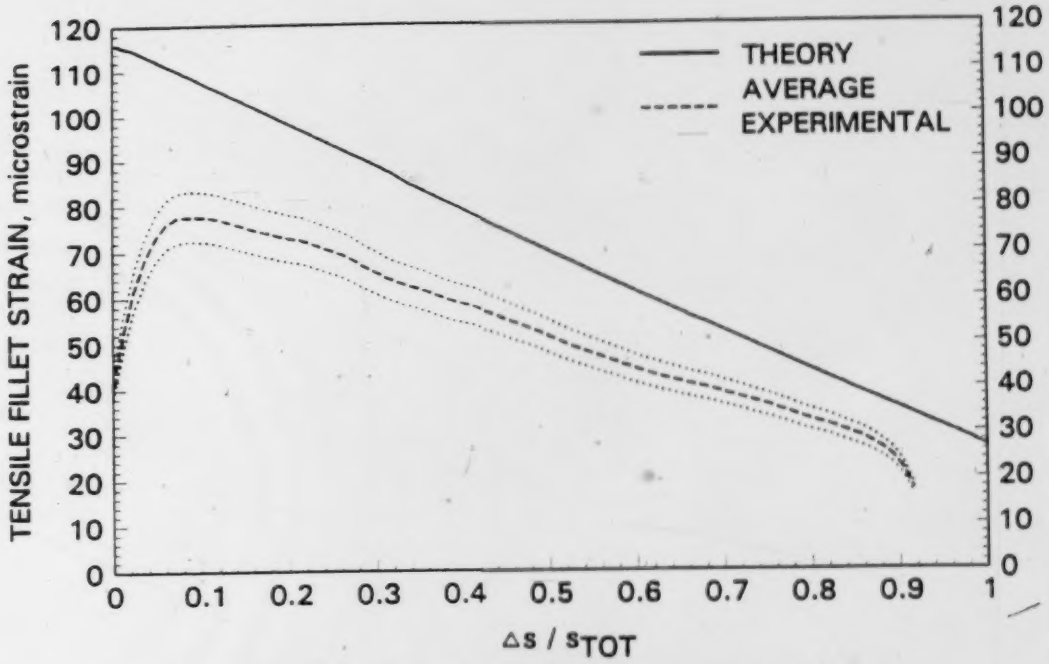

Figure 5.53 - Measured Variation of Strain Along the Line of Contact on 6 Mod. Helical Gears: Composite Data, Torque = 413 Nm, z/F=0.5

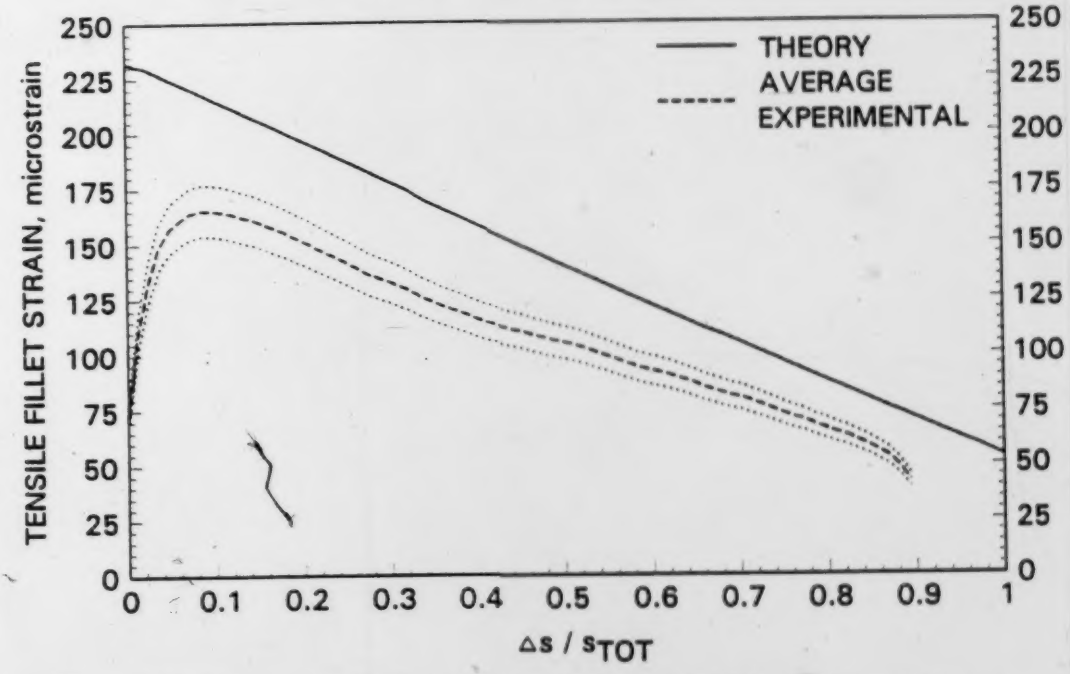

Figure 5.54 - Measured Variation of Strain Along the Line of Contact on 6 Mod. Helical Gears: Composite Data, Torque = 827 Nm, z/F=0.5

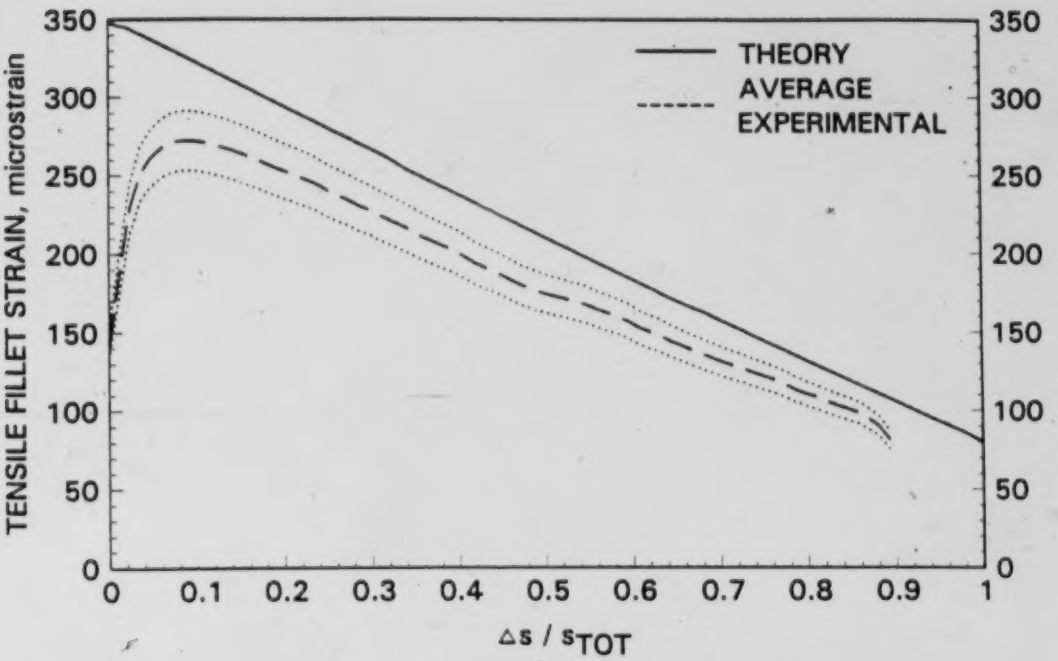

Figure 5.55 - Measured Variation of Strain Along the Line of Contact on 6 Mod. Helical Gears: Composite Data, Torque = 1241 Nm, z/F=0.5

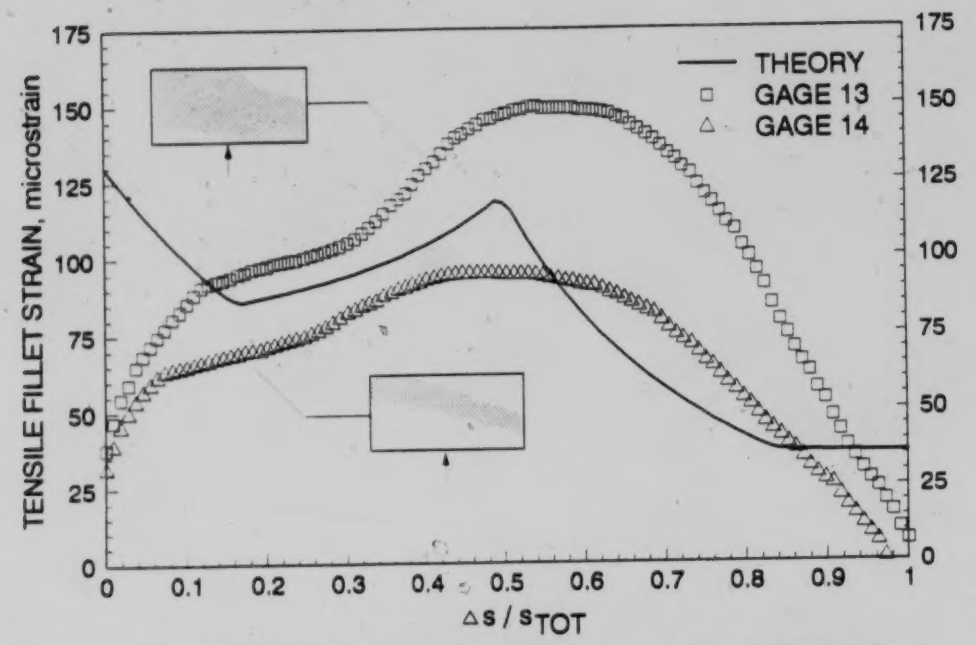

Figure 5.56 - Measured Variation of Strain Along the Line of Contact and Contact Patterns for Gages 13 and 14, Torque = 413 Nm, z/F=0.5

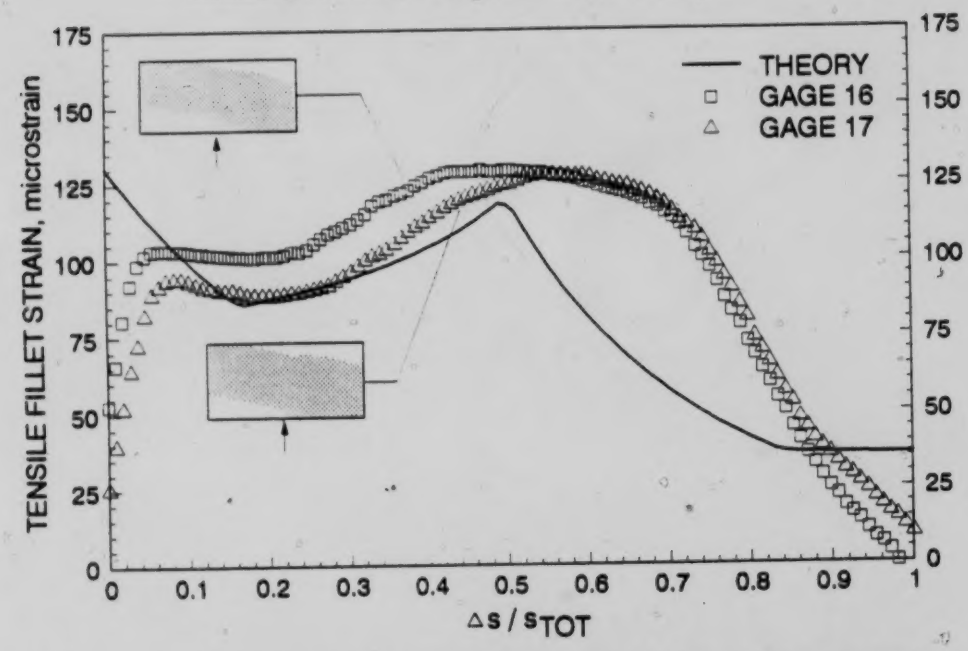

Figure 5.57 - Measured Variation of Strain Along the Line of Contact and Contact Patterns for Gages 16 and 17, Torque = 413 Nm, z/F=0.5

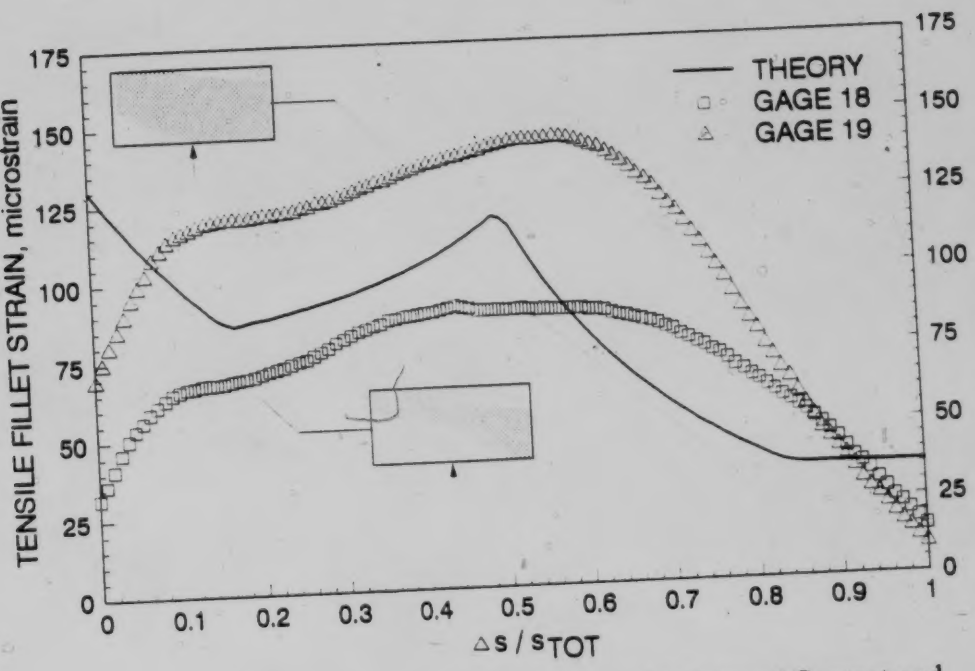

Figure 5.58 - Measured Variation of Strain Along the Line of Contact and Contact Patterns for Gages 18 and 19, Torque = 413 Nm, z/F=0.5

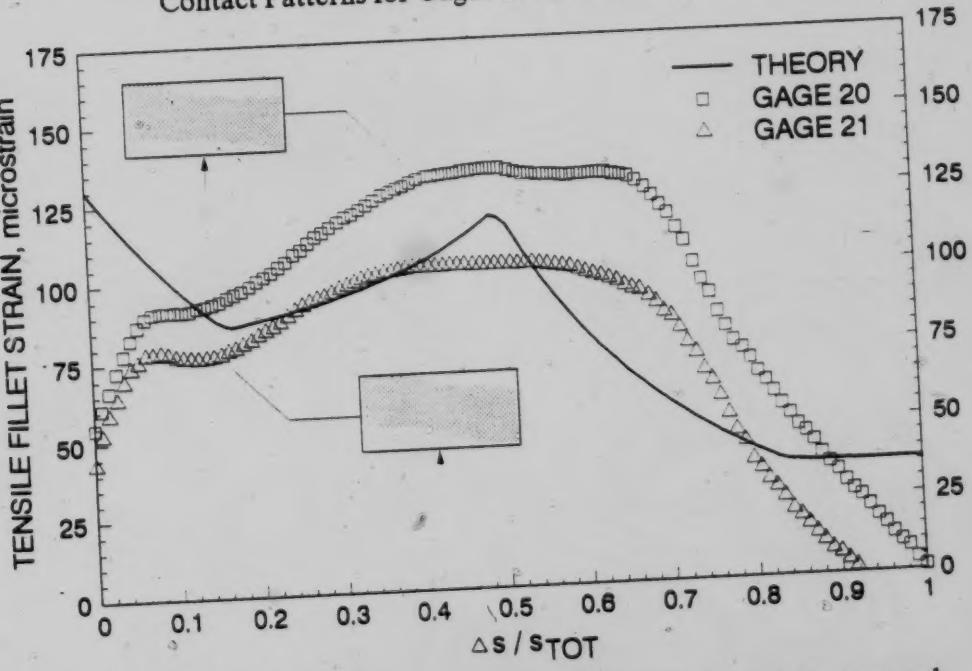

Figure 5.59 - Measured Variation of Strain Along the Line of Contact and Contact Patterns for Gages 20 and 21, Torque = 413 Nm, z/F=0.5

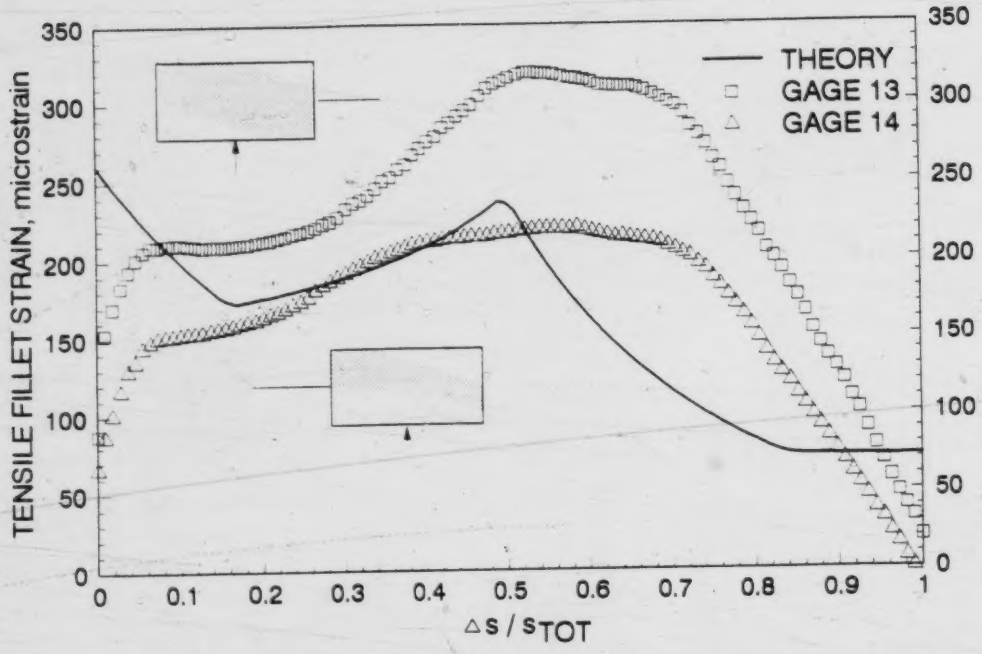

Figure 5.60 - Measured Variation of Strain Along the Line of Contact and Contact Patterns for Gages 13 and 14, Torque = 827 Nm, z/F=0.5

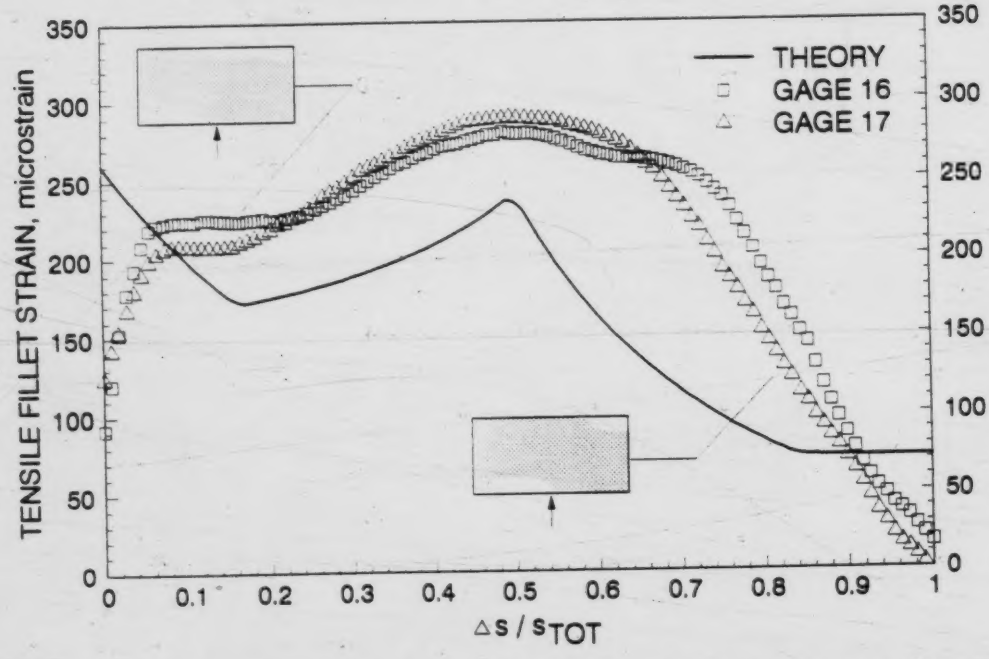

Figure 5.61 - Measured Variation of Strain Along the Line of Contact and Contact Patterns for Gages 16 and 17, Torque = 827 Nm, z/F=0.5

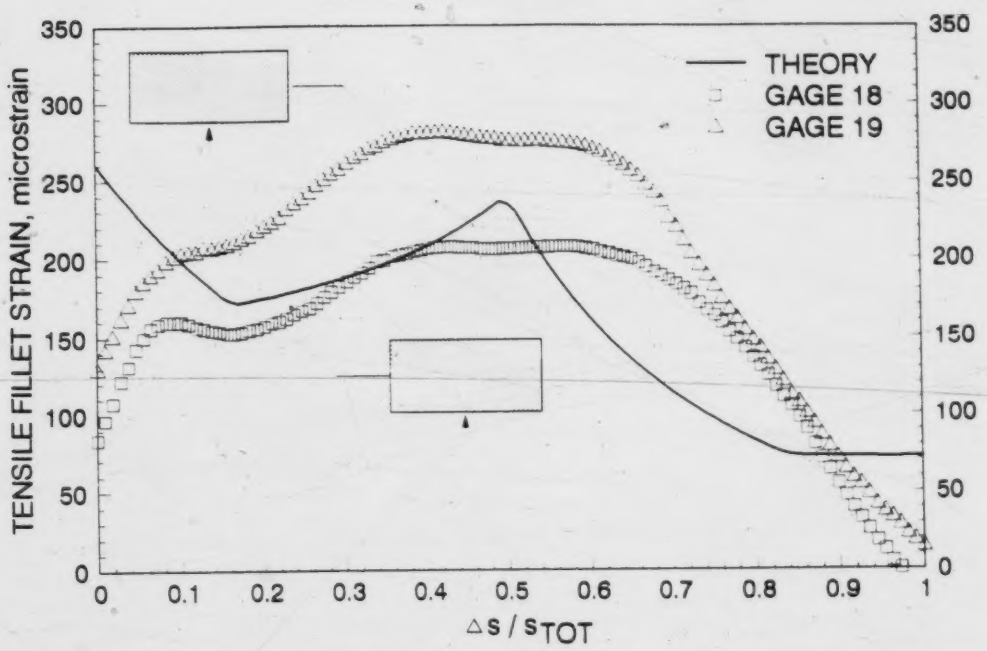

Figure 5.62 - Measured Variation of Strain Along the Line of Contact and Contact Patterns for Gages 18 and 19, Torque = 827 Nm, z/F=0.5

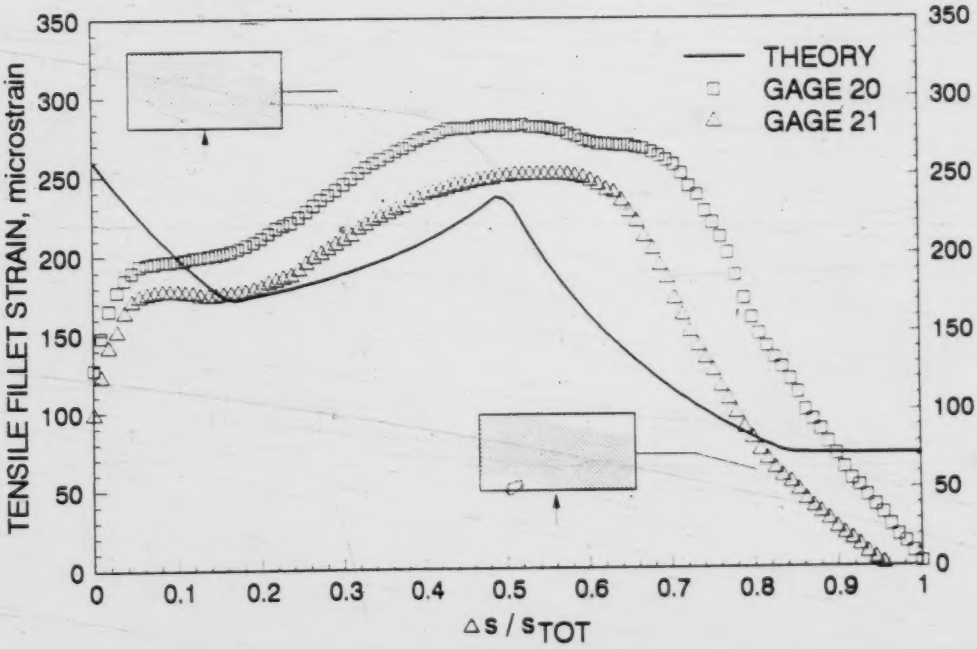

Figure 5.63 - Measured Variation of Strain Along the Line of Contact and Contact Patterns for Gages 20 and 21, Torque = 827 Nm, z/F=0.5

value of the measured fillet strain varied between 88% and 135% of the value of maximum theoretical strain. The contact patterns at all locations were similar to their corresponding contact patterns produced by an applied torque of 413 Nm.

The maximum applied torque of 1241 Nm produced maximum tensile fillet strains which varied between 82% and 128% of the maximum theoretical tensile fillet strains. As shown in Figures 5.64-5.67, the shapes of the strain traces are consistent with their shapes under lower applied torque levels. Load transfer across the entire tooth surface is evident in most of the contact patterns. Figures 5.68-5.70 show the average experimental variation of strain along the line of contact for the three applied torques along with the theoretical curves. From these figures it is apparent that there is reasonable agreement between the average exper imental and theoretical curves except at the beginning and end of the meshing process. It is also apparent that the degree of agreement between the average experimental and theoretical curves is independent of the applied torque to the gear. The 8 module helical gears provided the largest clearances for the mounting of strain gages, and consequently the gages were mounted on sensitive areas of the fillet. This is in contrast to the gages mounted on the 5 module spur gears which were less sensitive at lower applied torque levels as a result of the gages' placement.

5.4.7 Examination of the Differences Between Experimental and Theoretical Tensile 5.4.7 Fillet Strains

In the preceding sections reasonable agreement was found between the measured and predicted tensile fillet strains with the following exceptions:

- measured strains for the 5 module spur gears were substantially less than predicted values, especially for low values of applied torques.
- the theoretical values of tensile fillet strain for teeth entering and leaving the mesh were substantially higher than the measured values.

Hirt [43] measured the tensile fillet strains developed at ten locations along the fillet and root for various load positions. For tests conducted on ten spur gears with differing geometries, he discovered that the stresses present in the gear root varied

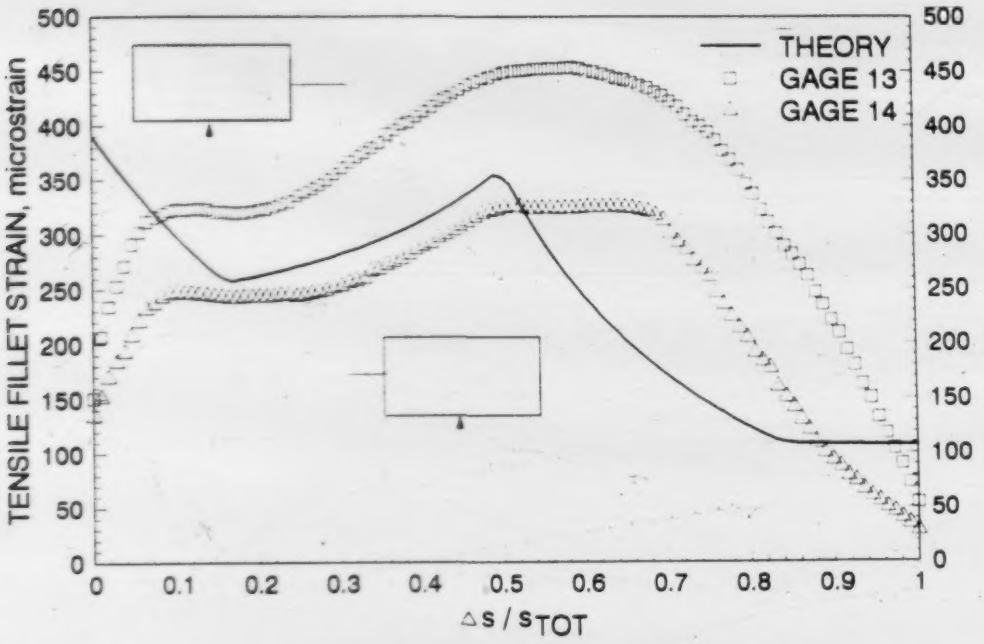

Figure 5.64 - Measured Variation of Strain Along the Line of Contact and Contact Patterns for Gages 13 and 14, Torque = 1241 Nm, z/F=0.5

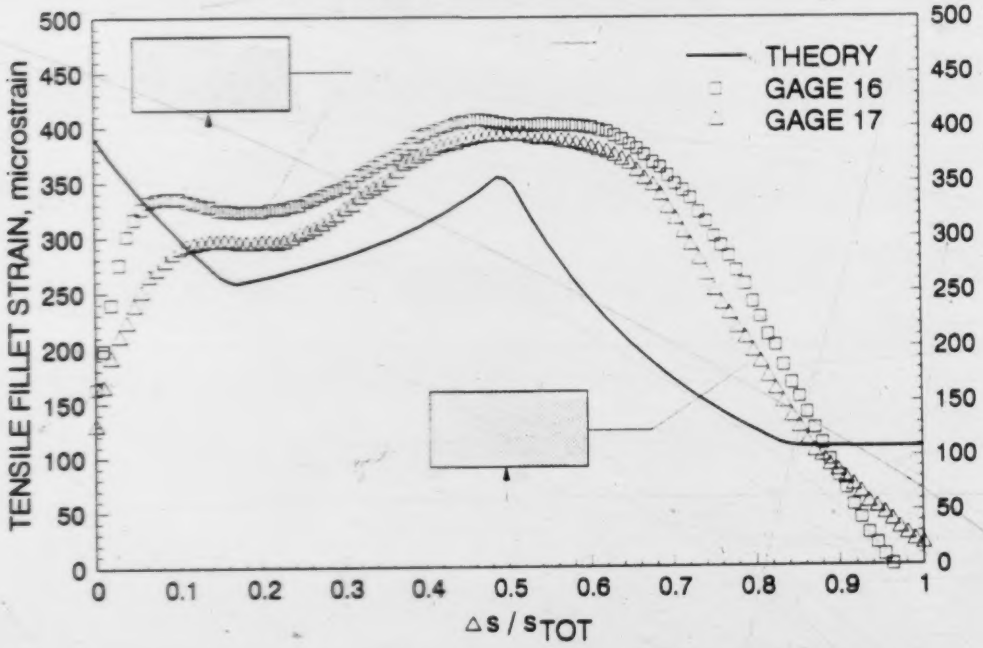

Figure 5.65 - Measured Variation of Strain Along the Line of Contact and Contact Patterns for Gages 16 and 17, Torque = 1241 Nm, z/F=0.5

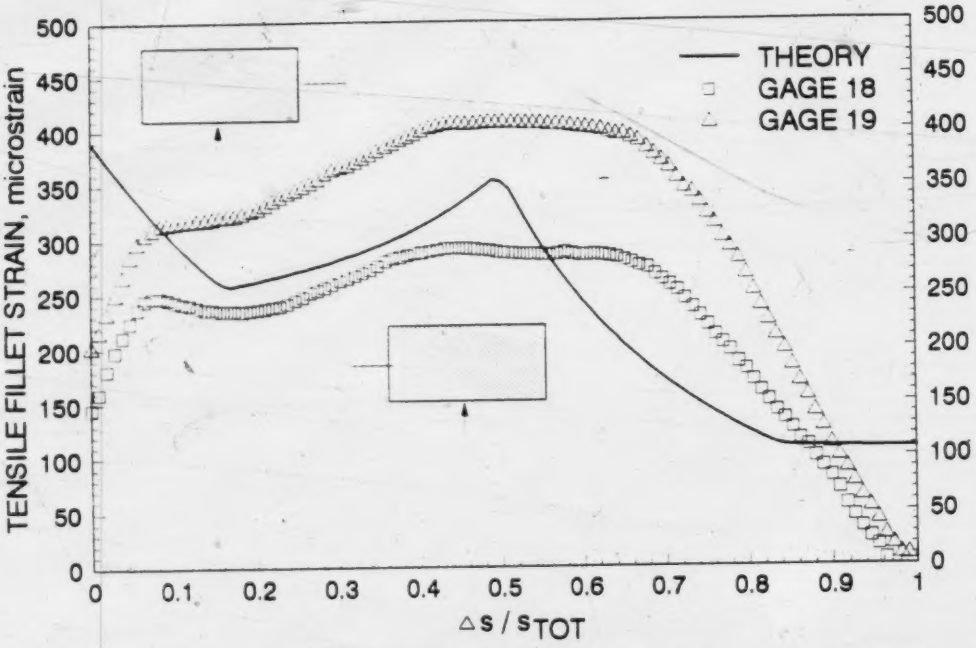

Figure 5.66 - Measured Variation of Strain Along the Line of Contact and Contact Patterns for Gages 18 and 19, Torque = 1241 Nm, z/F=0.5

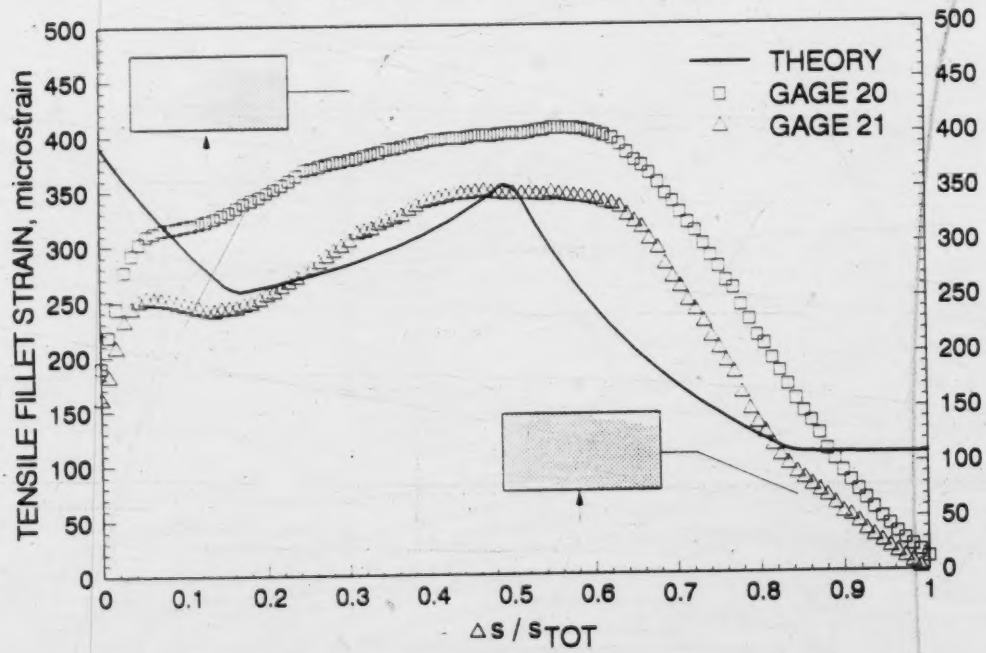

Figure 5.67 - Measured Variation of Strain Along the Line of Contact and Contact Patterns for Gages 20 and 21, Torque = 1241 Nm, z/F=0.5

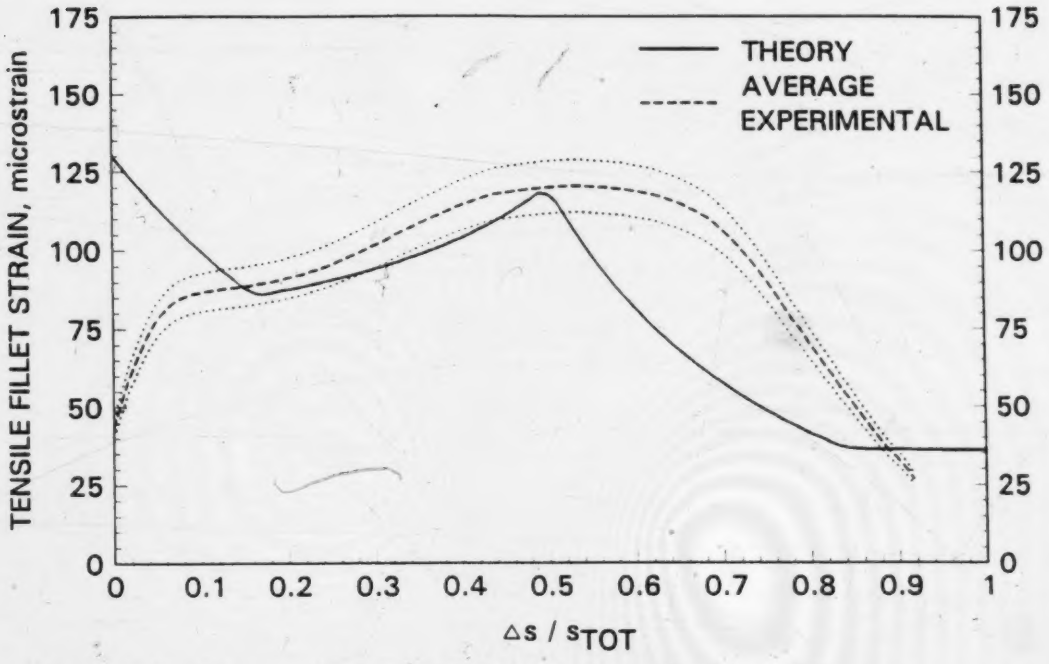

Figure 5.68 - Measured Variation of Strain Along the Line of Contact on 8 Mod. Helical Gears: Composite Data, Torque = 413 Nm, z/F=0.5

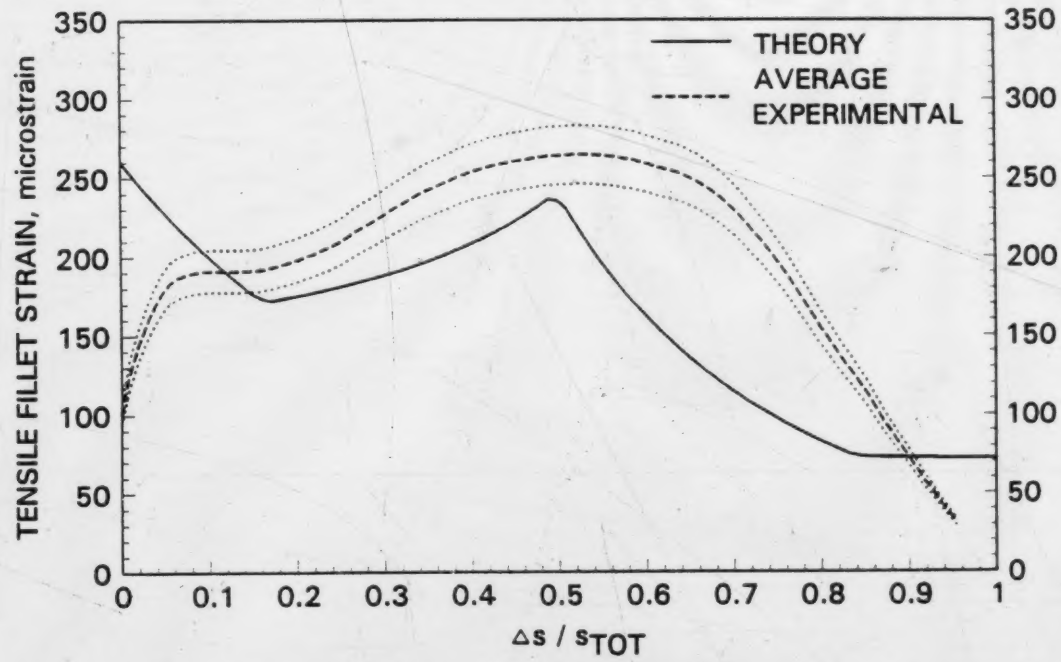

Figure 5.69 - Measured Variation of Strain Along the Line of Contact on 8 Mod. Helical Gears: Composite Data, Torque = 827 Nm, z/F=0.5

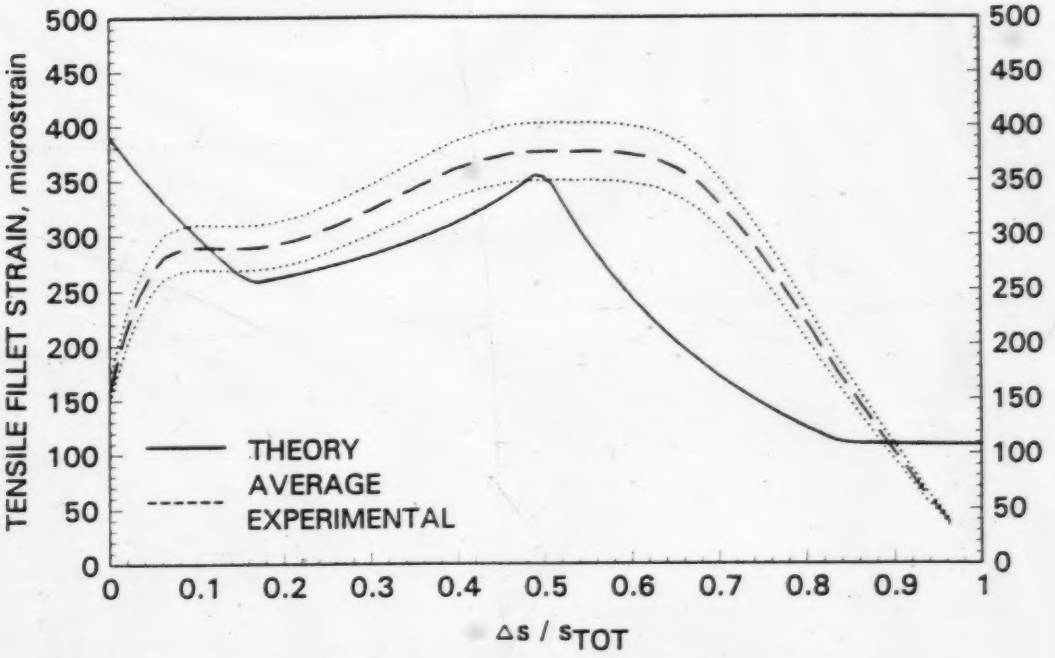

Figure 5.70 - Measured Variation of Strain Along the Line of Contact on 8 Mod. Helical Gears: Composite Data, Torque = 1241 Nm, z/F=0.5

between 14% and 77% of the maximum fillet tensile stress. As previously mentioned, the geometry of the 5 module spur gear combined with geometry of the strain gages used in these locations resulted in portions of the gage grid being bonded to the gear root. Hirst has shown that gages mounted in the root of the gear will experience less strain than gages mounted higher on the fillet for the same loading conditions. Consequently, it is reasonable to expect that the output of the gages mounted partially in the root of the 5 module spur gears would be less than theory would indicate.

Throughout the experimental testing of the four pairs of gears, it was consistently observed that the measured strain levels of gear teeth entering or leaving the meshing region were significantly less than their predicted values. Oda et al. [44, 45] conducted tests to measure the influence of helix angle and case hardening on the fatigue strength of helical gears. As part of this study fillet stresses were determined through the meshing cycle for one spur gear pair and three helical gear pairs. The face contact ratios of the helical gears were 0.37, 0.73, and 1.06. Oda's results indicate that for all gears tested, the tensile fillet stresses increased rapidly as the gear entered the meshing region and decreased rapidly as it left the meshing region. While the exact shapes differ because of different gear geometries and loads, the general variation of fillet strains through the meshing cycle observed by Oda is consistent with the results of this thesis. Oda concluded that for all of the gear pairs investigated, the maximum tensile stress occurred when the meshing point in the central transverse plane coincided with the point of maximum stress intensity. This result is consistent with measured and predicted fillet strains of the 5 and 8 module spur gears and the 8 module helical gears.

In another investigation, Oda et al [46] examined the tensile fillet stresses in welded spur gears as a function of web structure. Results of this study indicate a large increase in tensile fillet stress from comparatively low levels as the gear enters the mesh. The magnitude of these stresses at the engagement of the tooth is approximately 60% of the values which would be predicted by Colbourne's method.

One of the assumptions on which the theory used to calculate theoretical strains in this thesis is based is that the magnitude of the load intensity is constant along all of the lines of contact. If the stress intensity was lower for contact lines just entering or about to leave the plane of contact, fillet stresses of the gear teeth associated with these

contact lines would be reduced.

Sundarajan and Young [47] conducted a three dimensional finite element study of large spur and helical gear systems. A result of their work from a typical aerospace application indicates that load intensity is not constant along the total contact length. The value of the average load intensity along gear teeth just entering and about to leave the meshing region was calculated to be 50% of the value of the average load intensity of a tooth in the center of the mesh.

Finally, Eisentraut [48] examined the tensile fillet stresses present on a wide variety of helical gears with the use of a three dimensional finite element model. He discovered that the maximum fillet stress of most gears will occur when the fraction of the load on the tooth first becomes a maximum as the load moves from a corner loading position. This condition will occur for helical gears with face contact ratios less than 1 when the load intensity is a maximum and for gears with face contact ratios greater than 1 when the contact point is at the tip radius and the load intensity is a minimum. These numerical results are consistent with the experimental results described here. Eisentraut's results also revealed that the assumption of uniform leading along the line of contact is not precise.

Chapter 6: Conclusions

A recirculating power gear testing apparatus was constructed to perform gear research in a number of areas. This apparatus was used to investigate the variation of static tensile fillet strains through the meshing cycle of four spur and helical gear pairs. Experimentally measured strains during this study were compared to the theoretically predicted values of Colbourne's method. Conclusions which can be drawn from this study are as follows:

1. The maximum tensile fillet strains predicted by Colbourne's method for the 5 module and 8 module spur gears were 14% and 11% greater, respectively, than the maximum measured tensile fillet strains. The former result is influenced to some degree by details of the experimental setup which would reduce the measured strain. The largest fillet strains were measured when the contact point was close to the highest point of single tooth contact and the load intensity would be near a maximum. This result is predicted by Colbourne's method and AGMA 2001-B88.
2. For the 8 module helical gear pairs with a face contact ratio of 0.5, Colbourne's method and AGMA 2001-B88 predict that the maximum tensile fillet strain will occur when the load intensity is a maximum and when the contact point is located at either the highest point of single tooth contact (AGMA 2001-B88) or between the highest point of single tooth contact and the tip radius (Colbourne). Experimental results indicate that near maximum tensile fillet strain values were obtained for a series of contact points. The first point of this series was located between the tooth tip and the highest point of single tooth contact while the final point was located slightly below the highest point of single tooth contact. For this gear pair Colbourne's method underestimated the maximum measured tensile fillet strain by approximately 4%.
3. The results obtained in this thesis and examination of the experimental results of other investigators indicate that Colbourne's method overestimates the value of the tensile fillet strains for contact points within approximately 10% of either end of the path of contact. This discrepancy is believed to be caused by the assumption in Colbourne's formulation that the value of the load intensity is

constant along the entire contact length. The work of other investigators has indirectly shown that the average load intensity along lines of contact just entering or about to leave the plane of contact is less than the average load intensity for the entire contact length. This difference appears to manifest itself most clearly in the 6 module helical gear test results. Test results for these gears indicate that the maximum tensile fillet strain was developed when the contact point was close to the tip radius and the load intensity would be near a minimum. Colbourne's method predicts this result, but AGMA 2001-B88 disagrees with it in terms of the value of the load intensity. The maximum predicted tensile fillet strain was 28% greater than the largest measured maximum tensile fillet strain.

4. Colbourne's method and other investigators have shown that the maximum predicted tensile fillet strain varies in each transverse plane of a helical gear pair. This predicted result could not be verified experimentally as a result of unsymmetric load distribution across the teeth instrumented to detect this variation.

5. All of the data collected indicates that Colbourne's method can be used as a design tool to predict safely the maximum tensile fillet strain in spur and helical gear teeth. The method appears to produce slightly conservative maximum fillet strain predictions for spur gears and very slightly nonconservative maximum fillet strain predictions for helical gears which exhibit wide variations of load intensity through the meshing cycle. For gear pairs whose maximum tensile fillet strain value occurs when the gear is loaded at the tooth tip (inaccurately cut spur gears and helical gears with little variation in total contact length) the method appears to produce more conservative results.

REFERENCES

[1] American Gear Manufacturers' Association, Rating the Pitting Resistance and Bending Strength of Spur and Helical Gear Teeth, AGMA 2001-B88, March, 1987.

[2] Colbourne, J.R., The Geometry of Involute Gears, New York: Springer-Verlag, Inc., 1987.

[3] Dolan, T.J. and Broghamer, E.L., "A Photoelastic Study of Stresses in Gear Tooth Fillets," University of Illinois Engineering Expt. Sta. Bull. 335, March, 1942.

[4] Wellauer, E.J. and Seireg, A., "Bending Strength of Gear Teeth by Cantilever-Plate Theory," Journal of Engineering for Industry, Trans. ASME, Vol. 82, Series B, No. 3, August, 1960, pp. 213-222.

[5] Colbourne, J.R., "Effect of Oblique Loading on the Fillet Stress in Helical Gears," Department of Mechanical Engineering, University of Alberta, Edmonton, Alberta, Canada, 1987.

[6] Towle, A., "The Scuffing of Automobile Gears," Chartered Mechanical Engineer, Vol. 21, No. 10, 1974, pp. 99-104.

[7] Townsend, D.P., Zaretsky, E.V. and Scibbe, H.W., "Lubricant and Additive Effects on Spur Gear Fatigue Life," Transactions of the ASME, Vol. 108, July, 1986, pp. 468-477.

[8] Townsend, D.P. and Akin, L.S., "Gear Lubrication and Cooling Experiment and Analysis," Paper b-3, International Symposium on Gearing and Power Transmission, Tokyo, 1981, pp. 253-260.

[9] Akin, L.S. and Townsend, D.P., "Cooling of Spur Gears with Oil Jet Directed into the Engaging Side of Mesh at Pitch Point," Paper b-4, International Symposium on Gearing and Power Transmission, Tokyo, 1981, pp. 261-274.

[10] Haizuka, S., Naruse, C., and Nemoto, R., "Studies on Frictional Losses and Temperature Rise of Spur Gears," Bulletin of JSME, Vol. 29, No. 258, December, 1986, pp. 4416-4423.

[11] Naruse, C., Haizuka, S., and Nemeto, R., "Studies on Limiting Load for Scoring of Spur Gears," Bulletin of JSME, Vol. 22, No. 164, February, 1979, pp. 234-241.

[12] Fujita, K., Yoshida, A. and Akamatsu, K., "A Study on Strength and Failure of Induction Hardened Chromium-Molybdenum Steel Spur Gears," Bulletin of JSME, Vol. 22, No. 164, February, 1979, pp. 242-248.

[13] Townsend, D.P., "Surface Fatigue and Failure Characteristics of Hot Forged Powder Metal AISJ 4620, AISI 4640, and Machined AISI Steel Spur Gears," Lubrication Engineering, Vol. 43, No. 9, September, 1987, pp. 706-716.

[14] Atherton, W.J., Pintz, A., and Lewicki, D.G., "Automated Acoustic Intensity Measurements and the Effect of Gear Tooth Profile on Noise," 1987 ASME Design Technical Conference - 11th Biennial Conference on Mechanical Vibration and Noise, 1987, pp. 109-113.

[15] Atherton, W.J., Pintz, A., and Lewicki, D.G., "Automated Acoustic Intensity Measurements and the Effect of Gear Tooth Profile on Noise," Gear Technology, Vol. 5, No. 2, 1988, pp. 22-30.

[16] Labath, O.A. and McCarthy, D.L., "Full Speed, Full Torque Testing of a High Performance Marine Gearbox," AGMA Fall Technical Meeting, San Francisco, CA, October 14-16, 1985.

[17] Vance, J.M., "Measurement of Torsional Vibration in Rotating Machinery," Journal of Mechanisms Transmissions and Automation in Design, Vol. 108, December, 1986, pp. 565-577.

[18] Anderson, N.E. and Loewenthal, S.H., "Design of Spur Gears for Improved Efficiency," Journal of Mechanical Design, Vol. 104, October, 1981, pp. 767-774.

[19] Dudley, D.W., ed., Gear Handbook, New York: McGraw-Hill Book Company, Inc., 1962.

[20] Anderson, N.E. and Loewenthal, S.H., "Effect of Geometry and Operating Conditions on Spur Gear System Power Loss," Journal of Mechanical Design, Vol. 103, January, 1981, pp. 151-159.

[21] Mizutani, H., Isikawa, Y., and Townsend, D.P., "Effects of Lubrication on the Performance of High Speed Spur Gears," 15th Design Automation Conference, Montreal, Quebec, September, 17-21, 1989.

[22] Harris, T.A., Rolling Bearing Analysis, New York: John Wiley and Sons, 1966.

[23] American Gear Manufacturers' Association, Nomenclature of Gear Tooth Failure Modes, AGMA 110.04, 1980.

[24] Shigley, J.E., Mechanical Engineering Design, New York: McGraw Hill Book Company, Inc., 1980.

[25] American Gear Manufacturers' Association, Design of Components - Enclosed Gear Drives - Bearings, Bolting, Keys and Shafting, AGMA 260.02, January, 1974.

[26] SKF General Catalog, SKF Canada Ltd., 1986.

[27] Barwell, F.T., Bearing Systems: Principle and Practice, Great Britain: Oxford University Press, 1979.

[28] Bajaj, K.K., "Oil Mist Lubrication of Shaker Screen Bearings," Lubrication Engineering, Vol. 44, 10, October, 1988, pp. 852-855.

[29] Gesdorf, E.J., "Bearing Lubrication - How Much?, How Often?," Lubrication Engineering, February, 1987, Vol. 43, No. 2, pp. 117-120.

[30] "Increased Bearing Life Through Correct Oil Selection," SKF Canada Ltd., July, 1986.

[31] Musilli, T.G., "Grease - A Short Story," Lubrication Engineering, Vol. 43, No. 5, May, 1987, pp. 352, 353.

[32] Michalec, G.W., Precision Gearing: Theory and Practice, New York: John Wiley and Sons Inc., 1966.

[33] Dudley, D.W., Handbook of Practical Gear Design, New York: McGraw-Hill Book Company, Inc., 1984.

[34] Errichello, R., "Lubrication of Gears, Part 4," Lubrication Engineering, Vol. 46, No. 4, April, 1990, pp. 231-237.

[35] Papay, A.G., "Industrial Gear Oils - State of the Art," Lubrication Engineering, Vol. 44, No. 3, March, 1988, p. 218-229.

[36] Russell, A., "Gears and Their Lubrication," ASLE Alberta Section Fifth Annual Lubrication Seminar, Edmonton, Alberta, November 15, 1985.

[37] Boner, J., Gear and Transmission Lubricants, New York: Reinhold Publishing Corporation, 1964.

[38] Kotuis, P.V., "Overview of the Chemistry of Extreme-Pressure Additives," Lubrication Engineering, Vol. 42, No. 6, June, 1986, pp. 363-366.

[39] American Gear Manufacturers' Association, Lubrication of Industrial Enclosed Gear Drives, AGMA 250.04, 1981.

[40] Smith, J.D., Gears and their Vibration, New York: Marcel Dekkor, Inc., 1983.

[41] Tavakoli, M.S. and Houser, D.R., "Optimum Profile Modifications for the Minimization of Static Transmission Errors of Spur Gears," New York: ASME Paper 84-DET-173, 1984.

[42] Colbourne, J.R., "Gear Tooth Interference," Journal of Mechanisms, Transmissions and Automation in Design, Vol. 105, September, 1983.

[43] Hirt, M.C.O., Stresses in Spur Gear Teeth and Their Strength as Influenced by Fillet Radius, Arlington, Virginia: American Gear Manufacturer's Association, 1985.

[44] Oda et al., "Study on Bending Fatigue Strength of Helical Gears (1st Report, Effect of Helix Angle on Bending Fatigue Strength)," Bulletin of the JSME, Vol. 23, No. 177, March, 1980, pp. 453-460.

[45] Oda et al., "Study on Bending Fatigue Strength of Helical Gears (2nd Report, Bending Fatigue Strength of Case Hardened Helical Gears)," Bulletin of the JSME, Vol. 23, No. 177, March, 1980, pp. 461-468.

[46] Oda et al., "Study on Welded Structure Gears (2nd Report, Web Structures and Root Stress Distribution)," Bulletin of the JSME, Vol.. 24, No. 192, June, 1981, pp. 1078-1085.

[47] Sundarajan, S. and Young, B.G., "Finite-Element Analysis of large Spur and Helical Gear Systems," J. Propulsion, Vol. 6, No. 4, July-August, 1990, pp. 451-454.

[48] Eisentraut, M. A Determination of the Load Position Causing Maximum Fillet Stress in Helical Gear Teeth Using Three-Dimensional Finite Elements, M.Sc. Thesis, University of Alberta, Edmonton, Alberta, Canada, 1988.